Atomistic simulations to model defect formation, diffusion,

and ordering in $Cu(In,Ga)Se_2$ and Cd(Se,Te) alloys

Aaron Gehrke

A dissertation

submitted in partial fulfillment of the

requirements for the degree of

Doctor of Philosophy

University of Washington

2024

Reading Committee:

Scott Dunham, Chair

Ting Cao

Di Xiao

Program Authorized to Offer Degree:

Materials Science and Engineering

©Copyright 2024

Aaron Gehrke

University of Washington

Abstract

Atomistic simulations to model defect formation, diffusion,

and ordering in $Cu(In,Ga)Se_2$ and Cd(Se,Te) alloys

Aaron Gehrke

Chair of the Supervisory Committee:

Scott Dunham

Electrical and Computer Engineering

To improve the performance of $Cu(In,Ga)Se_2$ and Cd(Se,Te) thin-film photovoltaic devices, a robust understanding of the alloy species is needed. The presence of alloying introduces unique challenges, as multiple species are randomly dispersed on the same lattice sites in the material. To optimize device performance, it is necessary to understand and control the precise arrangement of these alloy species. First, it is necessary to understand the energetic interactions between the alloy species and the other species (and defects) in the system, as these interactions determine the types of ordering expected. Second, it is necessary to understand the diffusivity of the alloy species, as it is needed to predict the actual kinetically-limited structures that form under different processing conditions. Third, it is necessary to understand how the alloy arrangement affects the behavior of other critical defects in the material, as this can impact

phenomena such as dopant activation. Multi-scale modeling, where results from *ab initi*o calculations (such as those from density functional theory) are fed into higher-level models (such as kinetic lattice Monte Carlo and continuum simulations), is well-suited for exploring the behavior of alloys considered here. In this work, we predict the diffusion under varying conditions of In and Ga in $Cu(In,Ga)Se_2$ and of the intrinsic defects in Cd(Se,Te). We develop a nearest-neighbor interaction model to predict In/Ga ordering in $Cu(In,Ga)Se_2$ alloys, finding a positive correlation between the Ga concentration and the presence of vacancies on the Cu-sublattice. We use this model to predict the band gap fluctuations resulting from these composition variations under a range of different processing conditions, producing results that agree well with experiment. We demonstrate a mechanism to passivate detrimental Cu_{In} defects in $Cu(In,Ga)Se_2$. We conduct a detailed analysis of the effects of Se/Te ordering in Cd(Se,Te) on the formation of detrimental AX center compensating defects, and investigate possible mitigation methods. Lastly, we present work done in conjunction with the UW MEM-C program on $(10\bar{1}0)$ surface reconstructions in ZnO.

Contents

1 Introduction, Background, and Motivation **4**

1.1 Cu(In,Ga)Se_2 and Cd(Se,Te) 4

1.2 Diffusivity Model 8

1.3 Multi-scale Modeling Techniques 9

2 Cu(In,Ga)Se_2: Ab Initio Calculations **17**

2.1 Introduction 17

2.2 Methods 18

2.3 Binding Energies 20

2.4 Migration Barriers 28

3 Cu(In,Ga)Se_2: Diffusivity Models **33**

3.1 Methods and Model Selection 33

3.2 In and Ga Diffusivity 37

3.3 Analytic Models 42

3.4 Comparison to Experiment 45

4 Cu(In,Ga)Se_2: Group-III Sublattice Ordering **47**

4.1 Introduction 47

4.2 III-Sublattice Interactions Model 49

4.3 Kinetic Lattice Monte Carlo 55

5 Cu(In,Ga)Se_2: Cu_{In} Passivation **64**

5.1 Introduction 64

5.2 Model Calibration 65

5.3 Capture Cross Section Estimation 68

5.4 Comparison to Experiment 74

6 Cd(Se,Te): Diffusion of Intrinsic Defects **76**

6.1 Introduction 76

6.2 Ab Initio Calculations 78

6.3 Kinetic Lattice Monte Carlo 80

7 Cd(Se,Te): As and P Doping **84**

7.1 Introduction 84

7.2 Methods 85

7.3 Results and Discussion 91

7.3.1 Maximum dopability and net doping effectiveness 91

7.3.2 Relation between dopant concentration and Fermi level 99

7.3.3 Effects of quenching on doping 103

7.3.4 Comparison with previous literature 106

8 ZnO: Surface Modeling **110**

8.1 Introduction 110

8.2 Bulk ZnO 111

8.3 [10$\bar{1}$0] ZnO Surfaces 113

9 Conclusions, Reflections, and Future Work **118**

Acknowledgments **123**

Chapter 1

Introduction, Background, and Motivation

1.1 $Cu(In,Ga)Se_2$ and Cd(Se,Te)

The need for improved renewable energy sources has increased interest in solar energy technologies. $Cu(In,Ga)Se_2$ (CIGS) and Cd(Se,Te) (CdSeTe) are the two best-established thin-film technologies, capturing the number 3 and 2 spots, respectively, in global market share after silicon-based cells (as of 2023)[1]. Both of these are chalcogenides, and for both the highest-performing material requires alloying, whether In and Ga in CIGS or Se and Te in CdSeTe. Because the two alloy species are randomly distributed on the same lattice sites in the material, this presents unique challenges and opportunities for study. Precise control of the diffusion of the alloy species during film growth is needed to optimize the alloy ordering, which can locally affect critical parameters such as the band gap and dopant activation.

Chalcopyrite CIGS is a promising candidate absorber material for thin-film photovoltaic devices, as CIGS solar cells have shown the highest light-to-electricity conversion ever reported of any thin-film photovoltaic technology[2]. Furthermore, CIGS-based devices have been shown to

be very stable, showing no signs of performance degradation over time[3],[4]. CIGS displays a high tolerance for crystalline disorder, which allows for significant control of the electronic properties of the material[5]. CIGS is a solid solution of $CuInSe_2$ (CIS) and $CuGaSe_2$ (CGS), with In and Ga occupying the same III-sublattice. Figure 1.1 shows the chalcopyrite structure of CIGS and the

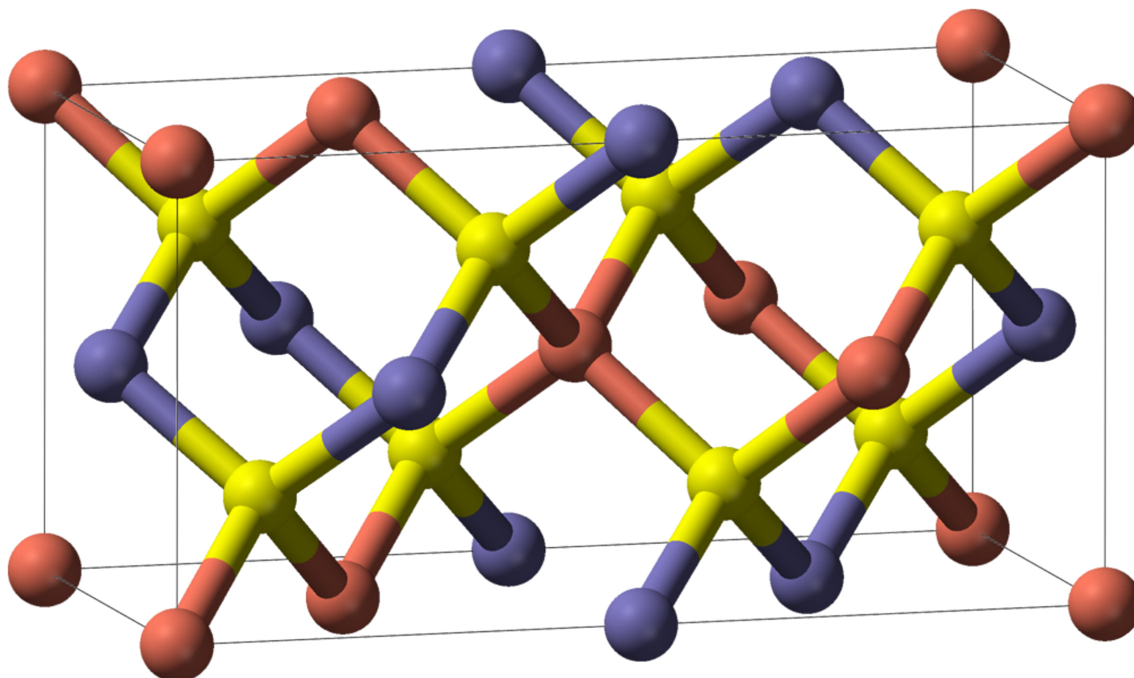

Figure 1.1: CIGS unit cell, containing 16 basis sites. Red = Cu, yellow = Se, blue = In/Ga.

three sublattices: Cu, In/Ga (group-III species), and Se. CIGS is a I-III-VI_2 tetrahedrally bonded semiconductor, with a band gap that varies from 1.0 eV in pure CIS to 1.7 eV in pure CGS.

The ability to tune the band gap of CIGS material by altering the Ga content provides an additional benefit, allowing the devices to not just be tuned to the solar spectrum, but to have the band gap vary as a function of depth, leading to improved performance[6]. The highest performance commercially available CIGS absorbers typically are designed with a Ga concentration gradient, from variations in the $[\mathrm{Ga}]/([\mathrm{Ga}]+[\mathrm{In}])$ (GGI) ratio within the layer. In graded cells, the recombi-

nation rate is lowered, improving the open-circuit voltage. Likewise the short-circuit current can be increased with proper grading. Both of these lead to higher conversion efficiencies. Understanding the diffusion mechanisms and ordering of In and Ga in CIGS is therefore critical to optimizing cell performance[2],[4],[7]. Furthermore, defects in CIGS with energy levels deep within the band gap can act as unfavorable recombination centers and also limit the performance of the device[8]. In many cases, these deep level traps can be passivated by forming complexes with other defects[8]. If the complex formation reactions are diffusion-limited, models for diffusion can also be used to simulate and understand this critical passivation process.

In addition to CIGS, we are also interested in studying CdTe and the related alloy CdSeTe. CdTe is a technologically important semiconducting material used for infrared and X-ray detectors[9],[10]. It can be doped both *n*-type and *p*-type (although only weakly *p*-type) without adding foreign impurities, which makes it particularly attractive for use in photodiodes and optical detectors[11],[12]. It also finds use as the absorber layer in CdTe thin-film solar cells, the application we are most interested in[13]. CdTe is well-suited for use in photovoltaic devices due to a number of favorable properties. Its band gap of 1.5 eV is a good match to the solar spectrum. It also possesses good carrier mobility and a high optical absorption coefficient that allows it to absorb most of the sunlight with only a very thin absorber layer[9],[11]. Lastly, CdTe solar cells can be manufactured quickly and inexpensively: it only takes a matter of hours to go from input materials to completed modules. Thus, it is not surprising that CdTe has claimed the second largest market share (5%) of any photovoltaic technology after crystalline silicon[14].

CdTe is a II-VI tetrahedrally bonded semiconductor that crystallizes in the zinc-blende structure, shown in Figure 1.2[15]. Unlike CIGS, CdTe is much less defect tolerant, with defect concentrations generally not exceeding 1 part per 10,000[16]. As a result, the defects will likely not

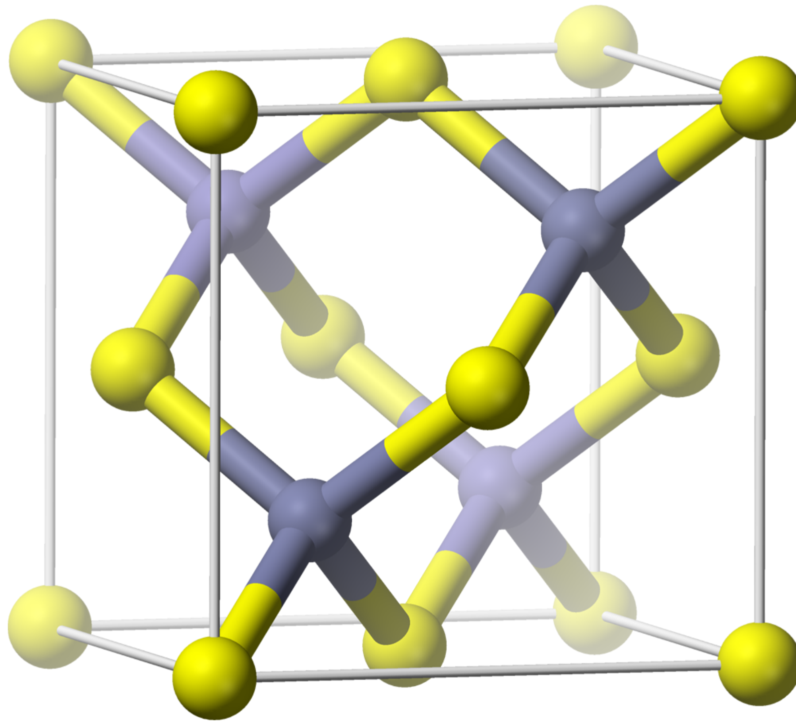

Figure 1.2: CdTe unit cell, containing 8 basis sites. Yellow = Cd, blue = Te.

interact significantly, and the dilute approximation can be applied. Recent advancements in CdTe-based thin-film photovoltaic technologies have been due in part to the use of graded CdSeTe absorbers, which increases the collected photocurrent[17]. CdSeTe is an alloy of CdTe and CdSe, formed by introducing both Te and Se on the same sublattice. Atomic diffusion in semiconductors is important in determining material properties such as the doping limit, passivation, and device stability[13]. Understanding and control of the diffusion profiles of intrinsic and extrinsic defects is critical for developing the highest-performing electronic and optoelectronic devices[18]. Therefore, we seek to understand the diffusion of different defects in CdTe. Additionally, doping can be a challenge in CdTe and CdSeTe due to self-compensation[19]. Therefore, we also want to model this self-compensation, with particular attention to how the ordering of the alloy species Se and Te affects the propensity of the system to self-compensate.

1.2 Diffusivity Model

The overall diffusivity of any given atomic species will be the sum of the diffusivities of the different defects and defect complexes in which the species occurs. In general, the diffusivity of a given defect or defect complex can be modeled in the typical Langmuir-Arrhenius form[5],[20]

$$D = gf\lambda^2 p_d \nu e^{-\Delta E_m/k_B T} \tag{1.1}$$

where $g = z/2d$ is a geometric factor determined by the nearest-neighbor coordination number z and the dimensionality of the lattice d, f is a correlation factor dependent on the mechanism, λ is the hopping distance, p_d is the probability that the defects necessary for diffusion are available, ν is the attempt frequency, ΔE_m is the migration barrier, k_B is the Boltzmann constant, and T is the temperature.

Diffusion occurs when a defect hops from one lattice site to a neighboring one. Eq. 1.1 contains terms that reflect both the average rate that a hop occurs and the total displacement that a hop contributes to diffusion. The hopping rate of the diffusing species is given by the terms $\nu e^{-E_m/k_B T}$. The attempt frequency ν arises from the natural vibration modes in the crystal, and reflects the projection of the vibrations of the defect along the direction of the reaction coordinate, effectively representing the frequency the defect "attempts" the hop. The migration barrier ΔE_m is the minimum energy the defect must overcome to pass over the saddle point between stable ground states. The exponential term is a Boltzmann distribution, which gives the fraction of attempts with energy high enough to overcome this barrier at temperature T. The product of the attempt frequency and fraction of attempts that are successful is then the rate that hops of the defect will occur. The term p_d is the fraction of the total diffusing species that occurs as the defect being considered at equi-

librium. Thus this term reflects that very dilute defects will contribute less to overall diffusivity than more abundant defects. The hop distance squared λ^2 incorporates the distance traveled by a hop and transforms the units from frequency of hops (s^{-1}) to units of diffusivity (cm^2s^{-1}). Each hop that occurs is not completely random, but will be correlated to the previous hop. The correlation factor f relates how likely a hop is to reverse the previous hop, with $f = 1$ being completely uncorrelated, and $f = 0$ being completely correlated (every hop reverses and no diffusion occurs). The correlation factor is given by

$$f = \frac{1 + \langle \cos(\theta) \rangle}{1 - \langle \cos(\theta) \rangle} \tag{1.2}$$

where $\langle \cos(\theta) \rangle$ is the average projection of hop direction on that of the previous hop. For the Cu-sublattice $z = 4$, because of tetrahedral coordination. One primary aim of this work is to calculate these various terms needed to model diffusion in CIGS and CdSeTe and apply different modeling techniques to understand and predict diffusion of native and non-native species in these materials.

1.3 Multi-scale Modeling Techniques

The different contributions to Eq. 1.1 can be determined with a variety of modeling tools, such as density functional theory (DFT), the chemical constraint calculator (CCC), and kinetic lattice Monte Carlo simulations (KLMC). Figure 1.3 illustrates schematically the approach followed to model diffusivity starting from first principles. The defect formation energies, defect complex binding energies, migration barriers, and attempt frequencies can be calculated *ab initio* from DFT packages. The formation and binding energies are used in the CCC to predict the equilibrium concentration of different defects and the Fermi level of the material under variations in temperature and composition of the system. Results are then fed into KLMC models, which require knowledge

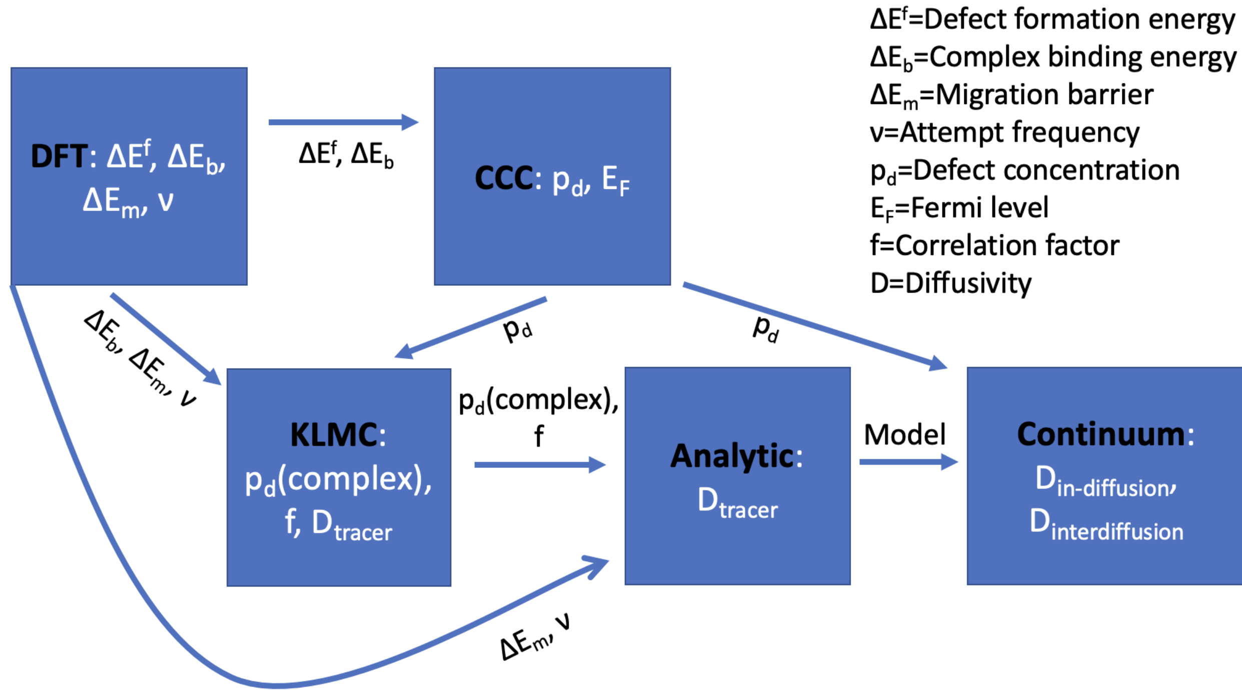

Figure 1.3: Schematic of approach to multi-scale modeling of diffusivity.

of both the defect hopping rates (from DFT) and defect concentrations (from the CCC). The KLMC models provide information on the diffusivity and the equilibrium ordering of the different species (such as the concentration of different complexes), as well as the observed correlation factors. Analytic models are developed with Eq. 1.1 that can reproduce KLMC results. Lastly, a successful analytic model is used in continuum simulations (which are populated with defect concentrations from the CCC) to model different experimental setups and geometries, such as in-diffusion from a substrate, or interdiffusion between diffusion couples. This schematic can also be modified to model phenomena besides diffusion. By removing kinetics we can utilize simply lattice Monte Carlo (LMC), which takes defect concentrations and defect binding interactions as input, but does not consider hopping rates. LMC can model defect ordering and phase segregration, as well as defects whose formation energy depends on the local atomic arrangement. Both of these situations are common in alloys such as CIGS and CdSeTe, where the arrangement of the alloy species has

important effects on the material properties. Both KLMC and LMC are therefore well-suited for understanding these materials.

DFT is a method of calculating an approximate solution to the many-body Schrödinger equation. It can provide information on the electronic and ionic structure of a wide variety of systems. In essence, DFT replaces a many-body wave function with 3N coordinates with a one-body density $n(r)$ with only three spatial coordinates, making computation possible even for large systems[21],[22]. The Hohenburg-Kohn theorem states that this electron density is sufficient to predict all the ground-state properties of the system[21]–[23]. The Kohn-Sham potential was developed to represent a fictitious system of non-interacting particles that gives the same density as that of the interacting system. The total energy can then be written as:

$$E[\rho] = T_s[\rho] + V_{ext}[\rho] + V_H[\rho] + E_{xc}[\rho] \tag{1.3}$$

where T_s is the kinetic energy, $V_{ext}[\rho]$ is the external potential from the electron-nuclei interaction, $V_H[\rho]$ is the Hartree potential from the electron-electron interactions, and $E_{xc}[\rho]$ is the exchange-correlation potential that corrects the errors in the other terms resulting from neglecting the non-classical many-body interactions[21],[22],[24]. Several schemes have been developed to account for the exchange-correlation energy, such as the Local Density Approximation (LDA), the Generalized Gradient Approximation (GGA), and hybrid functionals such as the Heyd-Scuseria-Ernzerhof (HSE) functionals, which include contributions from Hartree-Fock calculations[21]. Additionally, pseudopotentials such as the Projector Augmented Wave (PAW) pseudopotential are employed to replace the complicated effects of the nuclear and core electron motion with a softer potential that captures the core's effects on the outer valence electrons[21].

When implementing DFT, the electronic wavefunctions must be approximated with a basis set of functions. For periodic crystalline solids, it is best to use Bloch's theorem to expand the wavefunctions in terms of a discrete plane-wave basis set, which is truncated at some particular energy cutoff[21],[25]. The material being studied can then be represented as an infinite periodic array of finite-sized supercells. To model a defect, an atom can be added, removed, or replaced from the perfect supercell. The structure is then relaxed to find the ground state energy and ionic positions. The strain arising from the defect can be observed by comparing the relaxed ionic positions and lattice constants with those of a defect-free cell.

The climbing image nudged elastic band (CI-NEB) method can determine the minimum energy pathway (MEP) of an atom moving between two ground states. A pathway connecting the two states is guessed initially, with the path divided between a fixed number of images representing the intermediate states of the process. Ordinary NEB relaxes the images to the MEP while maintaining the spacing between them. This is accomplished by adding spring forces between images

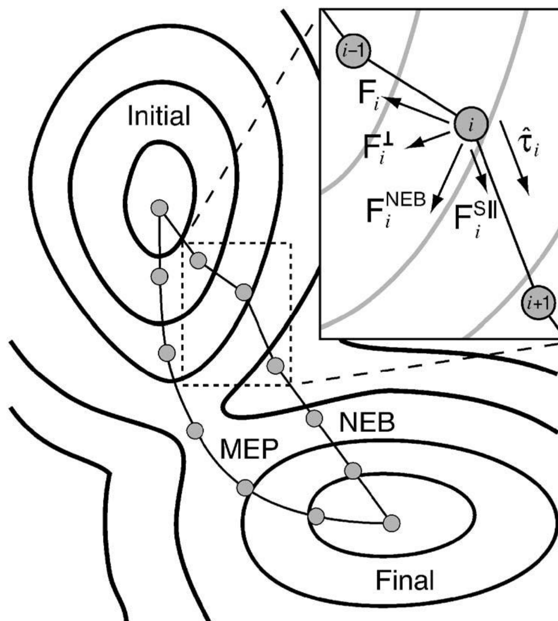

Figure 1.4: Illustration of the NEB approach showing the forces on the images that move them towards the MEP in a potential energy landscape [26].

and projecting the force component due to the potential perpendicularly to the spring forces, as illustrated in Figure 1.4[27],[28]. The climbing image modification drives the highest energy image up to the exact saddle point[29].

In addition to the CI-NEB method, the dimer method can be used to search for saddle points in random directions when the exact pathway is not known[30]. This method involves two identical images (or replicas) of the system separated at a fixed distance, known as the “dimer”. The algorithm searches for saddle points by pushing the dimer uphill on the potential energy surface. As it is translated, the dimer is also rotated to be oriented along the lowest curvature mode. The run converges on a saddle point when the forces on any degree of freedom in the system fall below a set value and the curvature is negative (indicating a saddle geometry).

To determine the attempt frequency of a process, the phonon frequencies of both the relaxed ground and the relaxed saddle structures can be calculated using density functional perturbation theory (DFPT)[31]. This method determines the Hessian matrix, or the matrix of the second derivatives of the energy with respect to atomic displacements, by perturbing each ion a small, fixed amount in each of the directions ±xyz. From the matrix the eigenvalues and corresponding eigenvectors are also calculated, where the eigenvalues are the normal vibrational modes of the system. From transition state theory, the attempt frequency of the process v^* can be calculated by

$$v^* = \prod_{i=1}^{3N-3} v_i \Bigg/ \prod_{i=1}^{3N-4} v_j^{'} \tag{1.4}$$

where v_i and $v_j^{'}$ are the normal vibrational modes of the ground and saddle states respectively[20]. The 3 translational modes are excluded, as well as the unstable imaginary mode that occurs in a properly converged saddle state.

Molecular dynamics (MD) can also be used to further investigate for different ground states, possible transitions, and vibrational properties. In DFT, MD is implemented by advancing the system by a fixed time step. At each step the forces on the ions are recalculated from DFT, and the positions advanced by numerically solving Newton's equations of motion, such as with Verlet integration. By observing a system for a large number of timesteps, unusual defect ground states or unexpected transitions may be seen that would not otherwise have been considered.

Compositionally constrained thermodynamics (as implemented in the CCC developed by this group[32]) can be used to predict equilibrium concentrations of defects d in charge states q at varying temperature and composition by[33]:

$$\frac{c_{d,q}}{1-c_{d,q}} = \theta_{d,q} e^{-\Delta E^f_{d,q}/k_B T} \tag{1.5}$$

where $c_{d,q}$ is the fractional concentration of the defect; $\theta_{d,q}$ is the entropic prefactor arising from lattice mixing, configurational degeneracy, and electronic state degeneracy; $\Delta E^f_{d,q}$ is the defect formation energy. The formation energy reflects the energy change in forming a defect, and can be calculated with DFT assuming a grand canonical picture of defect formation by the equation[33]

$$\Delta E^f_{d,q} = E_{d,q} - E_{bulk} + \sum_i n_i(\mu_i^0 + \Delta\mu_i) + q(E_{VBM} + E_{Fermi} + \Delta V) + E_{corr} \tag{1.6}$$

where $E_{d,q}$ is the energy of the supercell containing the defect and E_{bulk} is the ground state energy of the perfect crystal supercell. n_i is the number of atoms of type i added or removed from the material in forming the defect, and $\mu_i^0 + \Delta\mu_i$ is the chemical potential of species i with respect to a consistent reference. The chemical potential reflects the favorability of adding a species from a reservoir to the system: increasing the chemical potential of species i will increase its prevalence

in the system (likely favoring formation of interstitials and antisites of i), while decreasing the potential of i will decrease its prevalence (likely favoring vacancies of i). Thus the composition can be selected for by controlling the chemical potential. The chemical potential of electrons is given analogously by the Fermi level E_{Fermi} with respect to the bulk valence band E_{VBM}. The finite size of the cell introduces spurious interactions, which are accounted for by the correction term E_{corr}. Additionally, to avoid divergence of the infinite array of charged cells, the DFT calculations introduce a neutralizing background, which produces an offset accounted for by the potential alignment correction ΔV.

Monte Carlo methods use repeated random sampling to model deterministic systems. The basic premise of KLMC as implemented in this work starts with an initialized system of lattice points, and different species assigned to each point. Site-specific elementary processes for all allowed events on the lattice are defined, along with rates for each process. These rates additionally can be updated on the fly based on the local environment surrounding the process site(s). The algorithm then proceeds by matching all processes with the geometry at each lattice site and obtains the total rate of each process based on all the sites on which the process can occur. A process to perform is chosen randomly, proportionate to the relative total rate of the process. A site where the process is available is then chosen randomly to perform the process on, and the geometry is updated to reflect the process occurring. The system time is then propagated by drawing a random number ρ between 0 and 1 and adding the time step Δt given by

$$\Delta t = \frac{-\ln(\rho)}{P_k} \tag{1.7}$$

where P_k is the total rate of the process k in the system. This is repeated for a set number of steps[34].

KLMC is preferrable to methods such as MD when studying diffusion, because transition events occur very infrequently compared to the vibration periods of the system. KLMC allows the long time spans between events to be accelerated by ignoring the vibrational motion of the system and instead performing the events of interest with associated rates of occurrence.

Chapter 2

$Cu(In,Ga)Se_2$: Ab Initio Calculations[1]

2.1 Introduction

We first are interested in developing a model for the diffusion of group-III species in CIGS. To start, we must identify the diffusion mechanisms to include in our model. There are numerous mechanisms that could potentially mediate the diffusion of these species. In a crystal, diffusion proceeds through three primary mechanisms: (1) interchange by rotation, (2) migration through interstitial sites, or (3) diffusion via vacant lattice sites[6]. Ref. [3] measured the diffusivity of Ga into single crystal CIS layers, at varying compositions. It was found that the diffusivity was lowest at Cu/In ratios closest to unity, when the concentration of cation sublattice (groups I: Cu, and III: In/Ga) vacancies was expected to be at a minimum. This suggests that Ga (and potentially In) diffuse via metal vacancies[3],[4]. Ref. [36] found that annealing CIGS films in an argon atmosphere led to In/Ga interdiffusion, but annealing in a selenium atmosphere produced no such interdiffusion. They postulated that when annealing with argon, Se vacancies are formed. This

[1]Reproduced from A. S. Gehrke, D. E. Sommer, and S. T. Dunham, "Atomistic models of In and Ga diffusion in $Cu(In,Ga)Se_2$," *Journal of Applied Physics*, vol. 134, no. 11, p. 115 002, 2023, with the permission of AIP Publishing.

in turn promotes the formation of metal vacancies, which are more likely to compensate for Se vacancies than Se interstitials due to more favorable formation energies. The increase in metal vacancies then facilitates In/Ga diffusion. Ref. [6] also found results that suggest a vacancy diffusion mechanism.

Computational studies by Ref. [37] predict that interstitial In_{int} will not form entirely, but instead will spontaneously switch with a nearby Cu atom to form an In_{Cu}-Cu_{int} complex, suggesting that interstitial migration of In is not an important mechanism. Additionally, they found the formation energy of V_{In} to be very high, and thus the thermal concentration of In vacancies is expected to be very low. More recent computational work by Ref. [38] also confirms that the formation energies of In_{int} and V_{In} are much higher than that of V_{Cu} over a wide range of Fermi levels and chemical potentials, confirming that these defects are not expected to occur in meaningful abundance. These findings reduce the importance of the III-sublattice in contributing to mass transport in CIGS[7],[37]. Ref. [37] predicts that all extra In atoms will eventually form In_{Cu} defects, and that formation energy considerations suggest an abundance of V_{Cu} and In_{Cu} defects. Additional theoretical studies have confirmed a similar abundance of Ga_{Cu} defects in CIS, along with an abundance of In/Ga_{Cu} in CGS[39],[40]. Building on these findings, we propose a model of group-III diffusion whereby In_{Cu} and Ga_{Cu} antisites diffuse via V_{Cu} defects.

2.2 Methods

We calculated binding energies and migration barriers using VASP based on the projector augmented-wave method (PAW) and using a plane-wave basis set[41]. The energy cutoff of the plane-wave set was 385 eV, and the generalized gradient approximation (GGA) type Perdew-Burke-Ernzerhof

Table 2.1: Calculated and measured (Refs. [44] and [45]) lattice constants a, b and c for the tetragonal 16-atom unit cell.

		a, b Å	c Å
Present work:	$CuInSe_2$	5.88	11.85
	$CuGaSe_2$	5.68	11.28
Experiment:	$CuInSe_2$[44]	5.78	11.62
	$CuInSe_2$[45]	5.81	11.63
	$CuGaSe_2$[45]	5.61	11.03

(PBE)[42] exchange-correlation functional was employed. For binding energy calculations, we also employed hybrid Heyd-Scuseria-Ernzerhof (HSE06)[43] exchange-correlation functionals, with the portion of the Hartree-Fock exchange set to $\alpha = 0.25$, and an inverse screening length of $\omega = 0.2\,\text{Å}^{-1}$ (the default values for HSE06, having been shown to be suitable for most systems[43]). Most calculations were performed with a 64-atom cell and 4 x 4 x 4 Monkhorst-Pack *k*-point mesh, while some calculations required a 128-atom cell with 4 x 4 x 2 (if *c*-direction was doubled) or 2 x 4 x 4 (if *a*-direction was doubled) *k*-point mesh. The extrapolations using 16-, 128-, and 432-atom cells also used 4 x 4 x 2 *k*-point sampling. Ionic positions were relaxed until intra-ionic Hellmann-Feynman forces fell below 0.01 eV/Å, while the cell volume and shape were fixed to their ideal CIS or CGS values. The calculated lattice constants for CIS and CGS are shown in Table 2.1, and compared with experimental values. Our structural parameters show reasonably good agreement with experiment, with the *c* axis generally larger in our calculations. For calculation of migration energy barriers in VASP, the climbing-image nudged elastic band (CINEB) method was used[29].

2.3 Binding Energies

The binding energy of a defect complex composed of n defects is given by

$$E_b = E^f[\text{complex}] - \sum_{i=1}^{n} E^f[i] \tag{2.1}$$

where the sum of the formation energies of the isolated constituents is subtracted from the formation energy of the complex. It relates the energy that is gained or lost by bringing two or more defects together from infinite separation. By our convention, a negative binding energy denotes an attractive interaction, and a positive binding energy denotes a repulsive one. Binding energies should be reported with respect to the stable charge states of the individual defects, which for our purposes are ${V_{Cu}}^{-1}$ and ${[In,Ga]_{Cu}}^{+2}$, in both CIS and CGS[40]. Binding energies have been previously reported for antisite-vacancy complexes on the Cu-sublattice, but they show a wide scatter of values[37],[40],[46]. Here we attempt to harmonize these values with our own calculations, by identifying discrepancies in the calculation and reporting of the results among the different works.

We took a different approach than in these previous works, by demonstrating that the binding of In/Ga_{Cu} and V_{Cu} defects in CIGS can be modeled as coulombic interactions of point charges. As a result, the energy of an arbitrary configuration of these defects can be predicted from the electrostatic potential energy of an equivalently charged and spatially distributed array of point charges in a medium with static dielectric constant equal to that of CIGS. Such a model is computationally much more efficient than is DFT for computing the energy of a given atomic configuration. The energy can be calculated almost instantaneously on a computing system that would ordinarily take several hours for a similar calculation using DFT. The efficiency of such a model is particularly useful for large KLMC simulations, as employed later in this work.

In order to demonstrate that the interactions can be modeled as coulombic, we calculated the energies of 128-atom cells using DFT with defect pairs at varying degrees of separation. If coulombic interactions can account for the binding (or repulsion) between defects, the change in DFT energy upon separating a pair of defects should correspond to the change in the Madelung energy of an empty cell containing only the isolated charged defects undergoing the same separation. To calculate the Madelung energy, we modeled In/Ga_{Cu} as +2 and V_{Cu} as -1 point charges in an empty cell, with the static dielectric constant of bulk CIS/CGS. The Ewald summation solver provided by PYMATGEN was used for the calculations[47]. Note that for charged systems, both VASP and PYMATGEN impose a neutralizing background charge. The choice of the static dielectric constant proved to be a challenging issue. In particular, PBE-GGA functionals are known to overestimate the static dielectric constant relative to experimental values[37],[48]. Thus we cannot use experimental values directly, as they would not reflect the internal behavior of the DFT system to which we are comparing. Instead, the dielectric constant must be calculated from DFT, so that it can adequately capture the screening of coulombic interactions that occurs within the DFT framework being studied. However, attempts to calculate the static dielectric constant for CIS/CGS with PBE-GGA functionals failed to produce stable converged results, and so we simply used best-fit values of 17 for CIS and 15 for CGS. These can be compared with reported experimental values for CIS, which range from 11.3-13.6[49],[50], and for CGS, which range from 11-11.5[51]–[54]. In contrast, Ref. [38] calculated a value for the dielectric constant of $\approx$10.65 in CIS using HSE06 hybrid functionals, which is much closer to the experimental range. Therefore, we also performed DFT calculations using HSE06 functionals, and scaled the corresponding Madelung energies by the dielectric constant 10.65. Due to computational constraints, we did not relax the ionic degrees of freedom in the HSE06 runs, but only relaxed the electronic degrees of freedom starting with fully

relaxed PBE-GGA runs.

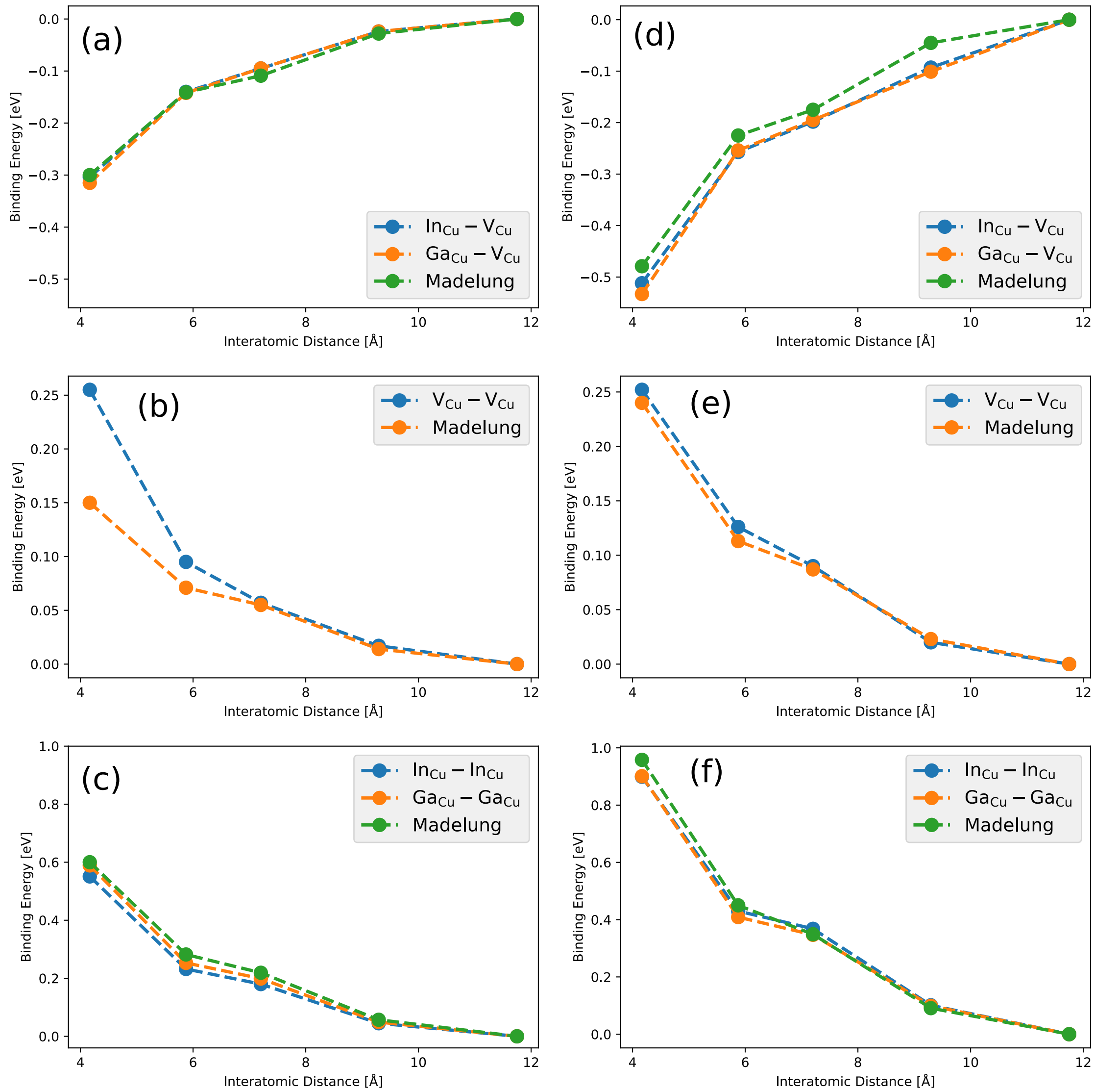

Figure 2.1: Energy change upon separation of different defect pairs in CIS, referenced to the energy at maximal separation within the cell. (a), (b), and (c) represent PBE-GGA calculations, while (d), (e), and (f) represent HSE06 calculations.

The results, shown in Figure 2.1, show a close match between DFT and Madelung energies, demonstrating that the binding of In/Ga_{Cu} and V_{Cu} defects can be modeled by coulombic interactions alone. Even though for the PBE-GGA calculations we adjusted the dielectric constant to fit the Madelung energies to the DFT energies, this does not necessarily invalidate the results, as they

still demonstrate that the energy variation with separation distance is well-modeled by considering only coulombic interactions. The only major deviation is in (b) for PBE-GGA calculations at 1st-nearest-neighbor (1NN) separation, but as this deviation does not appear in the equivalent and more accurate HSE06 calculation, it may be a unique feature of PBE-GGA functionals and not indicative of the real physical behavior. Note that in this work we use "1NN" and related terms such as "2NN" to refer to nearest-neighbors on the Cu-sublattice specifically, where "1NN" Cu sites are actually 2NN sites separated by Se atoms. We find that In and Ga have nearly identical behavior, despite differences in ionic radii. The CGS binding energies were also calculated, but are not shown as they are very similar to the results in Figure 2.1. The CGS binding energies tend to be slightly stronger than their CIS counterparts, explained by CGS having a slightly lower dielectric constant and slightly smaller lattice constants, both of which contribute to increased coulombic interaction. The differences between the PBE-GGA and HSE06 calculations in Figure 2.1 are due to the difference in dielectric constant. An important consequence of our findings is that, due to the slow decay of the r^{-1} coulombic energy dependence, we should expect long-range defect interactions, leading to loosely bound defect clusters, rather than tightly bound and well-defined defect complexes. This will impact not only the equilibrium configuration of defects, but also the In/Ga diffusion mechanisms, as discussed later in Chapter 3.

Having shown that the interactions of In/Ga_{Cu} and V_{Cu} defects can be modeled as coulombic, we can then predict the binding energy of any collection of n such defects simply as the total electrostatic energy of an array of point charges in a dielectric medium. This is given by[55]:

$$E_b = \frac{1}{2}\sum_{i=1}^{n}\sum_{j=1}^{n(i\neq j)}\frac{q_i q_j}{4\pi\varepsilon_0 \kappa r_{ij}} \tag{2.2}$$

where q_i, q_j are the nominal charges of defects i and j, r_{ij} is their separation distance, ε_0 is the vacuum permittivity, and κ is the dielectric constant. As PBE-GGA appears to overestimate the dielectric constant and HSE06 slightly underestimates it, we use experimental values for κ here in order to ensure that our reported values accurately reflect the behavior of the physical system, choosing κ=13.6 for CIS and κ=11.5 for CGS. This is justified because the DFT results in Figure 2.1 establish that the binding interactions can be accounted for by the coulombic interaction of point charges. Therefore, the actual strength of defect binding in CIGS material can be modeled by Eq. 2.2 with an experimental value for κ.

As an additional confirmation of this model for binding energy, we employed the extrapolation method proposed by Ref. [56] to calculate the binding energies of In_{Cu}-V_{Cu} and In_{Cu}-$2V_{Cu}$ complexes in CIS. This method requires calculating the binding energies in DFT using increasingly large supercells. The binding energies can then be extrapolated to the dilute limit to remove errors arising from finite cell size effects. This is accomplished by fitting the DFT results to the form:

$$E_b(L) = E_b(L \rightarrow \infty) + a_1 L^{-1} + a_3 L^{-3} \tag{2.3}$$

where L is the supercell dimension equal to the cube root of the cell volume, $E_b(L)$ is the binding energy found from cells of size L, and a_1, a_3, and $E_b(L \rightarrow \infty)$ are the extracted parameters. $E_b(L \rightarrow \infty)$ is then the binding energy extrapolated to the dilute limit. A requirement of this method is that all supercells used have the same symmetry. Starting with the 16-atom unit cell, we constructed three supercells: a 1x1x1 16-atom cell, a 2x2x2 128-atom cell, and a 3x3x3 432-atom cell. For a defect complex comprised of n point defects, the binding energy for a given supercell size is simply the combined energy of $n-1$ perfect supercells and one supercell containing the complex,

minus the combined energy of n supercells each containing one individual defect.

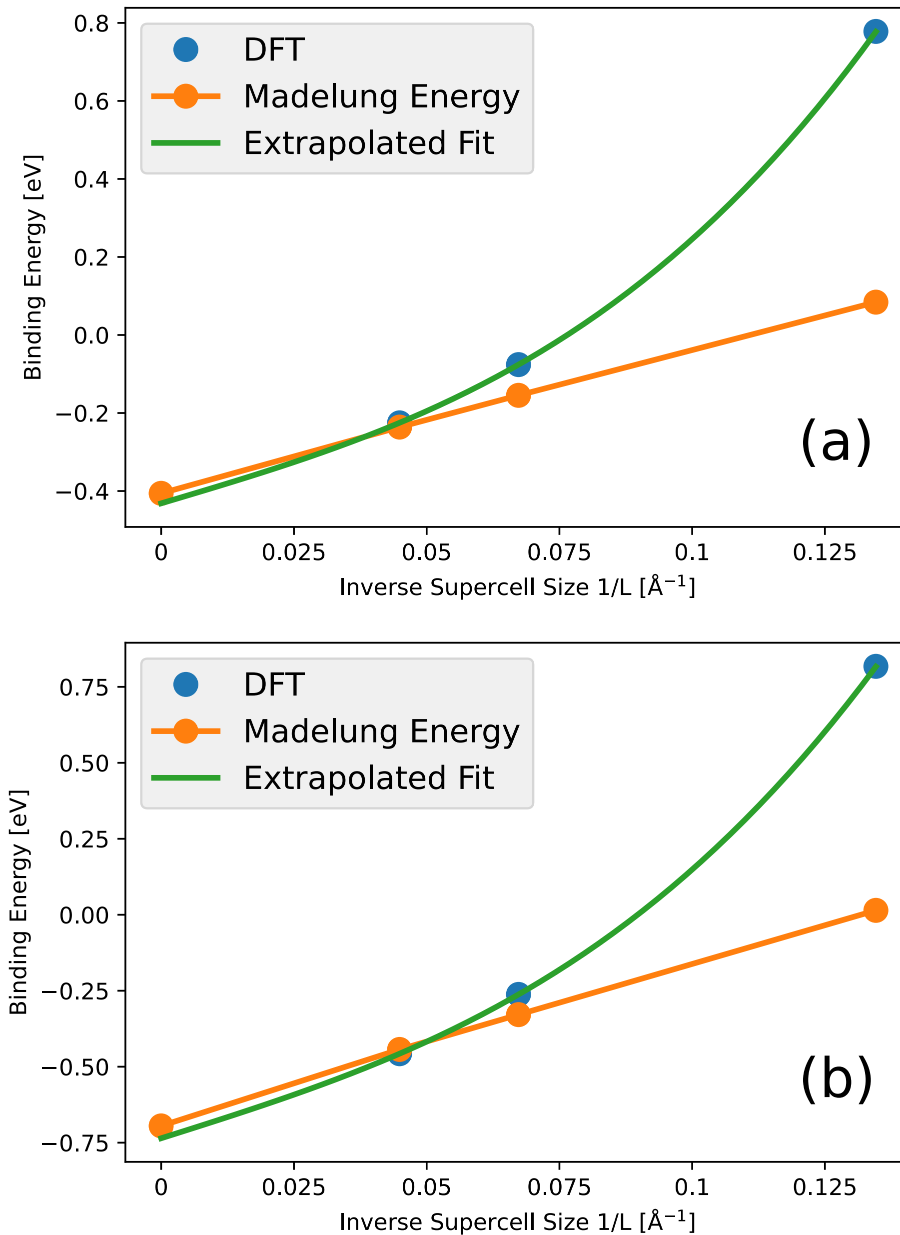

Figure 2.2: Binding energies of defect complexes in CIS extrapolated with respect to increasing supercell size. Supercell energies are calculated from DFT and also from the Madelung energy of only the charged defects in a periodic array. Binding energies for In_{Cu}-V_{Cu} (a) and In_{Cu}-$2V_{Cu}$ (b) are shown.

The results for PBE-GGA calculations are shown in Figure 2.2, along with the binding energies found by using only the Madelung energies of equivalent supercells containing only the charged

Table 2.2: Coulombic binding energies of antisite-vacancy complexes in their dominant charge state in eV calculated from Eq. 2.2 as compared to literature values.

	this work	Ref. [40]	Ref. [37]	Ref. [46]
$CuInSe_2$				
$([In/Ga]_{Cu}\text{-}V_{Cu})^{+1}$	-0.51	-0.18	-0.28	-
$([In/Ga]_{Cu}\text{-}2V_{Cu})^{+0}$	-0.85	-0.29	-0.46	-0.63/-0.67
$CuGaSe_2$				
$([In/Ga]_{Cu}\text{-}V_{Cu})^{+1}$	-0.63	-0.65	-	-
$([In/Ga]_{Cu}\text{-}2V_{Cu})^{+0}$	-1.05	-0.99	-	-

defects. For this, we took the Madelung energy of a supercell containing the complex composed of n defects and subtracted the Madelung energies of n supercells each containing one individual defect, ignoring perfect supercells as they contain no charged defects. Note that a value of κ=17 was used to scale the Madelung energies, which we found was appropriate for PBE-GGA, as previously explained. The results give converged values of -0.43 eV for In_{Cu}-V_{Cu} and -0.74 eV for In_{Cu}-$2V_{Cu}$. From the results it is clear that as supercell size increases, the values found with DFT converge to the values found with just the Madelung energy (which at infinite cell size is simply given by Eq. 2.2). The large deviations between the results found with DFT versus those found with the Madelung energy at small cell size can be explained by considering the different scaling of the two approaches. The Madelung energy scales like L^{-1} as observed. However, Eq. 2.3 includes a term that scales like L^{-3}, which accounts for the interaction of the localized charge distribution with the uniform background[57] and explains the large increase at small cell sizes. At infinite cell size, the two approaches converge to the same values and thus provide additional evidence for a model of binding of Cu-sublattice defects in CIGS that is coulombic.

Table 2.2 shows values for In/Ga_{Cu}-V_{Cu} and In/Ga_{Cu}-$2V_{Cu}$ complexes using Eq. 2.2 (note that the use of the lower experimental value for κ gives stronger binding energies in Table 2.2 than reported in Figure 2.2). Our values for CIS are much stronger than those found in Ref. [40], but

our values for CGS are very similar to theirs. Some difference may arise from their sampling of only a single cell size. Although they applied the correction scheme of Lany and Zunger[58], the corrected energy may still vary significantly with cell size[57]. Still, it is not clear why their values match ours for CGS but not for CIS, or why they find such a large variation between CIS and CGS, where we find little.

In Ref. [37], they also report weaker antisite/vacancy binding in CIS than we find. However, the value for the In_{Cu}-$2V_{Cu}$ binding energy in CIS is reported as the additional change in energy due to bringing a second V_{Cu} defect near a bound In_{Cu}-V_{Cu} complex. For consistency with our results, the value should be reported as -0.46 eV: the sum of the initial binding energy of the In_{Cu}-V_{Cu} pair and the energy change from adding a second V_{Cu} defect. This brings their value more in line with ours. Ref. [37] used the finite-size-scaling extrapolation scheme of Ref. [56] to obtain converged binding energies. However, as Ref. [56] explains, the extrapolation can only be done with cells of the same symmetry (such as cubic cells of increasing size). In contrast to our application of this method, Ref. [37] used cells of widely varying symmetry (in terms of 16-atom unit cells: 2x1x1, 2x2x1, 3x3x1, 3x3x2, and 4x4x2), and consequently their extrapolated values are not necessarily reliable. Despite this, their results for separating In_{Cu}-V_{Cu} pairs using PBE-GGA functionals produce energy differences of $\approx$0.3 eV, in line with values we find for a very similar procedure (see Figure 2.1).

Ref. [46] reports binding energies of the In/Ga_{Cu}-$2V_{Cu}$ complexes in CIS much closer to ours, although still weaker. Because the focus of their work is comparing the binding energies of In versus Ga complexes, rather than identifying the absolute magnitude of the energies, they did not attempt to extrapolate their results even though they are still changing markedly with increasing cell size (despite using the correction scheme of Freysoldt, Neugebauer, and Van de Walle[59]).

This suggests that after extrapolating to infinite cell size, they may find stronger binding energies than currently reported, bringing them even more in line with our values. Additionally, they concur with our results that In and Ga have similar binding energies.

2.4 Migration Barriers

As discussed in Chapter 2.1, previous experimental and computational work leads us to focus on a diffusion mechanism for In and Ga in CIGS dominated by 1NN vacancy-mediated hops of In_{Cu} and Ga_{Cu} antisites on the Cu-sublattice. This mechanism involves an In_{Cu} or Ga_{Cu} hopping onto a neighboring vacant V_{Cu} site. To calculate the migration barriers of these processes in CIS and CGS, DFT CINEB calculations were performed for vacancy-antisite exchanges. Figure 2.3 shows

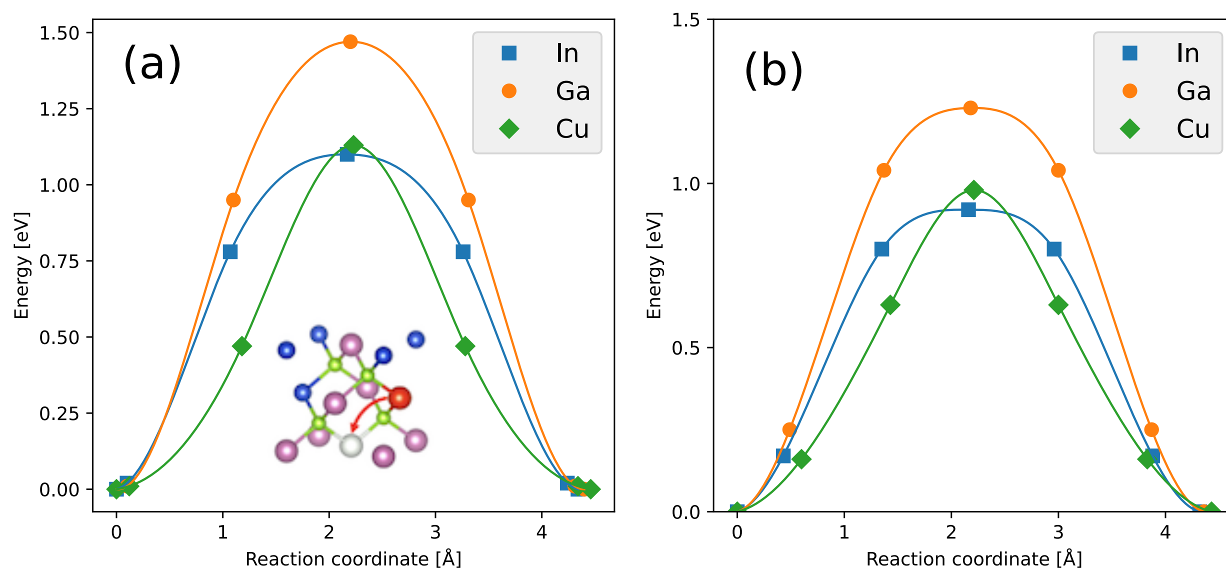

Figure 2.3: Diffusion paths for $[In/Ga/Cu]_{Cu}$-V_{Cu} processes in (a) CIS and (b) CGS. In the figure, the diffusing atom (red) moves into the vacant site (white). The surrounding atoms are copper (blue), indium (pink), and selenium (green).

the energy along the diffusion path taken by the moving antisite, and Table 2.3 shows the resulting migration barriers for the different processes. Our In_{Cu} and Ga_{Cu} barriers agree very well with

Table 2.3: Migration barriers and average distortion of antisite-vacancy exchange processes.

	E_m [eV]	Distortion (Å)		E_m [eV]	Distortion (Å)
CIS			**CGS**		
Ga	1.47	0.056	Ga	1.23	0.042
In	1.10	0.049	In	0.92	0.032
Cu	1.13	0.047	Cu	0.98	0.035

those of Refs. [7] and [46], and our V_{Cu} barriers agree with previous literature as well[5],[37],[60]. Although In_{Cu} and V_{Cu} have similar diffusion barriers, it is still expected that Cu diffusion occurs much faster than In diffusion. This arises due to most In in the crystal being immobile on group-III sites, so the overall diffusivity of In is significantly lower than the In_{Cu} antisite diffusivity, a point discussed further in Chapter 3. Two important observations can readily be made. First, the Ga process in CIS has a much higher barrier than the In process in CIS, and similarly the Ga process in CGS has a much higher barrier than the In process in CGS. Second, the In process in CIS has a higher barrier than the same In process in CGS, which is likewise true for the Ga process in CIS compared to the Ga process in CGS, and for the Cu process in CIS compared to the Cu process in CGS. Both observations can be explained by quantifying the "average distortion" that the lattice undergoes during the migration. To determine the average distortion of a given state, we calculated the distance every atom in a simulation cell is displaced from its ideal relaxed position. From this we determined the average displacement distance of an atom in the cell by averaging the displacements at all sites (excluding the sites involved in the exchange). Lastly, we found the change in average displacement between the ground and saddle states of each process, which we will refer to as the "average distortion" caused by the process. The results are presented in Table 2.3. Positive values of average distortion indicate a greater degree of average displacement in the saddle state compared to the ground state. We expect that a larger value of average distortion will correspond to a larger barrier, as the system must undergo a greater change from ideality

for the defect to migrate, which requires greater energy. In fact, this is exactly the trend that is observed. In both CIS and CGS, the In_{Cu} and Cu_{Cu} exchanges have similar barriers to each other, and correspondingly have similar values of average distortion. Meanwhile, in both CIS and CGS the Ga_{Cu} exchange has a significantly higher energy barrier than the equivalent In_{Cu} and Cu_{Cu} processes, and likewise has a significantly higher value of average distortion. Furthermore, all CIS processes have higher barriers than their equivalent CGS processes, and likewise the CIS processes have significantly greater average distortions than their CGS counterparts.

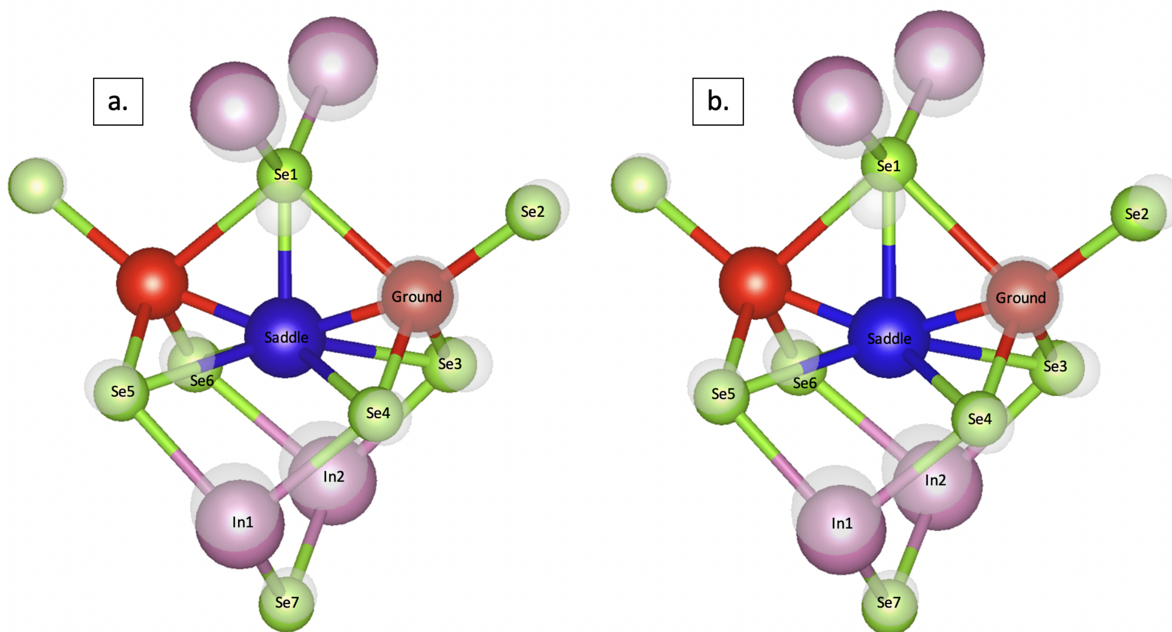

Figure 2.4: The saddle point configuration for (a.) Ga_{Cu}-V_{Cu} exchange and (b.) In_{Cu}-V_{Cu} exchange. The corresponding ground state configurations are overlaid semi-transparently. Color coding: Se (green), In (pink), Ga_{Cu} or In_{Cu} (blue), V_{Cu} (red). The 9 nearest-neighbors to the saddle and ground states are labeled.

Figure 2.4 shows the saddle and ground state configurations of Ga_{Cu}-V_{Cu} and In_{Cu}-V_{Cu} swaps in CIS. All six processes reported in Table 2.3 have qualitatively the same saddle point configuration. The migrating atom moves through the tetrahedral interstitial site, but at the saddle point, it is distorted away from the true tetrahedral site, towards the two vacancies. The distance between the

migrating atom and Se1 remains relatively constant throughout the migration, so that the migrating atom is effectively "pivoting" around this selenium. We find that for all six processes, the saddle point is symmetric between the initial and final states. This contrasts with Ref. [7], who find an asymmetric saddle point configuration for the Ga_{Cu} swap in CIS. This discrepancy may arise from differences in their calculation method from ours that are not reported, such as the lattice constants used and the degrees-of-freedom allowed to relax. They hypothesize that the large difference between Ga and In barriers in CIS may have some connection to this asymmetry, but since we find similar energy barrier differences with wholly symmetric configurations, the asymmetry may not be a key factor. As previously explained, we quantified the amount each atom was displaced from its ideal relaxed location. For both In and Ga migration processes, Se1 undergoes by far the greatest increase in displacement between the ground and saddle states, in line with its role as the "pivot" for the migrating atom. However, the average displacement of atoms in the In process ground state is much greater than that of the Ga process ground state, while the average displacement of atoms in the two saddles is more comparable. Because the In process begins already further from ideality, moving to the saddle does not require as large of an average distortion as for the Ga process, which begins closer to ideality in a more stable configuration (hence the higher migration barriers found for Ga compared to In processes). This trend is also observed in CGS, despite Ga being the native lattice species. Of the nine nearest neighbors labeled in Fig. 2.4, only Se2, Se3, and Se4 behave significantly differently between the In and Ga processes. As these three are all neighbors to the ground state (and in the case of Se2, not a neighbor to the saddle state), this confirms that the difference between In and Ga processes originates primarily with the ground state.

In addition to the 1NN hops, previous studies have found that 2nd-nearest-neighbor (2NN) hops of V_{Cu} have a comparable migration barrier to 1NN V_{Cu} hops, and therefore should be considered.

Table 2.4: Migration barriers for 2NN hops of a V_{Cu} defect at 1NN distance to Ga_{Cu}, In_{Cu}, or Cu_{Cu}.

	E_m [eV]		E_m [eV]
CIS		**CGS**	
1NN to Ga_{Cu}	1.22	1NN to Ga_{Cu}	1.31
1NN to In_{Cu}	1.25	1NN to In_{Cu}	1.32
1NN to Cu_{Cu}	1.18	1NN to Cu_{Cu}	1.17

We use "2NN" to refer specifically to the second-shortest distance between Cu sites, not to lattice connectedness. Of special interest is the situation where the initial and final sites of a 2NN V_{Cu} hop are both 1NN to the same antisite. Although there is no overall change in binding energy, the expected path approaches very closely to the antisite, and so the possibility of a distinctly different barrier from the isolated 2NN hop exists. Table 2.4 shows the barriers for 2NN hops of V_{Cu} in the presence of different antisites and native copper. Our value of 1.18 eV for a free 2NN V_{Cu} hop in CIS agrees well with Ref. [5]. In CIS, the presence of an antisite at 1NN increases the barrier only modestly, but it has a more substantial effect in CGS. This is likely due to the smaller lattice constants of CGS compared to CIS, which brings the antisite closer to the migrating atom and raises the energy. In both CIS and CGS, when an antisite is present, the migrating atom is distorted away from the antisite at the saddle point. In both cases, the saddle point configuration is asymmetric when an antisite is present, and the potential energy landscape around the saddle point is very flat and broad. Because 2NN hops only exist in *ab* planes (see Figure 3.1), the inclusion of 2NN hops in our models may impact anisotropy, as discussed in Chapter 3.2. 2NN hops of In_{Cu} and Ga_{Cu} were found to have such high barriers that they do not significantly impact group-III diffusion.

Chapter 3

Cu(In,Ga)Se_2: Diffusivity Models[1]

3.1 Methods and Model Selection

We now take the results of Chapter 2 to develop KLMC simulations of group-III diffusion. These KLMC simulations were performed using the open source KMCLib code[34]. This method assigns atomic species to fixed lattice positions, and advances the simulation by randomly choosing a migration process to perform, with the probability of selection weighted to be proportionate to the transition rate of the process. Allowed transition events and associated rate constants were determined from our DFT calculations. The binding energy between defects was treated by applying the coulombic model of interactions outlined previously. Our simulation considered only the Cu-sublattice, utilizing 1000 lattice sites with periodic boundary conditions in all directions, populated with a proportionate number of group-III antisites and vacancies for different compositions. The Cu-sublattice of CIGS has the connectivity of a diamond lattice but is elongated in the c-direction by a factor close to $\sqrt{2}$ (modified slightly by c/2a). 1NN hops are tetrahedrally

[1]Reproduced from A. S. Gehrke, D. E. Sommer, and S. T. Dunham, "Atomistic models of In and Ga diffusion in Cu(In,Ga)Se_2," *Journal of Applied Physics*, vol. 134, no. 11, p. 115 002, 2023, with the permission of AIP Publishing.

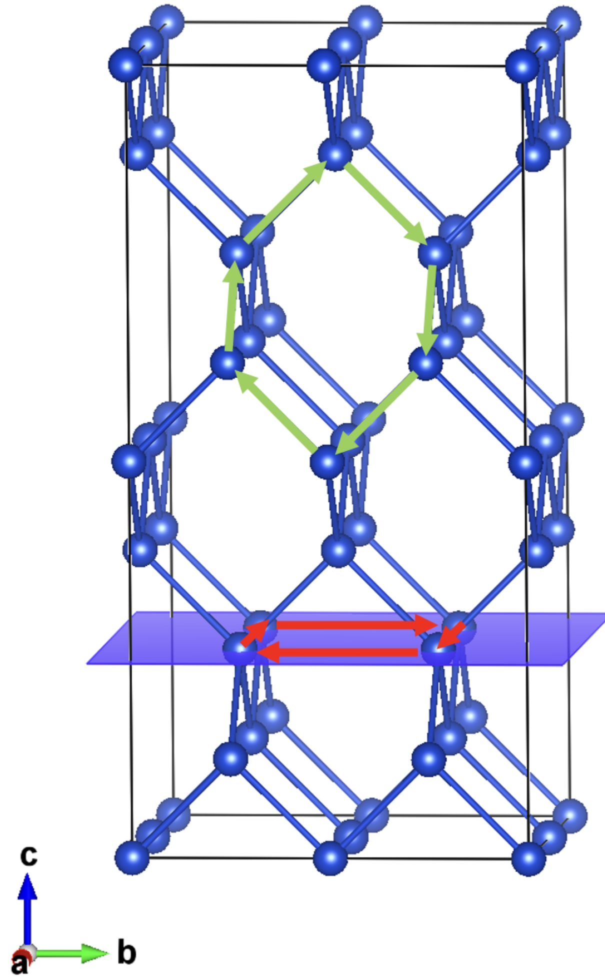

Figure 3.1: The Cu-sublattice of CIS. The green arrows depict the connectivity of 1NN sites, while the red arrows depict the connectivity of 2NN sites. Note that strictly 2NN diffusion is confined to the *ab* (blue) plane.

coordinated, while 2NN hops are confined to *ab* planes (see Figure 3.1). Allowed processes included 1NN In/Ga/Cu_{Cu}-V_{Cu} swaps and 2NN Cu_{Cu}-V_{Cu} swaps. Because many processes result in a change in the overall binding energy, in order to preserve detailed balance the migration barrier was estimated as the sum of the barrier of a free swap and half the change of the overall binding energy before and after the swap:

$$E_m = E_{m,free} + \frac{1}{2}\Delta E_b \tag{3.1}$$

where $E_{m,free}$ is the barrier of the isolated swap, and ΔE_b is the change in overall binding energy in the system. We tested this model against DFT calculations for a number of cases and found generally good agreement, with average error less than $k_B T$ even for the lowest temperatures simulated. Typical runs consisted of 10^6 steps to produce reliably converged values of the mean-squared displacement (MSD) of the group-III species. We obtained the diffusivity of the antisites via

$$D = \frac{1}{6t}\langle r^2 \rangle \tag{3.2}$$

where the MSD over time $\langle r^2 \rangle / t$ was extracted from the slope of the MSD vs time curve via least-squares regression.

Initially, the Chemical Constraint Calculator (CCC) as developed by Ref. [32] was to be used to ascertain the appropriate number of vacancies and antisites with which to populate the simulation, by considering defect thermodynamics in the canonical ensemble. However, several simplifications were found to apply which allowed for concentrations to be predicted simply from stoichiometry. Generally, the valence ratio[5] $2[\mathrm{Se}]/([\mathrm{Cu}] + 3([\mathrm{In}] + [\mathrm{Ga}]))$ is very close to unity in high-quality CIGS absorber material[3],[61], and the cation ratio $[\mathrm{Cu}]/([\mathrm{In}] + [\mathrm{Ga}])$ is copper poor (< 1). For these composition ranges, results from the CCC show that antisites and vacancies on the Cu-sublattice are overwhelmingly dominant compared to other defects. Consequently, the stoichiometry is necessarily fixed by the Cu-sublattice defect concentrations. For a valence ratio near 1, charge balance is maintained by having twice the concentration of singly negative charged copper vacancies as doubly positive charged group-III antisites on copper sites. Although the valence ratio may vary by a small amount above or below 1, because the simulation must be populated with an integer number of defects, these small variations in valence ratio do not typically

change the number of defects used in the model. Additionally, the CCC confirms that the ratio of $[\mathrm{Ga_{Cu}}]/([\mathrm{In_{Cu}}]+[\mathrm{Ga_{Cu}}])$ corresponds to the overall $[\mathrm{Ga}]/([\mathrm{Ga}]+[\mathrm{In}])$ (GGI) ratio (in other words the formation of In versus Ga antisites is equally favorable). Thus, the cation ratio is determined by the following:

$$\frac{[\mathrm{Cu}]}{[\mathrm{In}]+[\mathrm{Ga}]} = \frac{0.25-[\mathrm{V_{Cu}}]}{0.25+[\mathrm{In_{Cu}}]+[\mathrm{Ga_{Cu}}]} \tag{3.3}$$

$$2[\mathrm{V_{Cu}}] = [\mathrm{In_{Cu}}]+[\mathrm{Ga_{Cu}}] \tag{3.4}$$

$$\frac{[\mathrm{Ga_{Cu}}]}{[\mathrm{In_{Cu}}]+[\mathrm{Ga_{Cu}}]} = \mathrm{GGI} \tag{3.5}$$

This system is fully specified for a given cation ratio and GGI ratio, and the concentration of vacancies and antisites with which to populate the simulation can be readily obtained.

To account for alloyed CIGS, we considered how the formation energies and migration barriers of the relevant defects vary with GGI. Our DFT calculations show no energy change when exchanging $\mathrm{Ga_{Cu}}+\mathrm{In_{III}} \rightarrow \mathrm{In_{Cu}}+\mathrm{Ga_{III}}$ or $(\mathrm{Ga_{Cu}}+\mathrm{V_{Cu}})_{1NN}+\mathrm{In_{III}} \rightarrow (\mathrm{In_{Cu}}+\mathrm{V_{Cu}})_{1NN}+\mathrm{Ga_{III}}$, suggesting $\mathrm{In_{Cu}}$ and $\mathrm{Ga_{Cu}}$ antisites form with equal favorability. Refs. [60] and [40] have confirmed that $\mathrm{In_{Cu}}$ and $\mathrm{Ga_{Cu}}$ have formation energies similar to each other in both CIS and CGS, and that the formation energy of $\mathrm{V_{Cu}}$ is the same in both CIS and CGS. Likewise, Refs. [62] and [63] have found that in bulk group-III rich (thus Cu poor) CIS or CGS, the formation energy of $\mathrm{V_{Cu}}$ is unchanged over a wide range of Fermi energies in both CIS and CGS, and likewise the formation energy of $\mathrm{In_{Cu}}$ in CIS is similar to that of $\mathrm{Ga_{Cu}}$ in CGS. Taken together, these findings suggest that defect concentrations are unaffected by changes in GGI outside of the change in antisite ratio reflected by Eq. 3.5. Additionally, previous Monte Carlo studies suggest that for temperatures above the range of interest considered here (>400K), In and Ga mix homogeneously on the III-sublattice. Therefore, we are justified in only considering system-level GGI and ignoring the possibility of lo-

cal GGI variation[64]–[66]. However, because there is a large variation in migration barriers between CIS and CGS, for the given GGI we used a linear interpolation of the barriers between their CIS and CGS endpoints. This assumption was confirmed by running several NEB calculations with randomly arranged In and Ga atoms (corresponding to a GGI of 0.375) on group-III sites. The average barrier for the In_{Cu}-V_{Cu} swap was nearly identical to the value expected from a linear interpolation, likewise for the Ga_{Cu}-V_{Cu} swap.

A difficulty that arose was developing a fast and efficient algorithm to calculate the binding energy of the system, given our coulombic binding model. The long-range r^{-1} decay of coulombic interactions requires a sufficiently long cutoff to achieve well-converged results, but this can be computationally intensive. We implemented the approach outlined by Ref. [55], which requires only finding the electrostatic potentials at the two sites on which the process occurs, including only the stationary charges up to a certain cutoff. The cutoff is defined radially from the point halfway between both sites, so that the total charge used to evaluate both sites is unchanged. This has been shown to speed convergence[55]. Figure 3.2 shows convergence of the calculated diffusivity of In for increasing cutoff. As can be seen, above 20 angstroms the results show tight convergence. All the following calculations used 20 angstrom cutoffs to ensure the best results.

3.2 In and Ga Diffusivity

We calculated diffusivities for In and Ga in CIS over a range of compositions and temperatures using our KLMC model. We chose to report Ga diffusivity in CIS as opposed to in CGS in order to have a direct comparison between In and Ga diffusivity, and due to the lack of experimental data for diffusivity in very high Ga content CIGS. To be completely physically realistic, a very

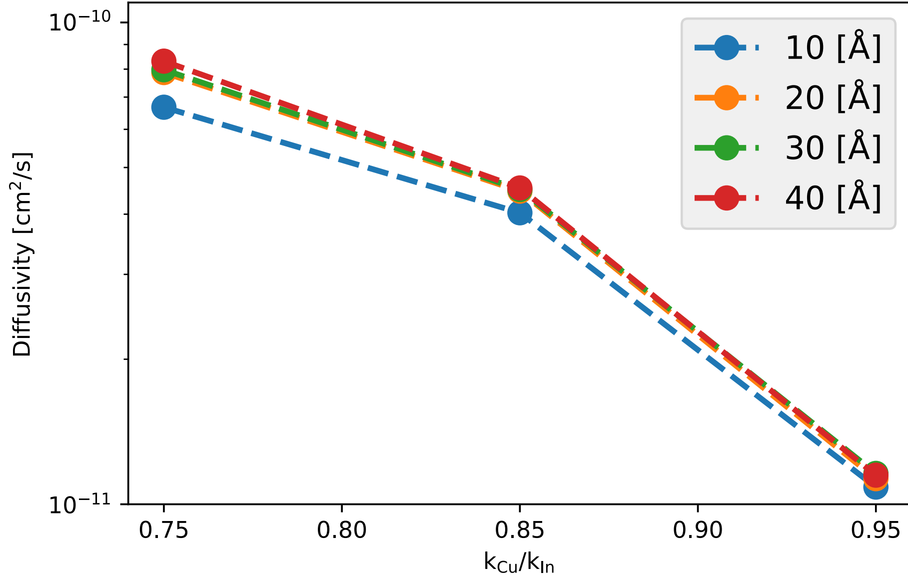

Figure 3.2: Convergence of the diffusivity of In from KLMC simulations at 1000K, for increasing cutoff radius, as a function of the cation ratio k_{Cu}/k_{In}.

small number of Ga atoms should have been added to the simulations to reflect a dilute Ga content that does not alter the overall properties of the bulk CIS system. However, it was found to be difficult to obtain sufficient statistics to estimate the MSD with such low Ga content. We decided instead to artificially convert all antisites to Ga while still maintaining CIS parameters, in order to obtain more robust MSD data. Since our simulation has both In_{Cu} and Ga_{Cu} bind via the same electrostatic interactions, the equilibrium configuration of defects should only depend on the overall concentration of vacancies and antisites, not the ratio of Ga_{Cu}/In_{Cu}. In turn, as the hop rate of an individual diffusing Ga_{Cu} antisite only depends on temperature and the neighboring defect configuration, conversion of In_{Cu} to Ga_{Cu} should not affect Ga diffusivity. A run with half Ga_{Cu} and half In_{Cu} antisites confirmed that no change in Ga diffusivity occurs from a change in the ratio of Ga_{Cu}/In_{Cu}.

Figure 3.3 shows results from the simulations for different temperatures and compositions. Figure 3.3a depicts the diffusivity of antisites, which is simply the diffusivity of the indicated

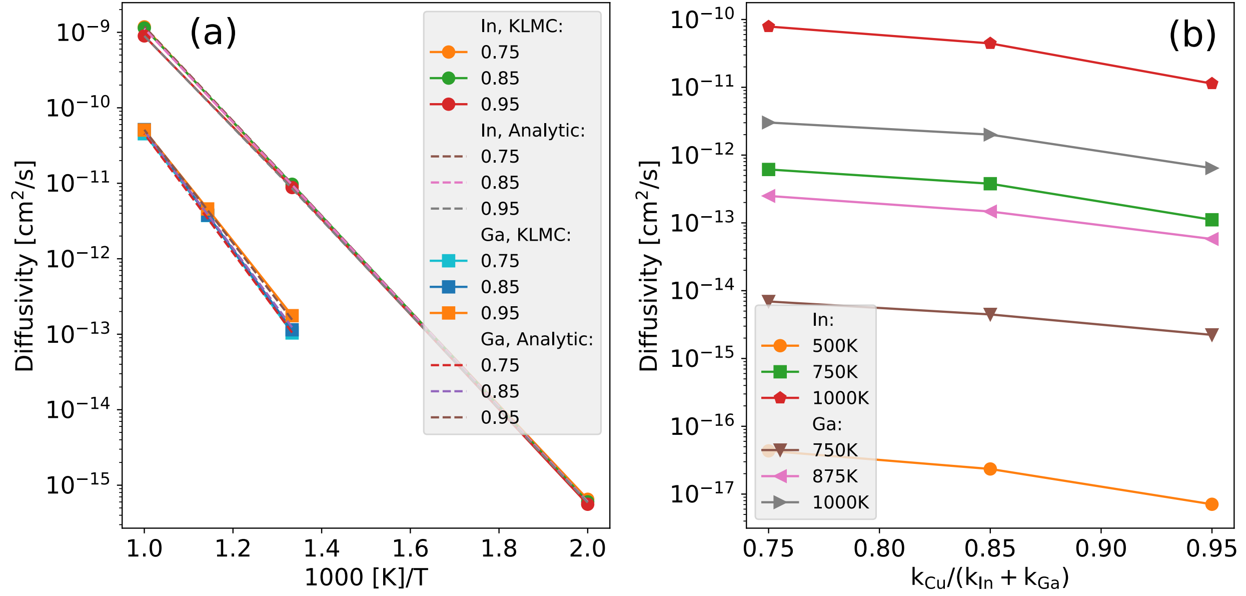

Figure 3.3: Diffusivity of In and Ga in CIS. (a) the diffusivity of antisites, as calculated from both KLMC and analytic models, for k_{Cu}/k_{In} ratios of 0.75-0.95. (b) the overall diffusivity of In and Ga versus composition, as calculated from KLMC.

species extracted from the KLMC simulations, as given in Eq. 3.2. Figure 3.3b gives the overall diffusivity, which is the antisite diffusivity multiplied by the fraction of the diffusing species that is mobile. This takes into account the fact that most of the In and Ga in the system exists frozen on the III-sublattice and does not contribute to diffusion; thus the overall diffusivity is lower than the antisite diffusivity. It can be readily observed that the diffusivity of antisites (Figure 3.3a) is mostly independent of the cation ratio, suggesting that the diffusing behavior of an individual antisite is not strongly affected by the density of other antisites and vacancies nearby, at least within these composition ranges. Therefore, the compositional dependence of the overall diffusivity of In and Ga in CIGS (Figure 3.3b) is primarily due to the availability of mobile antisites, which increases in more Cu-poor material. Ref. [3] finds a severalfold decrease in the diffusivity of Ga in CIS at 1000K when increasing the k_{Cu}/k_{In} ratio from 0.75 to 0.95, which is generally consistent with our findings. It is also evident from our results that Ga diffusion is predicted to be a couple orders of

magnitude lower than In diffusion in CIGS having the same composition, which is consistent with experimental observations. We discuss this in greater detail below.

The activation energies for In and Ga diffusion were found from the average of the 3 Arrhenius slopes for different compositions. In diffusion was found to have an activation energy of 1.24 eV, and Ga diffusion a value of 1.54 eV. These activation energies are quite reasonable. For In diffusion, the activation energy of 1.24 eV is noticeably higher than the migration barrier of 1.1 eV as listed in Table 2.3, whereas for Ga the value of 1.54 eV is closer to the barrier of 1.47 eV. When an antisite swaps with a vacancy, if the exchange does not bring the antisite into contact with a new vacancy, it is likely to simply reverse the swap with the original vacancy, leading to no net diffusion. For long-range diffusion to occur, after an antisite-vacancy exchange the vacancies must re-orient themselves to provide a pathway for a subsequent exchange that does not merely reverse the prior swap[67]. Because there are a variety of mechanisms for this to occur, it is difficult to determine a single barrier to this re-orientation process. These mechanisms include an antisite capturing a vacancy from far away, a vacancy disassociating from an antisite, and a vacancy orbiting around an antisite to a different 1NN location. Furthermore, the rates of all these mechanisms are influenced by the local defect landscape. A benefit of KLMC is its ability to capture all these complex behaviors with a relatively simple model. Despite this complexity, even using just NEB calculations of a few representative processes suggests that these mechanisms generally fall in the range of 1.2-1.3 eV. For In diffusion, the low migration barrier causes the In antisites to swap back and forth many times before a vacancy can re-orient itself on a new site. Therefore, the overall diffusion of In is limited by the effective "vacancy re-orientation" barrier, readily explaining why the activation energy is in the range of 1.2-1.3 eV. With Ga however, the migration barrier is so high that after a Ga_{Cu}-V_{Cu} exchange, the vacancies will re-orient many times

Table 3.1: Correlation factors for In and Ga diffusion, at selected temperatures and a composition of k_{Cu}/k_{In} = 0.85.

T[K]	In	Ga
500	0.21	1.00
750	0.31	0.98
1000	0.36	0.93

before the Ga exchanges again, and subsequent Ga hops will be equally likely in any direction. Thus, the overall diffusion of Ga is limited by Ga_{Cu}-V_{Cu} exchange, and so the activation energy is nearly the exchange energy.

This explanation can be confirmed by calculating the correlation factors (as defined in Eq. 1.2) of sample KLMC runs. As the fraction of hops that are reversals increases ($\cos(\theta) \to -1$), f tends to 0, while as hops become increasingly uncorrelated (each hop is independent of the previous hop, $\langle\cos(\theta)\rangle \to 0$), f tends to 1. The cosines are accumulated over the course of a KLMC run. We expect In runs to have fairly low values for f, corresponding to frequent reversals, while we expect Ga runs to have f values near 1, corresponding to nearly uncorrelated hops. Table 3.1 shows calculated correlation factors for representative systems and confirms that In antisites experience far more reversals than Ga antisites.

It was also observed that when considering *a*, *b*, and *c* axis diffusion separately, the diffusivity in the *c* direction was generally between 1.5-2 times higher than that in the *a* or *b* direction. As mentioned previously, because the Cu-sublattice of CIGS is identical to the diamond lattice elongated by a factor of about $\sqrt{2}$ in the *c* direction, each 1NN hop moves the defect proportionately more along the *c* direction than along the *a* or *b* directions. Thus, it is expected that about a 2-fold higher diffusivity would be observed in the *c* direction. For In, the doubling of the *c* direction diffusivity is depressed to only a 1.5-1.9 factor increase. This is believed to be due to the effect of 2NN V_{Cu} hops, which provide additional pathways for vacancy reorientation in the *ab* plane

only, boosting *ab* diffusivity by increasing the frequency of uncorrelated hops. For Ga, a simple 2-fold *c* direction increase is observed, explained by Ga diffusion being primarily limited by Ga/V exchange rather than V reorientation. These results suggest the possibility of anisotropic diffusion in CIGS, which is particularly interesting as we have not identified any work that recognizes such behavior in CIGS.

3.3 Analytic Models

To extend the results of our KLMC models into higher-order continuum models, we sought to estimate the temperature-dependent diffusion coefficient for In and Ga in CIGS using analytic models. We used Eq. 1.1 to model the diffusivity, with g equal to $\frac{1}{6}$ for 3D diffusion, $\lambda = 4.167\,\text{Å}$, ν estimated as the typical Debye frequency ($\nu_0 \approx 10\,\text{THz}$), and ΔE_m chosen for the desired complex and charge state.

We assumed that the migration barrier of a complex can be replaced by an effective activation energy for uncorrelated hops that causes $f = 1$. Essentially, this effective activation energy reflects the rate that uncorrelated hops occur between stretches of (potentially many) reversals. To predict p_d for the different defect complexes, we developed a simple equilibrium reaction model. For this model, we considered only 1NN single- and double-vacancy complexes along with unbound antisites and unbound vacancies, allowing triple-vacancy and higher complexes to be subsumed under the double-vacancy complex concentration. We also assumed that vacancies do not neighbor more than one antisite at any time, which is generally true given strong antisite-antisite repulsion. The formation of complexes is defined by the following equilibrium reactions:

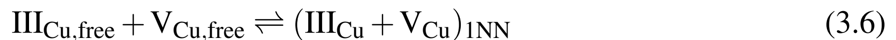

$$\mathrm{III}_{\mathrm{Cu,free}} + \mathrm{V}_{\mathrm{Cu,free}} \rightleftharpoons (\mathrm{III}_{\mathrm{Cu}} + \mathrm{V}_{\mathrm{Cu}})_{\mathrm{1NN}} \tag{3.6}$$

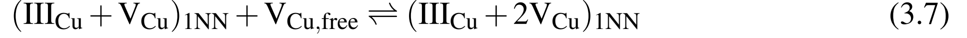

$$(\mathrm{III_{Cu}} + \mathrm{V_{Cu}})_{\mathrm{1NN}} + \mathrm{V_{Cu,free}} \rightleftharpoons (\mathrm{III_{Cu}} + 2\mathrm{V_{Cu}})_{\mathrm{1NN}} \tag{3.7}$$

from which the following model was generated:

$$[\mathrm{III_{Cu}}] = [\mathrm{III_{Cu,free}}] + [1\mathrm{V}] + [2\mathrm{V}] \tag{3.8}$$

$$[\mathrm{V_{Cu}}] = [\mathrm{V_{Cu,free}}] + [1\mathrm{V}] + 2[2\mathrm{V}] \tag{3.9}$$

$$[1\mathrm{V}] = K_1[\mathrm{V_{Cu,free}}][\mathrm{III_{Cu,free}}] \tag{3.10}$$

$$[2\mathrm{V}] = K_2[\mathrm{V_{Cu,free}}][1\mathrm{V}] \tag{3.11}$$

$$K_1 = A_1 e^{-E_1/k_B T} \tag{3.12}$$

$$K_2 = A_2 e^{-E_2/k_B T} \tag{3.13}$$

where $[\mathrm{III_{Cu}}]$ and $[\mathrm{V_{Cu}}]$ are the total concentrations of $\mathrm{III_{Cu}}$ (group-III species: In and Ga) and $\mathrm{V_{Cu}}$ respectively, $[\mathrm{III_{Cu,free}}]$ and $[\mathrm{V_{Cu,free}}]$ are the concentrations of unbound $\mathrm{III_{Cu}}$ and $\mathrm{V_{Cu}}$ respectively, and $[1\mathrm{V}]$ and $[2\mathrm{V}]$ and the concentrations of $\mathrm{In_{Cu}} + \mathrm{V_{Cu}}$ and $\mathrm{In_{Cu}} + 2\mathrm{V_{Cu}}$ complexes respectively. Equilibrium values for $[\mathrm{III_{Cu,free}}]$, $[1\mathrm{V}]$, and $[2\mathrm{V}]$ were extracted from KLMC simulations run under varying $[\mathrm{III_{Cu}}]$, $[\mathrm{V_{Cu}}]$, and T values, and used with Eqs. 3.8, 3.9, 3.10, and 3.11 to numerically solve for values of K_1 and K_2 as functions of T. From Arrhenius plots of these results, eqs. 3.12 and 3.13 gave values of $A_1 = 5.42$, $E_1 = -0.25$ eV, $A_2 = 1.05$, and $E_2 = -0.29$ eV. E_1 and E_2 can roughly be interpreted as the "effective binding energies" for the complexes given only 1NN interactions. Compared with the values of -0.51 eV and -0.85 eV in Table 2.2, it is clear that the presence of long-range interactions substantially reduces the favorability of complex formation. This is expected, as the slow decay of the coulomb interaction allows complexes to

partially dissociate without much penalty in terms of energy increase. To test the validity of this model, we solved Eqs. 3.8, 3.9, 3.10, and 3.11 simultaneously in MATHEMATICA[68] using our calculated parameters for different compositions and temperatures. The results in Fig. 3.4 compare

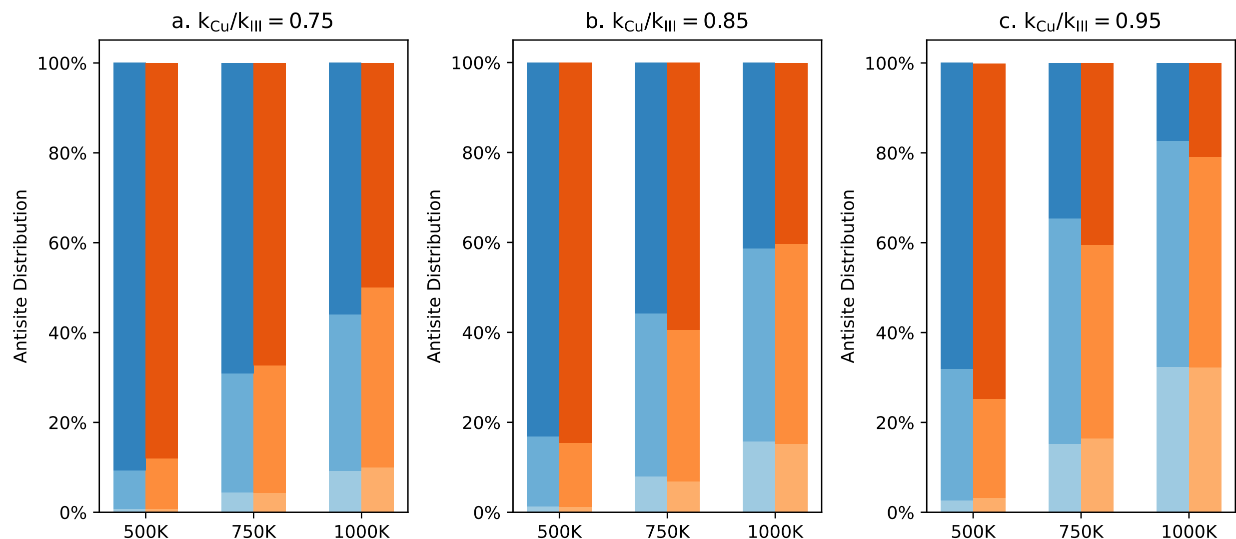

Figure 3.4: Equilibrium distribution of defect complexes in CIS, at different temperatures and compositions. The left-hand (blue) bars depict results from KLMC simulations, while the right-hand (orange) bars depict results from the proposed analytic model. All III_{Cu} antisites in the system are distributed as either unbound (free) antisites (lightest shading, on the bottom), in single-vacancy complexes (medium shading, in the middle), or double-vacancy and higher complexes (heaviest shading, on the top). The percentages correspond to the fraction of total antisites found in each configuration at equilibrium.

the KLMC equilibrium distributions of complexes with those found from our model. They agree very well, with an average error of only 10.3% between KLMC and our analytic model. The proposed model should be quite suitable for use in a continuum reaction-diffusion simulation.

We defined two free parameters for the effective activation energies of 1V and 2V+ complexes and fit the analytical model to the KLMC results for different temperatures and compositions by minimizing the total percent error. For In, the solution converged on identical activation energies for 1V and 2V+ of 1.26 eV, which is also nearly identical to the overall activation energy of 1.24 eV found directly from the KLMC simulations. The average percent error in the diffusivity from the analytic versus the KLMC model is only 2.9%. As explained previously, because the diffusion

of In is limited by the effective "vacancy-reorientation" barrier, not the antisite-vacancy exchange, both 1V and 2V+ complexes have the same limiting barrier, so the results we found are expected.

For Ga, we found a 1V effective activation energy of 1.47 eV and a 2V+ energy of 1.75 eV. The average percent error in the diffusivity is 4.4%, similar to the In diffusivity error. The difference of effective activation energy here is also reasonable. The 1V activation energy is identical to the 1V antisite-vacancy exchange barrier because overall diffusion of Ga is limited by the antisite-vacancy exchange barrier. The 2V+ antisite-vacancy exchanges have higher barriers because they require changes in binding energy that increase the barrier by about 0.15 eV for a 2V complex hop, and even higher for 3V+ hops, in line with the value of 1.75 eV found for 2V+ complex activation energies. An interesting consequence of this higher activation energy for 2V+ complexes is that diffusion of Ga is dominated by 1V complex hopping. Even at 300K, when our model predicts 98.7% of antisites should be in 2V+ complexes, diffusion is surprisingly still dominated by 1V complexes, which account for 99.8% of the diffusivity at this temperature. Figure 3.3 plots the analytic models against the KLMC results, which show very good agreement.

3.4 Comparison to Experiment

To validate our models against experimental results, we performed simulations to match the conditions of the In radiotracer diffusion study by Ref. [4]. In this work they report temperatures for each run and a GGI value of 0.3. They do not give values for valence ratio or cation ratio, but the process cited for the fabrication of their samples[69] is known to produce CIGS with valence ratio of nearly 1 and cation ratio of 0.85[70]–[73]. Therefore, we found it a reasonable comparison to use these values of valence ratio, cation ratio, and GGI in our simulations. Figure 3.5 shows the

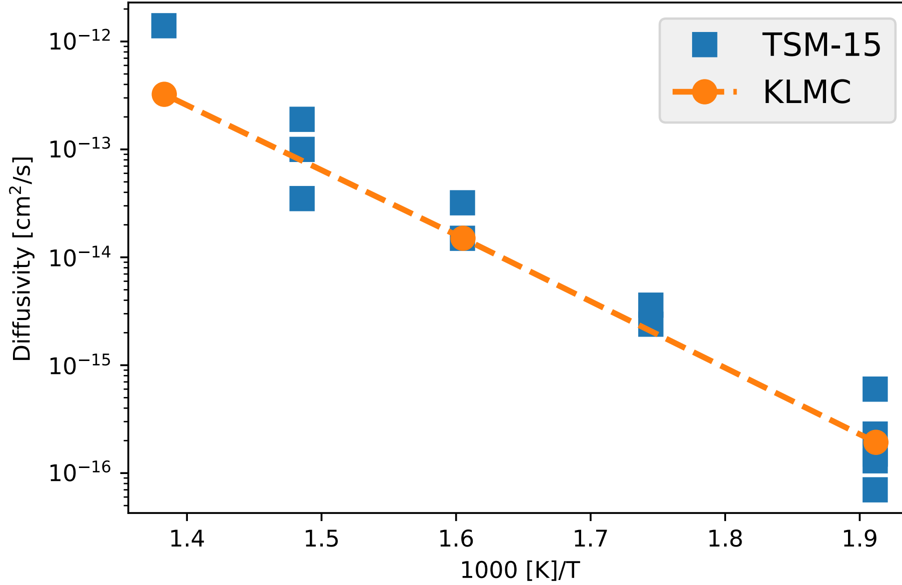

Figure 3.5: Comparison of our KLMC results with experimental radiotracer diffusion of In in CIGS from TSM-15 [Ref. [4]].

comparison of our KLMC models with their experimental results. We find an excellent agreement between our model and the reported data. Because our KLMC model relies solely on values calculated from *ab initio* methods (with the exception of the experimental dielectric constant, which itself falls within a narrow range of values and is not observed to strongly influence diffusivity in the simulations), these results provide strong evidence for the validity of our model for In diffusion in CIGS. Although we could not find studies on tracer diffusion of Ga in CIGS, there exist several studies on various types of in- and inter-diffusion of Ga. While these studies show a wide range of reported values, most suggest a diffusivity of Ga much smaller than that of In, consistent with our findings shown in Figure 3.3[3],[36],[70],[74]–[76]. Ref. [70] finds an activation energy for Ga in-diffusion from GaAs into single-crystal CIS of 1.49 eV, very close to our value of 1.54 eV for Ga tracer diffusion. Future work will involve developing continuum models to reproduce the specific design of these in- and inter-diffusion experiments, allowing for a more direct comparison between model and experiment.

Chapter 4

$Cu(In,Ga)Se_2$: Group-III Sublattice Ordering

4.1 Introduction

Having developed a robust model of diffusion on the Cu-sublattice of CIGS, we now turn to the challenge of extending our KLMC model to include the III-sublattice (i.e. the In/Ga-sublattice) as well. Even though significant diffusion of In and Ga is not expected to occur via these sites, by including the III-sublattice explicitly we can observe the In/Ga ordering that arises from the interactions between the species in the system. Understanding the local variations in In and Ga concentration is crucial to optimizing solar cell device performance, as the band gap is larger in regions of higher Ga content[6]. Consequently, precise control of the In/Ga ordering is necessary, which requires detailed understanding of the mechanisms contributing to ordering. KLMC can help elucidate these mechanisms. In particular, a long-term goal would be to develop a model that predicts the local fluctuations in GGI ratio expected under varying temperature and composition.

With such a model, it could then be possible to predict the local fluctuations in band gap and their resulting impacts on device performance.

In KLMC, adding the III-sublattice is straightforward, requiring simply to add these sites to the basis set and randomly populate them with the appropriate number of In and Ga types given the global GGI ratio desired. Because diffusion of In and Ga in CIGS has been shown to occur primarily on the Cu-sublattice (see Chapter 1.1), we do not need to add any hopping mechanisms on the III-sublattice. Likewise, the overwhelming majority of defects can be expected to occur on the Cu-sublattice (see Chapter 3.1), allowing the III-sublattice to simply be populated only with In and Ga types. However, to correctly capture the kinetics of the full system, we would need to add mechanisms allowing for interchange of In/Ga between the two sublattices. We are initially only interested in the equilibrium configurations on the III-sublattice, and so we can exclude these interchange mechanisms at first. Instead, we can artificially drive the system to equilibrium by allowing In-Ga exchanges on the III-sublattice. We can choose a migration barrier similar in magnitude to the Cu-sublattice hops, such as 1 eV, in order to obtain approximate parity between the frequency of Cu-sublattice and III-sublattice hops. In actuality, an In or Ga would first hop to the Cu-sublattice, diffuse some distance, and hop back to the III-sublattice in a new location. Our approach accelerates this process by allowing In and Ga to move directly to lower-energy locations, bypassing the Cu-sublattice diffusion steps. Although such a model will not have accurate kinetics, and therefore a KLMC implementation is not necessary, by developing the model in a KLMC framework it will be easy to extend it in the future to include the full kinetic picture.

4.2 III-Sublattice Interactions Model

To build the KLMC simulation, and especially to understand the nature of In/Ga ordering in CIGS, it is essential to have a good model of the binding interactions between the species in the simulation. We have already demonstrated a coulombic model of interactions between the Cu-sublattice defects. For III-sublattice interactions, we are primarily interested in low-Ga content situations (a GGI ratio less than 0.5). Thus, by treating In_{III} as the native species and Ga_{III} as a defect species, we only need to consider interactions between Ga_{III}-Ga_{III} and Ga_{III}-V/In/Ga_{Cu}. For example, if it is favorable for Ga_{III} to be near another Ga_{III} compared to being near a In_{III}, the binding energy of Ga_{III}-Ga_{III} (at that distance) will be negative, and positive if it is unfavorable. Unlike the coulombic interactions among the charged Cu-sublattice defects, Ga_{III} is uncharged, and so binding interactions involving it are not expected to have a significant coulombic component and are expected to be fairly short-ranged. As a result, we only need to consider the first few nearest neighbors for each interaction type.

We used VASP to calculate the binding energies, following the same methodology as outlined in Chapter 2.2 for PBE-GGA. 64-atom cell calculations were performed with a 4 x 4 x 4 Monkhorst-Pack *k*-point mesh, 256-atom cell calculations with a 3 x 3 x 2 mesh, and 512-atom cell calculations with a 2 x 2 x 2 mesh. Real space projection operators were used, with the error confirmed to be well below 1 meV/atom, and therefore suitable to use. For calculations involving only a small number of defects (around 0.5% or less of all sites) the pristine CIS lattice constants were used. For calculations involving large defect concentrations, all runs with the same total number of defects of each type (i.e. the same overall composition) were initially run with the lattice constants allowed to relax. The average value was calculated, and all the runs were rerun with lattice constants fixed at the average values. The calculated lattice constants used are given in Table

Table 4.1: Average value of the lattice constants for the different cell sizes and compositions used to develop the interaction model. The table lists the number of atoms in the cell, the dimensions of the cell relative to a cubic 64-atom cell, the cation ratio, the GGI ratio, and the lattice constants in the a, b, and c directions (in units of Å). The valence ratio is nearly equal to 1 in every case.

# Atoms	Dimensions	k_{Cu}/k_{III}	GGI	a, b	c
64	1 x 1 x 1	0.76	0.25	11.64	11.68
256	$\sqrt{2}$ x $\sqrt{2}$ x 2	0.76	0.25	16.47	23.38
512	2 x 2 x 2	1.0	0.0	23.52	23.68

4.1.

To develop the model, we initially looked at separating defect pairs in large 512-atom cells of pure CIS. The large size of the cells allowed us to calculate the change in energy between the pairs being at close distance and being far apart (greater than 17 Å separation). As explained above, we fixed the lattice constants for all cells to the pristine CIS values, so that the energy of different runs could be compared. By extracting the external pressure on the cell, we determined that the global strain energy due to the defects was very small, and more importantly did not change upon separating a defect pair. Thus, any change in energy upon separating a pair could be assumed to arise from local strain interactions (as coulombic interactions are expected to be negligible), which are precisely what we are trying to capture. To evaluate whether these interactions behave additively, we then looked at separating 3-defect pairs in different bound configurations out to far separation distances (with all 3 defects further than 9 Å from any other defect). Although we had initially just been looking at 1NN binding, these 3-body tests revealed that higher-neighbor interactions were significant. In particular, we observed that for some defect pairs, such as Ga_{III}-Ga_{III}, the sign of the binding oscillated for different interaction distances: at 1NN it might be positive, while at 2NN it might be negative, for example. To capture these more complex behaviors, we decided to test binding interactions up to 5NN distances (note that here, neighbors are being considered only on the cation sublattices; between any "1NN" pair is a Se atom).

Once we had determined the approximate pairwise interactions for the different pairs involving Ga_{III} out to 5NN in CIS, we then looked at modifying these interactions to predict the behavior in cells with more realistic Ga alloy concentrations and Cu-sublattice defect concentrations. As shown in Table 4.1, we first looked at 64-atom cells with 0.25 GGI ratio and 0.76 cation ratio (generally representative of high-performance PV material). For this, we would run 4 different runs in VASP, each with the same In/Ga_{Cu}-2V_{Cu} 1NN complex but different random Ga_{III} configurations. By comparing the energy change between these 4 runs, we could isolate the effect of different Ga_{III} configurations while fixing the interactions among Cu-sublattice defects. Our model can predict the energy change between two configurations by adding up the different pairwise interactions in a given cell, and the predicted energy change can be compared to the actual energy change given by DFT. By tuning the pairwise interaction parameters, we minimized the mean squared error (MSE) per cation in the cell between our model and DFT for a large number of different runs.

In KLMC, the simulation will spend the vast majority of the time in or near the lowest-energy configurations, especially at lower temperatures. Consequently, we desire for our model to be particularly tuned for correctly representing these near-equilibrium configurations. Once we had obtained a reasonably good model using the previously described procedure, we set up small KLMC runs with 256 atom cells (see Table 4.1) using the optimized interaction parameters. We first allowed the simulations to reach equilibrium at 300K, and then froze in the Cu-sublattice and continued running to generate a number of different low-energy III-sublattice arrangements for the same low-energy Cu-sublattice arrangement. By doing so, we could compare the energy change between low-energy structures that all possess the same Cu-sublattice configuration but different III-sublattice configurations. We have already developed a coulombic model for Cu-sublattice interactions in Chapter 2.3, and this approach allows us to remove any errors that might arise from

modeling Cu-sublattice changes with coulombic interactions, and instead focus solely on modeling changes on the III-sublattice. We then took samples of these structures and relaxed them in VASP, allowing us to repeat the optimization procedure (as previously described) specifically for lowest-energy defect configurations. This was an iterative process: after each optimization the procedure was repeated.

To test the validity of the model, at each iteration we divided all the data up into N subsets, and fit the parameters to $N-1$ subsets while testing the goodness of the fit on the remaining subset. We repeated this for each of the N subsets, and determined the average MSE/cation across all subsets. In order to weight the KLMC runs more heavily (which are the most representative of the conditions we ultimately hope to use the model on), all the runs involving separation of defect pairs were combined into a single subset, and all the runs involving three or more defects but not originated from KLMC were also combined into another subset. These first two subsets contained 20 and 50 data points, respectively, and each was weighted as 1x. Each iteration of KLMC runs then created two additional subsets, where each subset contained 12 data points and was weighted as 2x. This weighting was found to produce the optimal results, and prioritizes the KLMC data. Ultimately, 4 iterations leading to 8 subsets of KLMC data were needed to reach an optimized and converged model, for a total of 10 subsets and 166 data points used to create the final model.

To optimize the model, we carefully tuned the number and type of parameters included to obtain the best MSE/cation results. First, we looked at varying the interaction distance of the parameters to include. As shown in Figure 4.1, the MSE/cation improved up to inclusion of 4NN, but the model fit degraded when 5NN was added. Therefore, we determined that inclusion of neighbors up to 4NN produces the best fit. Additionally, we found that including two second-order terms for the largest parameter values (note that these parameters were only the largest before

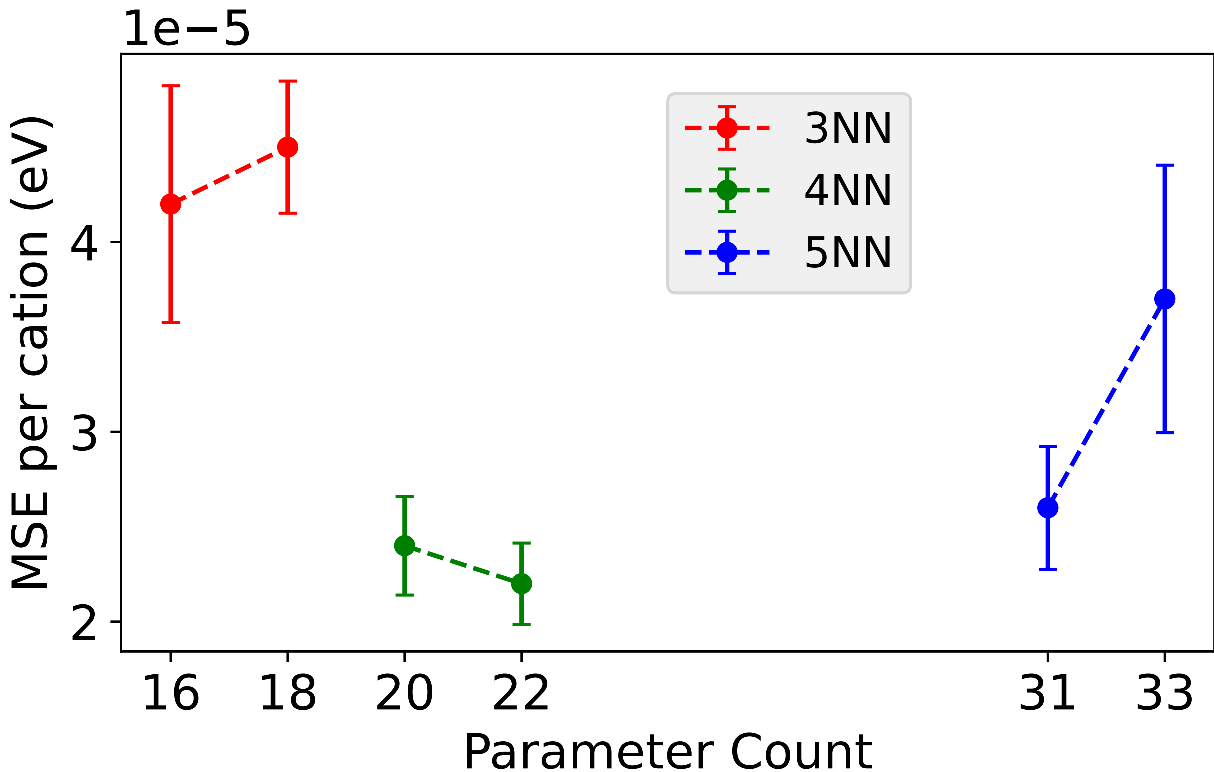

Figure 4.1: Average MSE/cation in the test data as a function of the parameter count. 3NN, 4NN, and 5NN specify the interaction distance up to which nearest-neighbors are included. The first point in each pair at the same maximum nearest-neighbor distance excludes second-order terms, while the second point includes them (adding 2 additional parameters).

the inclusion of second-order terms) also improved the model. These are terms that scale as the number of pairs squared, rather than simply as the number of pairs. We added these terms to 1NN type 1 Ga_{III}-Ga_{III} and Ga_{Cu}-Ga_{III} interactions. While these terms actually degrade the fit when added to 3NN and 5NN models (shown in Figure 4.1), the best overall model was found for 4NN with the second-order terms included. We also tested whether inclusion of valence cluster terms would improve the MSE/cation. Ideal CIGS is ionic, with Se^{-2} anions balancing equal parts Cu^{+1} and In/Ga^{+3} cations. In ideal CIGS, the average cation valence is +2. Valence cluster terms for each cation are parameters that are proportional to the square of the deviation of the local valence around a cation from the ideal valence. This local neighborhood includes the cation itself and the

Table 4.2: Optimized interaction energies (meV). Note that for certain distances, there are multiple types. These types correspond to symmetrically-distinct pairs, where the change in the *c*-direction is different between types. The squared term indicates that it is a second-order parameter.

Distance	Ga_{III}-Ga_{III}	V_{Cu}-Ga_{III}	Ga_{Cu}-Ga_{III}	In_{Cu}-Ga_{III}
1NN type 1	7	-2	14	3
$(\text{1NN type 1})^2$	1		4	
1NN type 2		-5	7	-5
2NN	-10	2	-10	5
3NN type 1	-5	0	-7	-2
3NN type 2	-4			
4NN	8	-2	6	-6

12 nearest-neighbor cations. These parameters are effectively a positive energy cost to the system for having locally off-stoichiometric valence. However, we found that inclusion of these terms significantly degraded the fit. Additionally, the terms were highly unstable, varying dramatically depending on the subsets of data included in a fit. Therefore, we decided to exclude valence terms from the model.

Table 4.2 gives the final values of the model parameters. These were obtained by fitting all 10 subsets of 166 data points at once. We also tested the stability of the parameters by excluding 1 subset at a time, following the method described previously, to quantify how much the parameters fluctuated depending on the exact data included in the model. The average ratio of the uncertainty of a mean to the mean itself for the parameters derived in this way was only 16%, confirming that the parameters are reasonably stable. An additional 24 data points were generated for testing from KLMC using the final model parameters. These data produced a MSE/cation of 1.5×10^{-5}, which is a further improvement upon the best model depicted in Figure 4.1. Thus, we now have a model suitable for use in larger KLMC simulations.

4.3 Kinetic Lattice Monte Carlo

With this model, we ran larger KLMC simulations with 2000 atoms (1000 on the Cu-sublattice and 1000 on the III-sublattice) at different temperatures. As we are currently just interested in the equilibrium configurations and not the full kinetic picture, we tuned the hop rates in the simulation to produce roughly equal numbers of hops on the Cu-sublattice as on the III-sublattice over the course of the simulation runs. First, we set all the migration barriers equal to 1 eV. Next, we varied the attempt frequencies of the III-sublattice hops from factors of 0.1 to 1.0 relative to the Cu-sublattice attempt frequencies. We ran several test runs and determined optimal scaling factors of 0.1 for 300K, 0.25 for 500K, and 0.5 for 700K for the III-sublattice attempt frequencies relative to the Cu-sublattice values. By tuning the rates in such a way, we can ensure that every part of the system reaches equilibrium in a minimal number of steps.

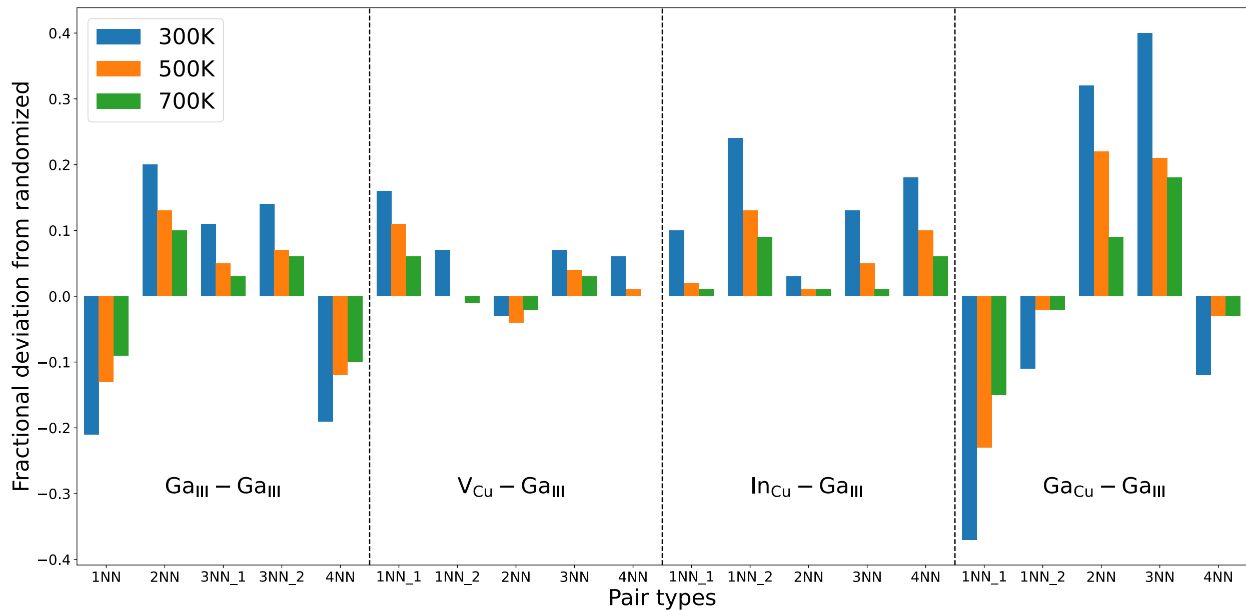

Figure 4.2: Average fractional deviation (at 300K, 500K, and 700K) of the occupation of different pair types from a randomized (no binding interactions) structure. Each triplet of bars corresponds to a different pair type.

To understand how the interaction model affects the distribution of different pair types, we

found the average occupation of the different pair types over a set of 40 randomly configured structures, and the average occupation of the different pair types over 100,000 step periods in 4 different KLMC runs using the interaction model at 300K, 500K, and 700K. Figure 4.2 depicts the results, plotting the fractional deviation of the occupation of different pairs with interactions included from the randomized baseline occupation. A positive value indicates that the concentration of that pair increased upon inclusion of the interactions, and a negative value indicates that it decreased. Figure 4.2 can be compared with Table 4.2 by noting that any pair with a positive (negative) interaction energy is expected to decrease (increase) in concentration compared to a randomized structure. In general, we observe this behavior occurring, with nearly all the positive deviations in Figure 4.2 corresponding to negative energies in Table 4.2 and vice versa. This confirms our model is behaving as expected. Figure 4.2 also provides insight on the magnitude of the deviations that our interaction model introduces into the system. The largest deviations show an increase or decrease of about 30% from the baseline, while most pairs have a deviation of around 10% or less. This shows that our model introduces a significant but not overwhelming change to the arrangement of atoms in the system. Figure 4.2 also demonstrates that as the temperature is raised, the deviations decrease and the system becomes more like the randomized one. This is expected, because at higher temperatures the entropy factor driving disorder becomes larger relative to the binding energies driving order.

We also developed an analysis to extract an order parameter from each step of the simulation that quantifies the degree of clustering in the system. We looked at both the clustering of vacancies on the Cu-sublattice and the clustering of Ga on the III-sublattice. For vacancies, the analysis loops over every Cu-sublattice site in a given configuration and records the number of vacancies around that site up to 3NN distance (including if the central site is itself a vacancy). For Ga, the

Table 4.3: Order parameters based on the standard deviation of local clustering, for randomized, 300K, 500K, and 700K systems. The order parameters are given for both V_{Cu} and Ga_{III} clustering.

Species	Randomized	300K	500K	700K
V_{Cu}	1.65	2.09	2.11	1.83
Ga_{III}	2.13	2.30	2.19	2.16

analysis loops over every III-sublattice site and records the Ga neighborhood in a similar manner. This produces a list of values corresponding to the local concentration of vacancies or Ga around each point. The standard deviation of this list is calculated, and following Refs. [65] and [66] the standard deviation is interpreted as a measure of the degree of clustering of the species of interest. In a completely randomized configuration, the standard deviation would be low, as all local neighborhoods would have the same number of vacancies or Ga atoms corresponding to the total concentration of these species. But in a highly inhomogeneous configuration, the standard deviation is expected to increase, as some sites will have a large number of vacancies or Ga atoms locally, while others will have few.

The order parameters calculated from our simulations are given in Table 4.3. As expected, ordering is the highest for 300K, and tends to decrease as the temperature is raised. It is noticeable that compared to a randomized system, the clustering of V_{Cu} increases significantly, while the clustering of Ga_{III} increases only slightly. Consequently, our model suggests that even at room temperature, CIGS will not have strongly Ga-rich and Ga-poor regions. This is reasonable in light of Table 4.2 and Figure 4.2, which show that while 2NN and 3NN bonds between Ga_{III}-Ga_{III} are attractive, 1NN and 4NN bonds are repulsive. Thus, any region around a Ga_{III} atom will include a similar fraction of sites that are favorable and unfavorable to other Ga_{III} atoms, preventing strongly Ga-rich regions. In contrast, our model predicts a much more pronounced increase in V_{Cu} clustering, despite the fact that individual V_{Cu} defects possess a -1 charge that repel them from

one another. This counterintuitive result could be due to the clustering of vacancies around group-III antisites (where their attraction to the +2 charged antisites is stronger than their repulsion from each other), as well as their interactions with the III-sublattice. As Figure 4.2 shows, V_{Cu}-Ga_{III} and In_{Cu}-Ga_{III} pairs are mostly favorable. This could contribute to a scenario where even moderately Ga-rich regions attract In_{Cu}-V_{Cu} clusters, boosting the inhomogeneity of V_{Cu} that already existed. The ability to capture such complicated and overlapping interactions is one of the unique powers of KLMC methods.

In a similar way, we developed an analysis to extract a local effective GGI ratio and local effective $[\mathrm{Cu}]/([\mathrm{In}]+[\mathrm{Ga}])$ (i.e. cation) ratio. As before, we looped over a set of all sites in the simulation and explored the local neighborhood around each site. Here, we used a larger cutoff of 20 Å (the largest spherical shell that can be inscribed in our 2000 atom simulation box). However, rather than averaging all atoms within this larger shell equally, we used a Gaussian distribution to weight the contributions from more distant sites less than those immediately around the central site. The radial distance of a site from the central site was input into the Gaussian function, and we varied the standard deviation radius of the Gaussian function from 10 Å to 20 Å. To find the GGI ratio, we looped over each III-sublattice site and counted each (weighted) Ga within the cutoff from the site, then divided by the total weighted number of group-III species within the cutoff. Likewise for the cation ratio, we looped over every site and divided the weighted sum of Cu within the cutoff radius by the weighted sum of In and Ga within the cutoff radius. We quantified the magnitude of the fluctuations in the local GGI or cation ratios by calculating the standard deviation of the set of local ratios at all sites in the simulation cell. Ref. [77] has derived equations predicting how the band gap, valence band maximum (VBM), and conduction band minimum (CBM) of CIGS vary

as functions of both the GGI ratio and the cation ratio, which they give as:

$$E_g^{\text{total}} = (1-x)E_g^{\text{CIS}} + xE_g^{\text{CGS}} - bx(1-x) + \alpha(25 - \text{X}_{\text{Cu}}) \tag{4.1}$$

$$\text{Offset}_{\text{CBM}}(\text{eV}) = \beta x(E_g^{\text{CGS}} - E_g^{\text{CIS}} - b(1-x)) + \sigma\alpha(25 - \text{X}_{\text{Cu}}) \tag{4.2}$$

$$\text{Offset}_{\text{VBM}}(\text{eV}) = (1-\beta)x(E_g^{\text{CIS}} - E_g^{\text{CGS}} - b(1-x)) + (1-\sigma)\alpha(25 - \text{X}_{\text{Cu}}). \tag{4.3}$$

Here x is the GGI, X_{Cu} is the % atomic fraction of Cu (equal to 25 in ideal CIS), $b = 0.23$ is the optical bowing constant, $\alpha = 0.017$ is the slope of Cu off-stoichiometry versus band gap, $\beta = 0.94$ is the relative change of the total band gap because of the shift in CBM due to Ga content, and $\sigma = -0.235$ is the relative change to the total band gap from the CBM due to Cu off-stoichiometry. These equations give a very similar dependence of the band gap on GGI as we find, and their prediction that the CBM is mainly affected by GGI content, while the VBM is mainly affected by Cu off-stoichiometry, is generally supported by other published work[78],[79]. We utilized these equations to predict the local band gap, VBM offset, and CBM offset using our local GGI and cation ratios. From these local values we found the fluctuations by taking the standard deviation over all sites in the cell.

Table 4.4 gives the fluctuations in the local GGI ratio and cation ratio as a function of the temperature and standard deviation radius. The GGI fluctuations decrease as temperature increases, a result of increased disorder at higher temperatures. This is the same trend previously observed in Figure 4.2, where increasing temperature drives the system towards a randomized structure. Thus, rapid quenching may reduce fluctuations in the GGI ratio, by freezing in higher temperature structures. However, the cation ratio does not have a clear temperature trend. This suggests that

Table 4.4: Fluctuations in the GGI ratio and cation ratio at 300K, 500K, and 700K. Values are reported for standard deviation radii of 10, 15, and 20 Å. The global GGI and cation ratios are 0.25 and 0.75, respectively. The fluctuations in the band gap, VBM, and CBM due to the GGI ratio, the cation ratio, and the combined effect of both are given, in meV. Last, the correlations between the local GGI ratio and local cation ratio are also given.

	10 Å			15 Å			20 Å		
	300K	**500K**	**700K**	**300K**	**500K**	**700K**	**300K**	**500K**	**700K**
GGI									
GGI	0.030	0.024	0.022	0.027	0.020	0.019	0.026	0.020	0.019
Band gap (meV)	16	13	12	14	11	10	14	10	10
CBM (meV)	15	12	11	13	10	9	13	10	9
VBM (meV)	1	1	1	1	1	1	1	1	1
Cation									
Cation	0.041	0.056	0.040	0.033	0.049	0.033	0.032	0.048	0.032
Band gap (meV)	15	20	15	12	18	12	12	18	12
CBM (meV)	4	5	3	3	4	3	3	5	3
VBM (meV)	18	25	18	15	22	15	14	22	14
Combined									
Band gap (meV)	27	25	19	23	22	16	22	21	16
CBM (meV)	13	12	11	12	11	10	12	10	10
VBM (meV)	18	25	18	15	22	15	14	22	14
Correlation	-0.492	-0.124	-0.004	-0.489	-0.106	-0.011	-0.477	-0.100	-0.022

rapid quenching may not help to reduce fluctuations in the cation ratio, as the fluctuations at 700K and 300K are identical, and even higher at 500K. We found that increasing the standard deviation radius consistently reduces the fluctuations. A longer radius gives increased weight to sites further from the central site, effectively smoothing out the local values and moving them closer to the global values, reducing the fluctuations as observed.

We calculated the correlations between the local GGI ratio and the local cation ratio, which are shown in Table 4.4. The correlations are consistently negative, indicating that an increase in local GGI ratio will lead to a decrease in local cation ratio, and vice versa. The correlations are quite strong at low temperature, but decrease upon heating, nearly disappearing at 700K. As previously discussed, this is caused by the increasing randomness of the system at higher temperatures. Increasing the standard deviation radius also tends to reduce the strength of the correlations, likely

for similar reasons as mentioned above: a longer radius reduces the fluctuations, so the correlations are less pronounced.

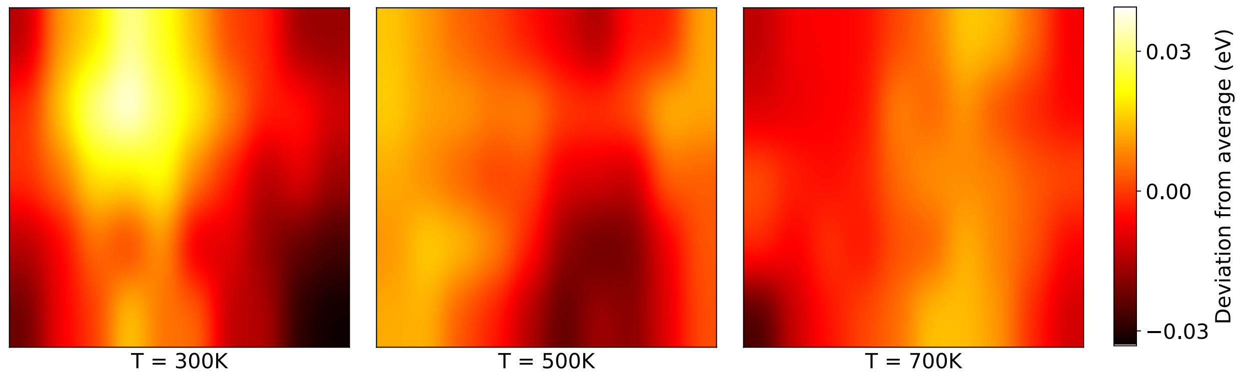

Figure 4.3: 4×4 nm cross-sectional *xy*-plane snapshots of the band gap fluctuations in CIGS at 300K, 500K, and 700K. The calculated local band gap values were interpolated with Gaussian smoothing to give the contours, which represent the local band gap deviation from its average value in the system.

Figure 4.3 depicts cross-sectional snapshots of the band gap fluctuations at 300K, 500K, and 700K. At 300K pronounced deviations are evident, but they largely dissipate by 700K. Table 4.4 reports the fluctuations in the band gap, VBM, and CBM due to variations in the local GGI and cation ratios, along with the fluctuations due to the combined effect of both. The combined band gap and CBM follow the same trends as the GGI ratio, decreasing at both higher temperature and higher standard deviation radius. However, the combined VBM follows the trends of the cation ratio, peaking at 500K, with equivalent fluctuations at 300K and 700K. It has been shown that the CBM changes significantly with GGI content, while the VBM remains nearly unaffected[77]. Thus, it is not surprising that the CBM fluctuations closely follow the GGI trends. Conversely, the VBM is strongly affected by changes in Cu content, while the CBM is affected only minimally[77]. Hence, the VBM fluctuations follow the trends in the cation ratio. This can be clearly seen by observing the individual impact of the GGI and cation ratio: from Table 4.4 it is clear that the VBM depends very little on GGI, while the CBM depends very little on the cation ratio.

Note that the combined fluctuations of the band gap at 300K are as large as $k_B T$ at 300K (26 meV), suggesting these fluctuations may have a noticeable impact on the device performance. An experimental study of CIGS films found band gap fluctuations that range from 15 to 65 meV[80] (measured as the standard deviation of the local band gap energy), which generally agree well with our predictions for the combined band gap fluctuations. The study concluded that alloy disorder and Cu content variation were key contributing factors to the fluctuations. In particular, they found that the fluctuations increased around 15 meV when comparing CIS to 0.25 GGI CIGS. This increase could reflect the contribution to the fluctuations arising from the introduction of alloy disorder, and it agrees very well with the band gap fluctuations we find arising from GGI variations.

Rapid quenching may reduce the fluctuations somewhat, as the hop rate of Ga is well below once per hour at 500K, so the III-sublattice fluctuations can likely be frozen in at their 500K values. However, the fluctuations in the band gap at 500K are nearly as large as those at 300K, owing to the impact of the high cation ratio (and thus the VBM) fluctuations at this temperature. To test the effects of quenching, we took structures that had previously been equilibrated to 500K, locked in the positions of the atoms on the III-sublattice, and then equilibrated only the Cu-sublattice at 300K. This reflects a more realistic scenario, in which the III-sublattice equilibrates down to 500K before freezing in, while the Cu-sublattice (with much faster diffusion) continues to equilibrate down to 300K. For a 10/15/20 Å standard deviation radius, we found fluctuations of 0.024/0.020/0.020 for the GGI ratio, 0.066/0.057/0.055 for the cation ratio, and 29/25/24 meV for the band gap. The GGI ratio values are unchanged from the 500K values in Table 4.4, reflecting the fact that In_{Cu}/Ga_{Cu} antisites do not have much impact on the local GGI ratio, so changes in only the Cu-sublattice have little impact. The cation ratio values are higher than both the respective 300K values and 500K values in Table 4.4. This suggests that the III-sublattice at 500K, as opposed to at 300K,

may actually contribute to the highest fluctuations in the cation ratio, whereas for the Cu-sublattice the highest fluctuations are at 300K. The band gap fluctuations, driven by the higher cation ratio fluctuations, are even greater after quenching than at either 300K or 500K alone. These results suggest that a rapid quench may not do much to reduce fluctuations in CIGS.

Chapter 5

Cu(In,Ga)Se_2: Cu_{In} Passivation

5.1 Introduction

In semiconductor operation, deep level traps are defects that lie deep within the band gap, with energy levels far from the band edges. They are undesirable, as they degrade device performance by capturing free electrons or holes, thus compensating the desired doping, and reducing the non-radiative lifetime of charge carriers[8]. Cu_{In} antisite defects are prominent deep level defects in CIS solar cell devices. However, they can be passivated by forming a complex with In_{Cu} antisites[8]. Careful control of the growth and annealing conditions can influence the formation of these complexes and reduce deep level traps[8]. By simulating the process whereby an In_{Cu} diffuses towards a Cu_{In} and forms a passivated complex, we can develop a model to predict the time for this capture to happen as a function of initial separation distance, temperature, and composition. Such a model can be incorporated into a continuum simulation and used to optimize the annealing process by reducing expected deep level formation.

5.2 Model Calibration

The current work builds on our previous models of In_{Cu} diffusion in CIS. Previous work by us also demonstrated that the binding interaction between In_{Cu} and Cu_{In} can be modeled as the interaction between +2 and -1 point charges, respectively[8]. To model the formation of passivated In_{Cu}-Cu_{In} complexes, we started with our previous KLMC model for In and vacancy diffusion that only contains the Cu-sublattice. To represent Cu_{In}, a single immobile defect was added to the location of a theoretical In site in the KLMC simulation, without adding the complete III-sublattice. Interactions were incorporated such that the Cu_{In} defect behaved as a -1 point charge. Additionally, the Cu-sublattice was populated with a number of In_{Cu} and V_{Cu} defects appropriate for the composition desired, using the method outlined previously in Chapter 3.1.

Initially, the simulation was run at 750K for 100,000 steps, with a composition of k_{Cu}/k_{In} = 0.95, for 400 runs starting from random initial configurations. As each run only contains one Cu_{In} defect, we defined a passivated state as one where one or more In_{Cu} defects are at 1NN distance (technically 2NN as there is a Se site between Cu and In sites, but 1NN when only considering the cation sublattices) from the immobile Cu_{In} defect. If for a given time step the simulation was in a passivated state, we assigned it 1, and if it was not passivated we assigned it 0. At each simulation time step, we averaged these values for all 400 runs, with the resulting value being the average fraction of Cu_{In} passivated over time. This value initially began low, based on a random distribution of In_{Cu}, but over time equilibrated to a stable value of around 0.75, suggesting the large majority of complexes are passivated even at high temperature.

Next, we identified a set of 400 equilibrium configurations that combined have an average fraction of Cu_{In} passivated that is equal to the equilibrium value at 750K. These configurations were used to initialize 400 runs at 300K. As with the higher temperature runs, we found the average

fraction of Cu_{In} that is passivated at each time step over the course of the simulations. At the start of the simulations, the average fraction passivated equals the 750K equilibrium value, but gradually increases as In_{Cu} diffuses and is captured by Cu_{In}. Our goal is to simulate a rapid quench from high to low temperature, and the rate by which the average fraction passivated increases can be used to develop a model for the rate of passivation of Cu_{In} by In_{Cu}. The large number of different runs allows us to sample a large number of different capture events, to obtain a smooth function of the average fraction passivated over time.

We had previously observed that when the cutoff radius for the coulombic interactions between charged defects was too large, so that the spherical shell of interaction surrounding a defect could not be contained entirely within the simulation cell, the self-interactions that Cu_{In} had with its periodic images created undesirable effects. Essentially, any movement of a mobile species such as In_{Cu} towards the frozen Cu_{In} was also movement away from the image of Cu_{In} in the neighboring cell, and the overlapping potentials effectively reduced the net interaction strength between In_{Cu} and Cu_{In}, leading to a slower rate of passivation. On the other hand, when the cutoff radius was too small, so that the interaction sphere around a defect was significantly smaller than the simulation cell, this also created undesirable problems. In this case, with a large fraction of sites in the cell outside the interaction radius of the Cu_{In} defect, the rate of passivation was incorrectly predicted to be slower, as In_{Cu} atoms outside the cutoff radius did not experience any attraction towards Cu_{In}.

To avoid these problems, we determined that the optimal configuration is to have a nearly-cubic cell with the cutoff chosen so that the spherical interaction shell can be nearly inscribed in the cell, but not extending beyond. This allows the interactions to cover the largest fraction of the cell possible while avoiding self-overlap. Because the *c*-axis of the 8-atom unit cell is longer than the *a*- and *b*-axes, this requires the *c* direction to have fewer repetitions to be nearly-cubic. We tested

convergence by running the full set of calculations at three different cell sizes: $4 \times 4 \times 3$, $5 \times 5 \times 4$, and $7 \times 7 \times 5$ multiples of the 8-atom unit cell in the $a \times b \times c$ directions, with interaction cutoffs of 16 Å, 20 Å, and 28 Å, respectively. We used the average fraction passivated to calculate the concentration of unpassivated Cu_{In} at each step in the simulations, and plotted the concentration as a function of simulation time. These results are plotted in Figure 5.1 for the three different cell

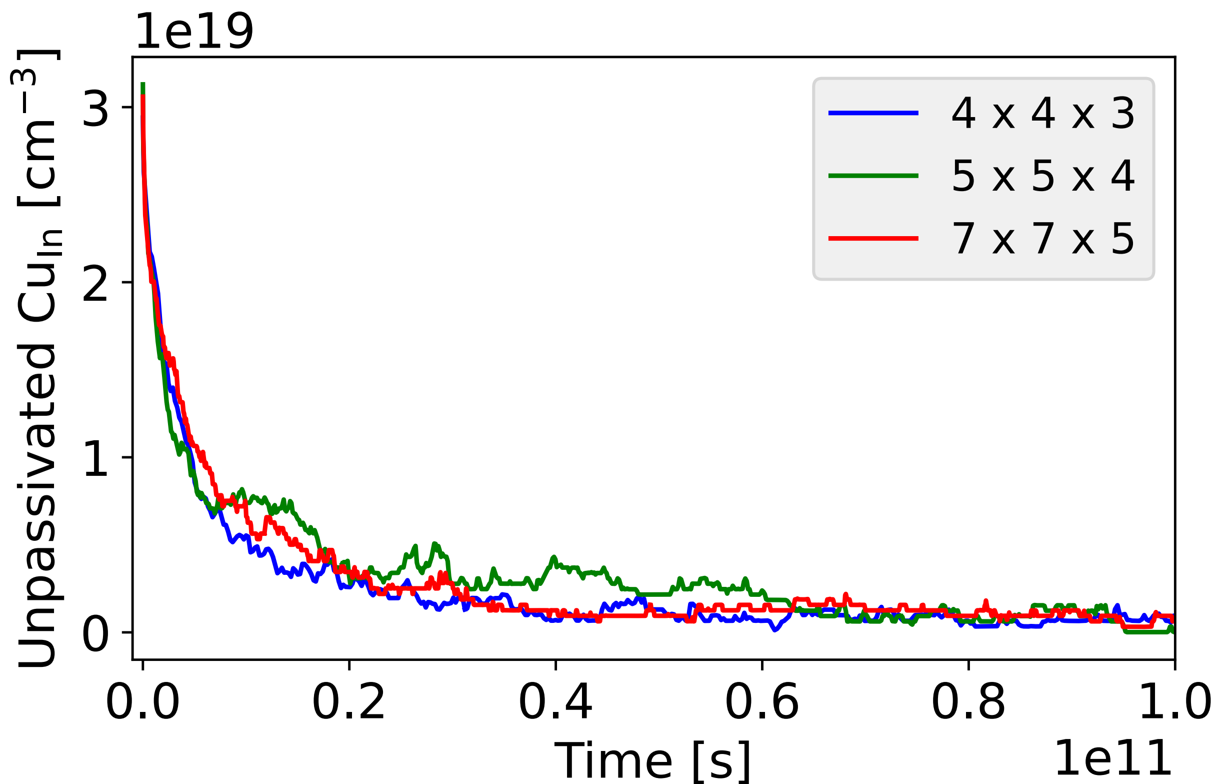

Figure 5.1: Concentration of unpassivated Cu_{In} over time for different simulation cell sizes: $4 \times 4 \times 3$, $5 \times 5 \times 4$, and $7 \times 7 \times 5$ multiples of the 8-atom unit cell.

sizes. As can be seen, the results are clearly converged with respect to cell size, and show a smooth decay of the concentration of unpassivated Cu_{In}. The diffusivities are also quite well-converged: 6.9×10^{-25} $\frac{cm^2}{s}$ in $4 \times 4 \times 3$, 9.6×10^{-25} $\frac{cm^2}{s}$ in $5 \times 5 \times 4$, and 1.2×10^{-24} $\frac{cm^2}{s}$ in $7 \times 7 \times 5$. Over time, In_{Cu} migrates to the unpassivated Cu_{In} and forms complexes, improving the charge carrier lifetime of the device by eliminating these unpassivated Cu_{In} deep level traps.

5.3 Capture Cross Section Estimation

From these results, we attempted to estimate a capture cross section for $\mathrm{Cu_{In}}$ by fitting the data to a rate equation. The process of $\mathrm{Cu_{In}}$ passivation can be modeled at the continuum level as a diffusion-limited reaction among charged species. Essentially, we can treat unpaired $\mathrm{In_{Cu}}$ and unpaired $\mathrm{Cu_{In}}$ as separate reactants A and B that react to form C, which is the passivated defect complex. This reaction is considered to happen instantaneously when the two reactants are within a 1NN radius of each other, so the rate is controlled only by the diffusion of the reactants towards each other. Because we treat $\mathrm{Cu_{In}}$ as being immobile, we only need to consider the diffusivity of $\mathrm{In_{Cu}}$. The reaction can be expressed as:

$$[\mathrm{In_{Cu}}] + [\mathrm{Cu_{In}}] \rightleftharpoons [\mathrm{In_{Cu}} + \mathrm{Cu_{In}}] \quad (5.1)$$

where $[\mathrm{In_{Cu}}]$ and $[\mathrm{Cu_{In}}]$ are the concentrations of unpassivated (i.e. neither has the other at a 1NN location) $\mathrm{In_{Cu}}$ and $\mathrm{Cu_{In}}$ respectively, and $[\mathrm{In_{Cu}} + \mathrm{Cu_{In}}]$ is the concentration of passivated $\mathrm{In_{Cu}}$+$\mathrm{Cu_{In}}$ complexes.

We are interested in modeling the rate of depletion of unpassivated $\mathrm{Cu_{In}}$, which is then given by:

$$-\frac{d[\mathrm{Cu_{In}}]}{dt} = k_1[\mathrm{In_{Cu}}][\mathrm{Cu_{In}}] - k_{-1}[\mathrm{In_{Cu}} + \mathrm{Cu_{In}}] \quad (5.2)$$

where k_1 is the forward rate constant and k_{-1} is the backwards rate constant. As can be seen from Figure 5.1, nearly all unpassivated $\mathrm{Cu_{In}}$ defects react to become passivated complexes over time, and we can thus assume that the backwards rate constant k_{-1} is very small and ignore the $k_{-1}[\mathrm{In_{Cu}} + \mathrm{Cu_{In}}]$ term. Likewise, $[\mathrm{In_{Cu}}]$ is much larger than $[\mathrm{Cu_{In}}]$ and can be treated as a constant,

as In_{Cu} does not get used up. The general solution to the rate equation takes the form:

$$[Cu_{In}] = Ae^{-k_1[In_{Cu}]t} \tag{5.3}$$

To improve the accuracy, the small but non-zero equilibrium value of $[Cu_{In}]$ can be added to the equation giving:

$$[Cu_{In}] = Ae^{-k_1[In_{Cu}]t} + [Cu_{In}]_{eq} \tag{5.4}$$

where $[Cu_{In}]_{eq}$ is the equilibrium concentration of Cu_{In}.

It has been derived previously[81] that the rate constant for the diffusion-controlled reaction $A + B \rightleftharpoons C$, with a coulombic interaction between A and B, has the form:

$$k_1 = 2\pi Da \tag{5.5}$$

where D is the diffusivity of one species with respect to the other (in our case when Cu_{In} is immobile, it is simply the diffusivity of In_{Cu}), and a is the capture radius, with units of length. Thus we can fit Equation 5.4 to our data by finding A and a. This is valid for when a single mechanism with rate k_1 controls the reaction at all times, with D constant. However, because our simulations at 300K are initialized with configurations run at 750K, the arrangement of defects (such as the concentration of In_{Cu}-V_{Cu} complexes) will not be at equilibrium initially. This will impact the diffusivity of In_{Cu} and other factors such as the screening of Cu_{In} by other charged vacancies. Over time, these will change and the rate may also change as a result. Thus we suspect that a double exponential function, which allows for two different mechanisms with distinct rates, will better

Table 5.1: Parameters determined from fitting to single and double exponential functions. A and a correspond respectively to the pre-exponential factor ($\frac{cm^3}{s}$) and capture radius (Å) for the single exponential function, while A_1 and a_1 correspond to the faster mechanism of the double exponential function, and A_2 and a_2 correspond to the slower mechanism of the double exponential function.

	A	a	A_1	a_1	A_2	a_2
$4\times4\times3$	2.3×10^{19}	30	2.0×10^{19}	64	0.7×10^{19}	10
$5\times5\times4$	1.6×10^{19}	10	1.9×10^{19}	86	0.9×10^{19}	5
$7\times7\times5$	2.1×10^{19}	13	1.2×10^{19}	49	1.3×10^{19}	8

capture the simulation dynamics. Such a function has the form:

$$[\mathrm{Cu_{In}}] = \mathrm{A}_1 e^{-k_1[\mathrm{In_{Cu}}]t} + \mathrm{A}_2 e^{-k_2[\mathrm{In_{Cu}}]t} + [\mathrm{Cu_{In}}]_{eq} \tag{5.6}$$

where k_1 and k_2 are the rate constants associated with a slower and a faster mechanism, and A_1 and A_2 represent the relative weights of the two different mechanisms to the overall passivation process.

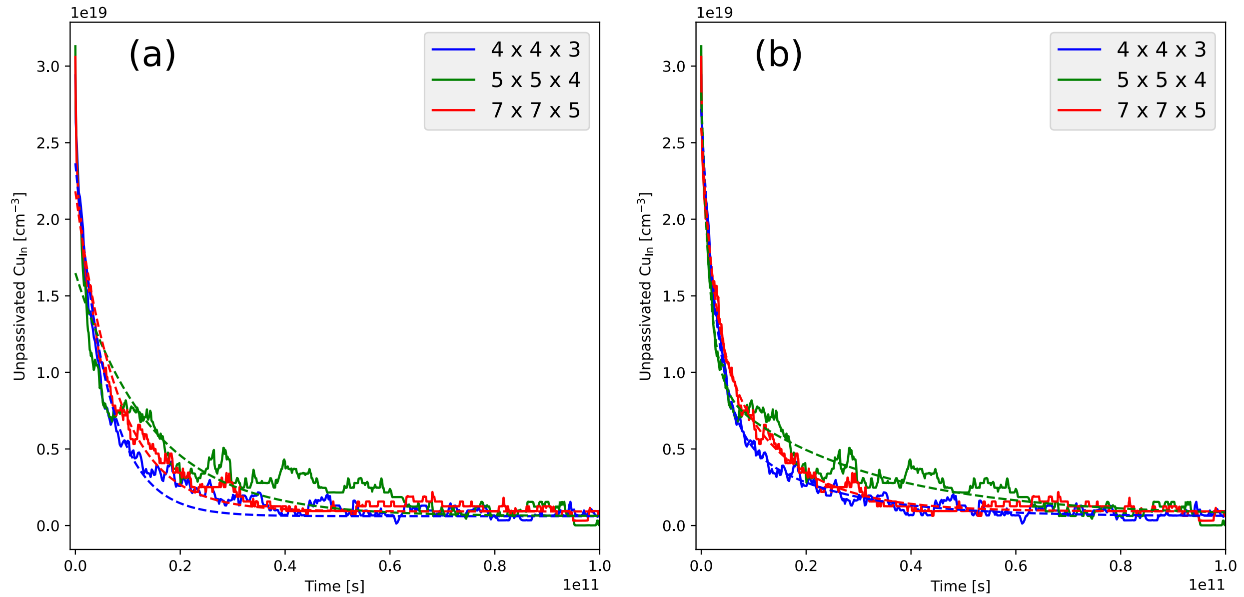

Figure 5.2: Results from fitting the passivation of Cu_{In} to (a) single and (b) double exponential functions, for each of the three different simulation cell sizes.

We fit our results for the three different simulation cell sizes to both single exponential and dou-

ble exponential functions, as shown in Figure 5.2, with parameters given in Table 5.1. As expected, the double exponential functions fit better than the single exponential functions. However, even the single exponential functions fit the data fairly well. This suggests a single rate constant generally captures the behavior, and the different passivation mechanisms may be similar to each other in magnitude. Mainly, the single exponential fits fail to fully characterize the initial rapid drop in unpassivated Cu_{In}. We suspect that this initial fast mechanism arises from the non-equilibrium nature of the starting configurations. At 750K, most In_{Cu} defects have no or only one V_{Cu} neighbor. At 300K, nearly all of the In_{Cu} defects have two or more V_{Cu} neighbors. Given that Cu_{In} is immobile, passivation can only occur when a mobile In_{Cu}-V_{Cu} complex migrates towards a Cu_{In} defect. An In_{Cu} in a complex with only one V_{Cu} will have a net charge of +1, and so will be attracted towards the -1 charged Cu_{In}. But when all In_{Cu} defects are in a complex with two or more V_{Cu} defects, the complex as a whole will be neutral or negatively charged, and so will not be attracted to unpassivated Cu_{In}. We propose that closer to $t = 0$, most mobile In_{Cu} is in positively charged complexes and so moves rapidly towards unpassivated Cu_{In} sites. Over time, however, more V_{Cu} defects attach themselves to In_{Cu}, and effectively screen the interaction between In_{Cu} and Cu_{In}, reducing the rate of passivation. This would explain the initial fast mechanism that causes a rapid drop in the concentration of unpassivated Cu_{In}, followed by the slower mechanism at later times.

To test this, we developed an analysis class that tracks the number of V_{Cu} at 1NN to each In_{Cu} at 1000 step intervals. When a simulation run is initially in an unpassivated state, the analysis identifies the first In_{Cu} to passivate the Cu_{In}. It then calculates the average number of V_{Cu} neighbors that the In_{Cu} that eventually passivates the Cu_{In} had from $t = 0$ until the time that the passivation event occurred. Essentially, this is calculating what the average “vacancy neighborhood” around the In_{Cu} looked like over the path it took to reach the Cu_{In}. For each simulation run that is initially

unpassivated (about 100 runs for each cell size considered), there is a unique time that the run became passivated, and an associated average vacancy neighborhood for the path the In_{Cu} took to reach the Cu_{In}.

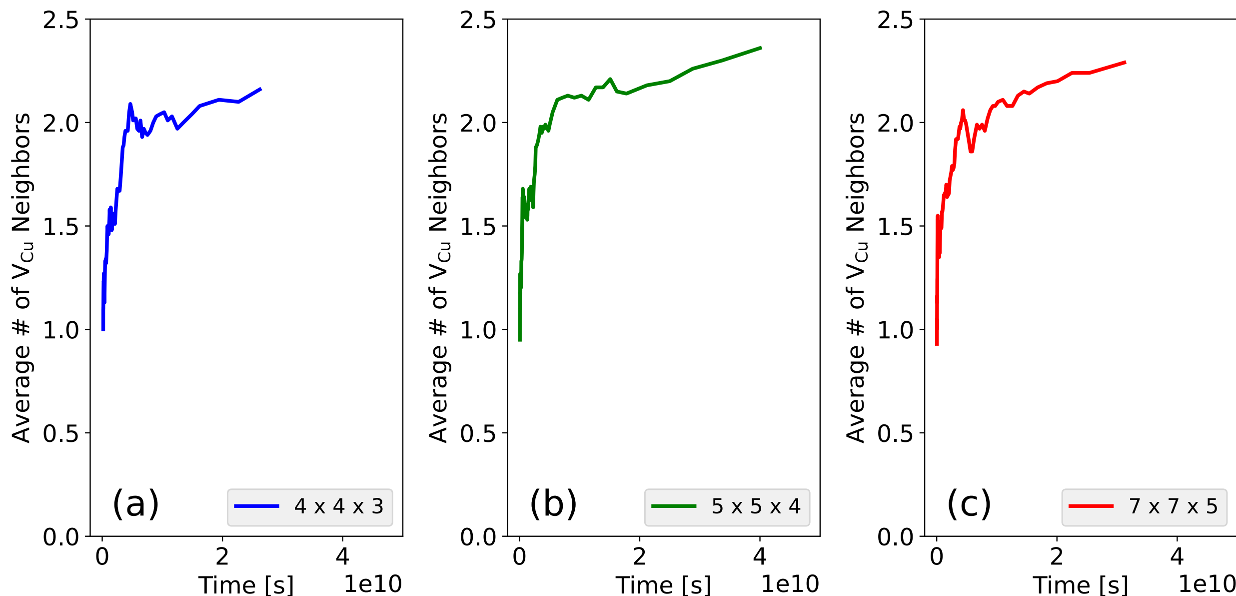

Figure 5.3: Average number of V_{Cu} neighbors to an In_{Cu} from $t = 0$ until the time that the In_{Cu} forms a passivated complex with Cu_{In}. The data points are ordered by the time that the passivation occurs in the simulation. The three different simulation cell sizes are shown: (a) $4 \times 4 \times 3$, (b) $5 \times 5 \times 4$, and (c) $7 \times 7 \times 5$.

We plotted these results in Figure 5.3. Simulation runs that became passivated very quickly correspond to data points at earlier times on the x-axis, while simulation runs that took very long to become passivated correspond to data points at later times. As can be seen in Figure 5.3, In_{Cu} defects that passivated the Cu_{In} early on had fewer V_{Cu} neighbors during their journey to the Cu_{In} than those that passivated it later on. The average number of V_{Cu} neighbors when passivation occurs near $t = 0$ is around 1, but as time passes, more V_{Cu} attach themselves to In_{Cu}, so that the average number of neighbors increases to over 2 at later times. This confirms our theory by demonstrating that early on in the simulations, most In_{Cu} is found in single-vacancy +1 charged complexes, which are rapidly drawn towards unpassivated -1 charged Cu_{In}. But over time, V_{Cu}

(with -1 charge) surrounds In_{Cu} and screens their interactions with Cu_{In}, slowing down the rate of passivation. Therefore, we can see two distinct mechanisms as existing: the fast mechanism applying to single-vacancy In_{Cu} complexes (which are attracted to unpassivated Cu_{In}), and the slow mechanism applying to multiple-vacancy In_{Cu} complexes, which do not feel any attraction to unpassivated Cu_{In}. Initially the fast mechanism is dominant, but over time the slow mechanism takes over.

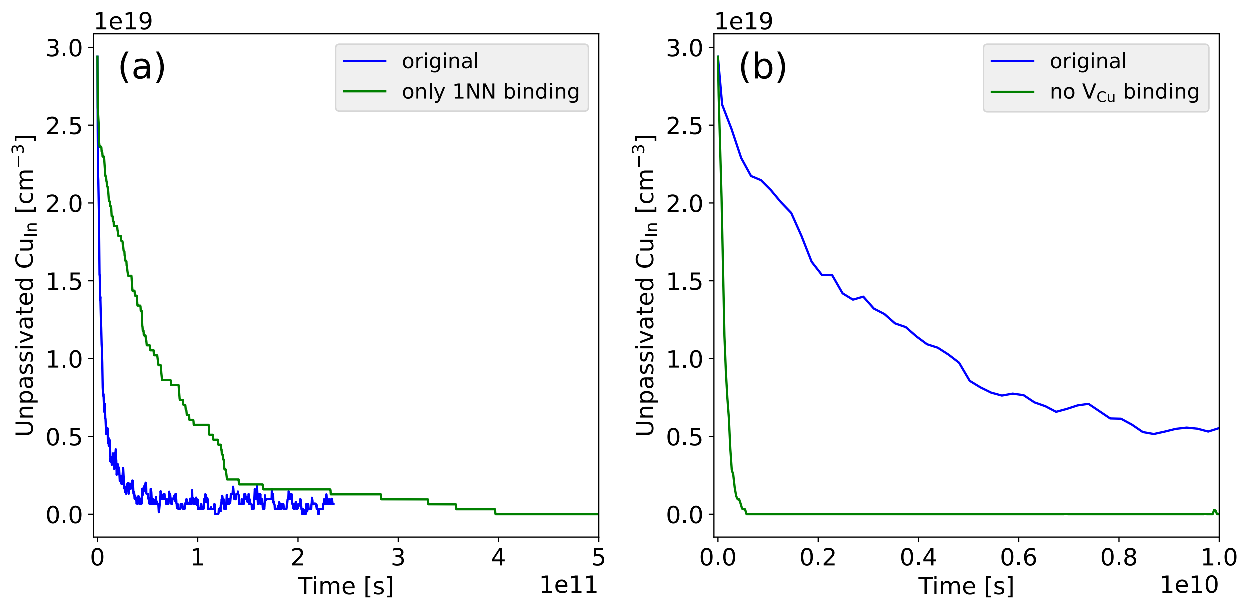

Figure 5.4: Modifications to the interaction model in the $4 \times 4 \times 3$ cell size. (a) compares the original (unmodified) model to the model including only 1NN interactions for Cu_{In}. (b) compares the original model to the model without V_{Cu} interactions. Note the difference in *x*-axis scale.

To further explore the impact of the binding interactions on the rate of passivation, we tested two artificial modifications of the model in the $4 \times 4 \times 3$ cell. In one, we limited the interaction range of the Cu_{In} defect to only 1NN distances. In the other, we made all V_{Cu} defects neutral, leaving In_{Cu} as +2 and Cu_{In} as -1. The results are shown in Figure 5.4. As expected, by limiting the Cu_{In} interactions to only 1NN (Figure 5.4a), the rate of passivation is much slower than with long-range interactions. This is because In_{Cu} defects are not attracted to Cu_{In} and so only passivate

Cu_{In} when they happen to reach a 1NN site after a long period of random diffusion. However, without long-range interactions, there are no reversals of passivation and the curve trends steadily downward until every run is passivated. This occurs because with long-range interactions, a hop from 1NN to 2NN is only a small energy penalty, as 2NN has nearly as strong of binding as 1NN does. But with only 1NN interactions, a hop from 1NN to 2NN requires overcoming the full 1NN interaction, which is very difficult at 300K. Thus, while passivation is slower overall, once passivation occurs it becomes locked in. In contrast, eliminating V_{Cu} interactions causes passivation to become extremely rapid (note Figure 5.4b and the difference in *x*-axis scale). One factor is simply that the diffusivity of In_{Cu} becomes much higher: it is 3.8×10^{-23} $\frac{cm^2}{s}$ in Figure 5.4b compared to 8.7×10^{-25} $\frac{cm^2}{s}$ in Figure 5.4a and 6.9×10^{-25} $\frac{cm^2}{s}$ in the original run. The higher diffusivity allows In_{Cu} defects to reach Cu_{In} much more quickly. The diffusivity likely increases because without interactions, the V_{Cu} defects can move around freely and do not get locked into low-energy configurations. Additionally, without the -1 V_{Cu} interactions, the only attractive interactions are between In_{Cu} and Cu_{In}. This means that Cu_{In} becomes the prime target for all In_{Cu} in the simulation, and there is no V_{Cu} screening to slow them down.

5.4 Comparison to Experiment

Unpublished experimental work, courtesy of X. Xiang (2022) in the S. Dunham research group at the University of Washington, demonstrated that heating CIS samples to 383K for 2 hours caused a drop in the open-circuit voltage (Voc), reflecting a degradation in the cell performance. After cooling and remaining at 300K several weeks, however, the Voc had recovered to pre-annealing levels. Initially, it was supposed that if Cu_{In} antisites are the performance-limiting trap centers,

the drop in Voc would have likely been caused by the annealing breaking apart passivated In_{Cu}-Cu_{In} complexes and activating the detrimental Cu_{In} trap states. However, as our model predicts that passivation of Cu_{In} after cooling from a high temperature to 300K will take centuries to reach equilibrium (in Figure 5.1, 10^{11} seconds is approximately 3000 years), it seems unlikely that any meaningful recovery of the Voc would occur in just a few weeks if the Voc is limited by Cu_{In}. Thus, our results motivate searching for alternative possible mechanisms besides the passivation of Cu_{In} by In_{Cu} to explain the rapid recovery in Voc observed experimentally.

Chapter 6

Cd(Se,Te): Diffusion of Intrinsic Defects

6.1 Introduction

In addition to our work on CIGS, we present results for diffusion of intrinsic defects in CdSeTe using a very similar approach. Unlike with CIGS, in CdSeTe there is less certainty as to which defects dominate diffusion and the nature of their ground state configurations. Antisites primarily diffuse in complexes with vacancies, but the expected concentrations of the necessary complexes in CdSeTe are too low to contribute significantly to diffusion. Therefore, we exclude antisite diffusion and consider only diffusion via vacancies and interstitials. Furthermore, we consider only the dominant charge states of the defects, as we find that the concentrations of the defects in their non-dominant charge states are too low to ever be significant for diffusion.

A review of the experimental literature on CdTe diffusion will be helpful here. Figure 6.1 depicts several radiotracer diffusion experiments on Cd self-diffusion in CdTe over a range of temperatures[10],[12],[82]–[87]. As is apparent, there is a strong consensus on the value of D_{Cd}, especially in the high-temperature regime. Figure 6.1 also demonstrates the existence of high-

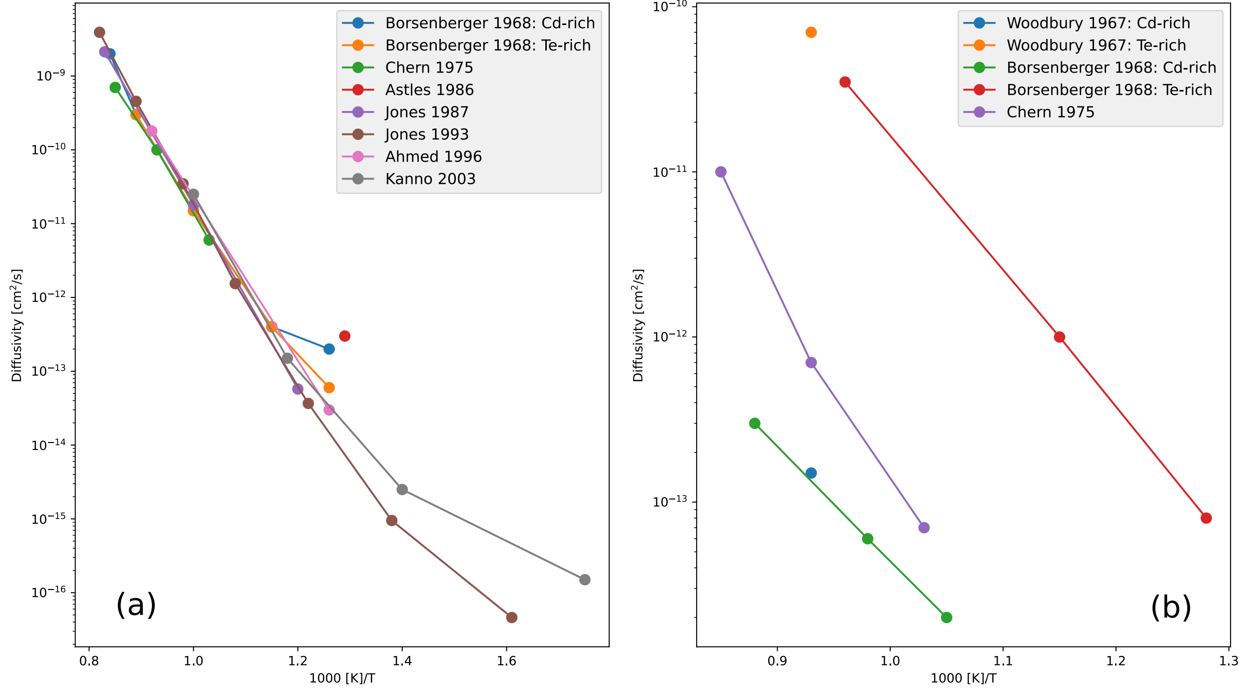

Figure 6.1: Arrhenius plots of experimental tracer diffusivity of (a) Cd and (b) Te in CdTe. Results by Woodbury 1967 [82], Borsenberger 1968 [12], Chern 1975 [83], Astles 1986 [84], Jones 1987 [10], Jones 1993 [85], Ahmed 1996 [86], and Kanno 2003 [87].

temperature and low-temperature mechanisms with distinct activation energies, although there is some disagreement on the temperature at which the low-temperature mechanism becomes dominant[12],[83],[85],[87]. Additionally, there is a consensus that D_{Cd} has very minimal or nonexistent dependence on the partial pressure p_{Cd}[12],[83],[85],[88]. In order to explain the absence of significant partial pressure dependence of D_{Cd}, different mechanisms are proposed: it is believed that D_{Cd} arises either from a superposition of contributions from different defects with opposite p_{Cd} dependencies (such as vacancies and interstitials)[12],[83], or it arises from a pressure independent mechanism such as a $(\mathrm{Cd_i V_{Cd}})^x$ ring mechanism[83],[88].

Figure 6.1 shows less of a clear-cut consensus with regards to D_{Te} self-diffusivity. Refs. [12], [82] agree with each other but are quite different from Ref. [83]. Unlike with D_{Cd}, D_{Te} displays a strong dependence on p_{Cd}. Refs. [12], [82], [83] report a p_{Cd}^{-1} dependence of D_{Te}, while Refs.

[83], [88] also report a $p_{\mathrm{Cd}}^{1/3}$ dependence at high p_{Cd}'s. Refs. [12], [82] both suggest that D_{Te} is mediated by neutral $\mathrm{Te_i}$. Ref. [82] observes that D_{Te} is independent of doping, indicative of neutral defects. Additionally, they note that the simple reciprocal p_{Cd} dependence suggests a simple $\mathrm{Te_i}$ mechanism over more complex models. Refs. [83], [88] agree with a $\mathrm{Te_i}^x$ mechanism at low p_{Cd}, but also observe evidence of a transition to a high p_{Cd} mechanism, which they assume to be V_{Te}^{+2}, possessing the observed $p_{\mathrm{Cd}}^{1/3}$ dependence.

6.2 Ab Initio Calculations

To elucidate the nature of the intrinsic defects in CdSeTe, we used molecular dynamics (MD) to run simulated annealing, a technique for finding global energy minimums without an initial guess structure. Essentially, the system begins at high temperature and is slowly cooled, eventually settling into a low energy configuration. MD was run in the canonical (NVT) ensemble, using the Nose-Hoover thermostat to control the system temperature. The system was advanced with a 6 femtosecond time step for 1000 steps, starting at 1000K and ending at 1K. Four runs were performed for each defect, and the lowest energy structures resulting from these runs are shown in Figure 6.2. In $\mathrm{V}_{\mathrm{Cd}}^{-2}$, the neighboring Te atoms are contracted inwards about 0.2 Å, while in $\mathrm{V}_{\mathrm{Te}}^{+2}$ the neighboring Cd atoms are distorted outwards about 0.7 Å. When a Se atom is added nearby, the neighboring Cd is distorted even further from the vacancy and towards the Se. In $\mathrm{V}_{\mathrm{Te}}^{+2}$, with the removal of the fourth Te bond, the neighboring Cd atoms shift from tetrahedral coordination to more stable trigonal planar coordination with Te-Cd-Te angles of 119 degrees. However, in $\mathrm{V}_{\mathrm{Cd}}^{-2}$, the neighboring Te atoms are not quite trigonal planar, with Cd-Te-Cd angles of only 104 degrees. In $\mathrm{Cd}_{\mathrm{i}}^{+2}$, we found that the interstitial is stable in both the tetrahedral anion ($\mathrm{T_a}$) site surrounded

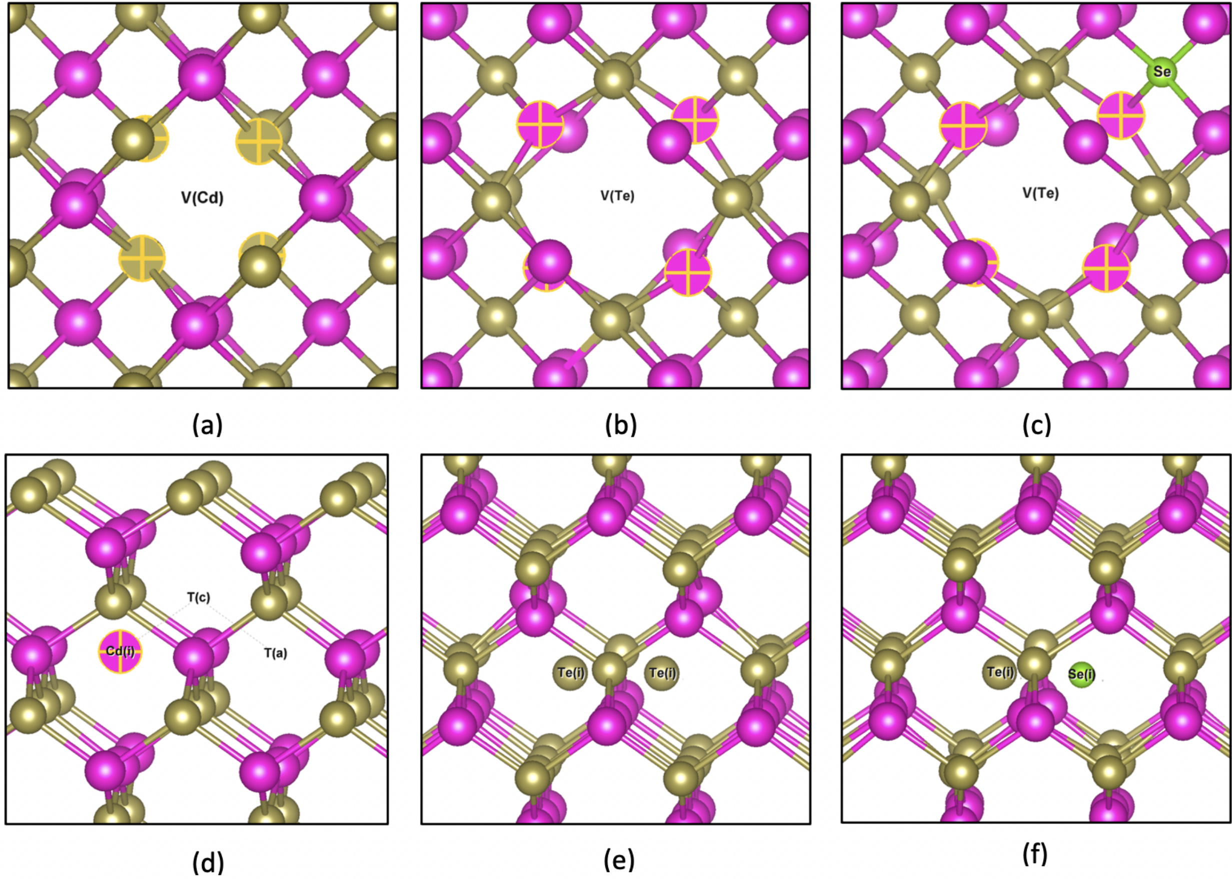

Figure 6.2: Relaxed ground state structures of intrinsic defects in CdTe. (a) V_{Cd} with nearest-neighbor Te atoms highlighted. (b) V_{Te} with nearest-neighbor Cd atoms highlighted. (c) V_{Te} with nearest-neighbor Cd atoms highlighted and a neighboring Se_{Te} defect. (d) Cd_i with T(c) and T(a) sites indicated, connected by a possible diffusion path. (e) Te_i-Te_i split interstitial. (f) Se_i-Te_i split interstitial. Purple corresponds to Cd atoms, dark green corresponds to Te atoms, and light green corresponds to Se atoms (only shown in (c) and (f)).

by Te atoms and the tetrahedral cation (T_c) site surrounded by Cd atoms. However, for this charge state the T_a site is lower in energy by about 0.38 eV. The dashed line in Figure 6.2 illustrates the path the interstitial takes through the intermediate T_c site to move between more stable T_a sites. In contrast to Cd_i^{+2}, both Te_i^{+0} and Se_i^{+0} prefer to form split interstitials oriented along the [110] directions. Ref. [13] find identical stable configurations for both the Cd_i^{+2} and Te_i^{+0} interstitials.

Next, we used NEB in VASP to find the migration barriers for the defects in CdTe. Attempts to calculate barriers for defects in CdSe have not yet succeeded, so we exclude them for now. The methodology followed that as outlined for CIGS in Chapter 2.2. Table 6.1 contains the migration

Table 6.1: Migration barriers for vacancy and interstitial defects in CdTe.

Vacancies	$\mathbf{V_{Cd}^{-2}}$	$\mathbf{V_{Te}^{+2}}$	$\mathbf{(Se_{Te} + V_{Te})^{+2}}$
	0.93	1.20	1.15
Interstitials	$\mathbf{Cd_i^{+2}}$	$\mathbf{Te_i^{+0}}$	$\mathbf{Se_i^{+0}}$
	0.52	0.16	0.28

barriers found for defects in CdTe. Our value of 0.93 eV for V_{Cd}^{-2} diffusion is somewhat lower than Ref. [89]'s value of 1.19 eV. However, our value of 1.2 eV for V_{Te}^{+2} is quite close to Ref. [15]'s value of 1.13 eV. Although we did not find this value reported in literature, we find that an $(Se_{Te} + V_{Te})^{+2}$ exchange in CdTe is 1.15 eV, which is quite similar to the V_{Te}^{+2} exchange. For Cd_i^{+2} diffusion, we find the same diffusion path as in Ref. [13]: the interstitial is stable in the T_a site, moves to the T_c site, and then quickly moves either back to the original T_a site or to a new T_a site. We find a barrier of 0.52 eV when hopping from T_a to T_c, and a barrier of 0.13 eV when hopping from T_c to T_a. This agrees well with Ref. [13]'s values of 0.42 eV and 0.08 eV and Ref. [11]'s values of 0.47 eV and 0.1 eV for the forward and reverse barriers, respectively. We found the Te_i^{+0} and Se_i^{+0} split interstitials can diffuse rapidly along the [110] directions, with barriers of 0.16 eV and 0.28 eV respectively. Refs. [13] and [11] confirm this, finding 0.1 eV and 0.09 eV respectively for the Te_i^{+0} interstitial.

6.3 Kinetic Lattice Monte Carlo

Last, we developed both KLMC and analytic models to describe the diffusion of isolated defects in CdSeTe, following a similar approach as used for CIGS. Our simulations incorporated both the Cd and Te/Se sublattices in cells containing 1000 lattice sites. Unlike in CIGS, the typical concentrations of the relevant defects are very dilute and unlikely to interact significantly with other

Table 6.2: Parameters used in analytic diffusion models.

	z	d	f	λ(cm)	ν(THz)	ΔE
Vacancies						
$\mathbf{V_{Cd}^{-2}}$	12	3	0.7815	4.69×10^{-8}	10	0.93
$\mathbf{V_{Te}^{+2}}$	12	3	0.7815	4.69×10^{-8}	10	1.2
$(\mathbf{Se_{Te}} + \mathbf{V_{Te}})^{+2}$	12	3	0.7815	4.69×10^{-8}	10	1.15
Interstitials						
$\mathbf{Cd_i^{+2}}$	4	3	0.75	4.69×10^{-8}	10	0.52
$\mathbf{Te_i^{+0}}$	2	3	1	4.69×10^{-8}	10	0.16
$\mathbf{Se_i^{+0}}$	2	3	1	4.69×10^{-8}	10	0.28

defects. Therefore, we simulate each defect type separately in a cell containing only one instance of the defect of interest. For V_{Cd}^{-2}, we included $V_{Cd} - Cd_{Cd}$ hops with $V_{Cd} - Se_{Te}$ interactions as previously calculated by our group up to 2NN distance. For V_{Te}^{+2}, we included both $V_{Te} - Te_{Te}$ and $V_{Te} - Se_{Te}$ hops with $Se_{Te} - Se_{Te}$ interactions up to 1NN. To model Cd_i^{+2}, we added additional lattice sites corresponding to the T_a and T_c sites. Allowed hops included both T_a-T_c and T_c-T_a hops, with no interactions added. Modeling of the Te_i^{+0}/Se_i^{+0} split interstitials was significantly more complicated. The split interstitials have 2 atoms and 6 possible orientations, for a total of 12 unique sites needed to be added to every original Te/Se site. Furthermore, we defined a rotation process that changes the orientation of the interstitial, which from NEB has a transition energy of 0.5 eV. $Se_{Te} - Se_{Te}$ interactions were included for split interstitials.

In addition to KLMC, we created simple analytic models using Eq. 1.1, with parameters as shown in Table 6.2. The results from KLMC and the analytic models are plotted in Figure 6.3. It can be seen that the KLMC and analytic models agree very well for V_{Cd}^{-2}, V_{Te}^{+2}, V_{Se}^{+2}, and Cd_i^{+2}, but are less suitable for Te_i^{+0} and Se_i^{+0}. In V_{Cd}^{-2} diffusion, the diffusivity is virtually identical in both CdTe and CdSe, but lower for the alloyed material. This can be explained by the $V_{Cd} - Se_{Te}$ interactions. In both pure CdTe and CdSe, the interactions have no effect as the local Se neighborhood to the vacancy does not change with the location of the vacancy. In the alloy however, certain posi-

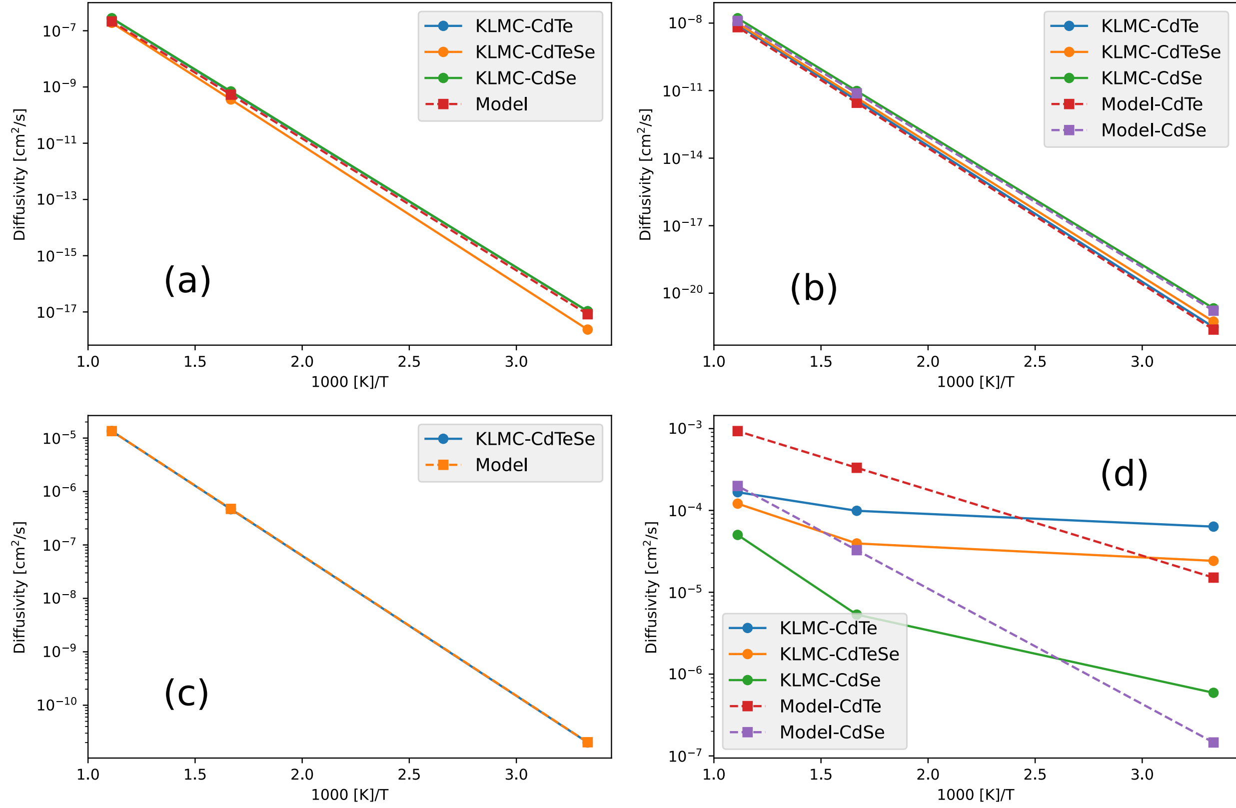

Figure 6.3: Results of KLMC simulations and analytic models for the diffusivity of various defects in CdTe, CdSeTe with a 0.25 Se/(Se+Te) ratio, and CdSe. (a) V_{Cd}. (b) $V_{Te/Se}$. (c) Cd_i. (d) Te/Se_i.

tions are more favorable given the local Se neighborhood, which effectively "locks in" the vacancy and discourages rapid diffusion. For $V_{Te/Se}$ diffusion, the vacancy diffusivity gradually increases moving from pure CdTe to pure CdSe, a result of the lower barrier of V_{Se}^{+2} compared to V_{Te}^{+2}. The Cd_i^{+2} simulation is quite simple with no interactions, thus the analytic model predicts the KLMC results nearly perfectly. Lastly with Te_i^{+0}/Se_i^{+0} diffusion, there is a general trend of decreasing diffusivity with increasing Se content, explained by the higher barrier of Se_i^{+0} migration compared to that of Te_i^{+0}. The split interstitial diffusion is more difficult to model, as there exists both a rapid [110] diffusion mechanism and a slower rotation mechanism. The rotation is not simply the rate-limiting mechanism, as the interstitials can diffuse a large distance between rotations. However, this diffusion is only 1-dimensional, and so cannot describe the overall diffusion behavior in all 3

dimensions. This unusual combination possibly leads to the non-Arrhenius behavior observed in Figure 6.3.

The results in Figure 6.3 cannot be directly compared to Figure 6.1, as Figure 6.3 gives only the diffusivity of a defect, while Figure 6.1 gives the diffusivity of the entire species, which is the sum of the products of the defect diffusivity and the defect concentration for each diffusion-mediating defect. However, because the defect concentrations are expected to be low in CdSeTe, the species diffusivities will be several orders of magnitude lower than the constituent defect diffusivities. This is generally in agreement with our results, which are several orders of magnitude greater than the experimental species diffusivities. More work is needed to develop a complete model of the species diffusivities in CdSeTe.

Chapter 7

Cd(Se,Te): As and P Doping

7.1 Introduction

Undoped CdTe films can only be made weakly p-type[19]. Cu doping is often used to improve p-type conductivity, but it may also cause device instability and degradation owing to the high diffusivity of Cu[19]. Group V pnictides such as N, P, As, and Sb, when they are substitutional on Te sites, are being considered as effective acceptors[19]. As_{Te}^{-1} and P_{Te}^{-1} form symmetric tetrahedrally coordinated acceptors (Fig. 7.1a), but they can be compensated by the formation of As_{Te}^{+1} and P_{Te}^{+1} donors, which relax into an AX center configuration. (Hereafter when we specify As, unless otherwise indicated the methodology applies also for P.) When an AX center is formed, the As atom and a neighboring Te atom will move toward each other, forming an As-Te bond while simultaneously breaking one Cd-bond each (Fig. 7.1b). The formation of these AX centers will pin the Fermi level under equilibrium growth conditions, setting a limit on doping[19]. We have developed models for the formation energy of these two competing acceptor and donor defects for alloy CdSeTe systems. We then have used KLMC simulations to predict the net doping of

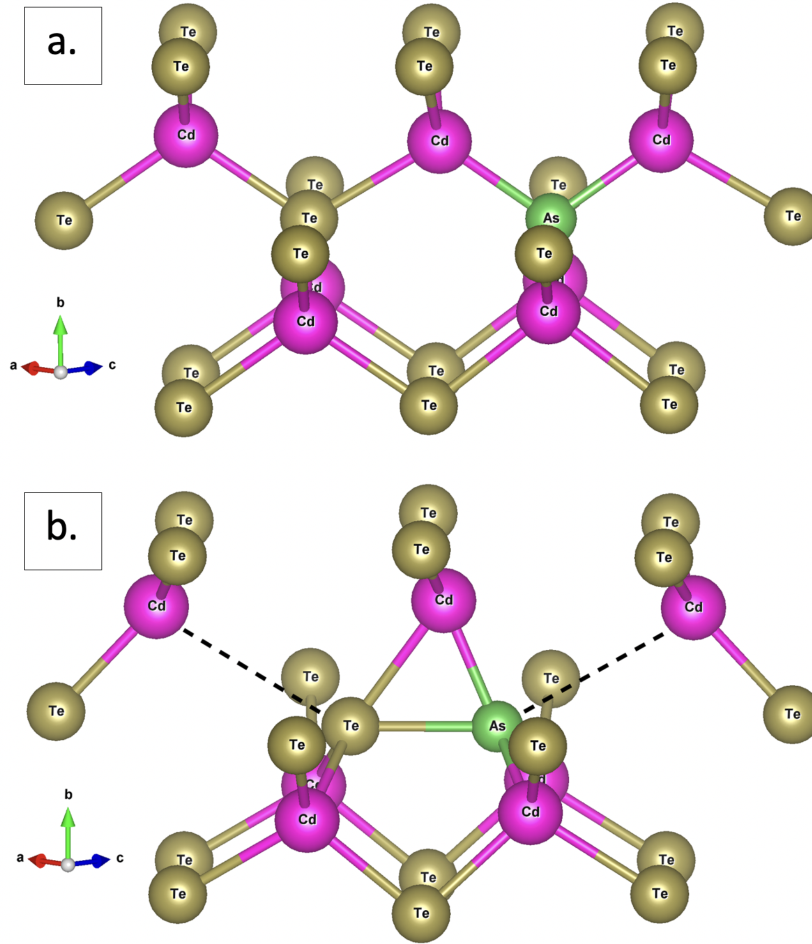

Figure 7.1: Visualization of the different possible substitutional As_{Te} configurations. (a) depicts the As_{Te}^{-1} tetrahedral structure. (b) depicts the As_{Te}^{+1} AX center structure. The dashed lines indicate bonds that break as the Te and As atoms move together to form the AX center.

CdSeTe from the presence of As_{Te} under variations in temperature, Se content, and Fermi level, by simulating the relative concentrations of As_{Te} acceptor and donor defects.

7.2 Methods

To study the net doping effectiveness of As and P in CdSeTe alloys, we employed KLMC simulations. These simulations allowed for 1NN (on the Te sublattice) exchanges of Se with Te. Because we are primarily interested in the equilibrium configurations and not the actual kinetics of the

system, we chose to use these unphysical Se-Te exchanges with an arbitrary rate constant to effectively create a Metropolis Monte Carlo simulation. We implemented this in a KLMC framework rather than a Metropolis one to build on previous KLMC simulations, and to allow the possibility of easily incorporating proper kinetics in future simulations. This choice is not expected to influence the results. A simulation consisted of 216 lattice points representing the CdTe lattice. An As atom was fixed in the center of the cell on a Te site, and remained there throughout the simulation. Se atoms were populated on Te sites, corresponding to the desired $\mathrm{k_{Se}}/(\mathrm{k_{Se}}+\mathrm{k_{Te}})$ (SST) ratio.

At each step, the energetics of the configuration were calculated before and after a Se-Te exchange. A custom rate calculator was implemented to calculate both the energy from the $\mathrm{As_{Te}}$ interacting with Se and Se-Se interactions. Previous work conducted by this group has revealed that the formation energies $E^f[\mathrm{As}_{\mathrm{Te}}^{-1}]$ and $E^f[\mathrm{As}_{\mathrm{Te}}^{+0}]$ have little dependence on local alloy arrangement, but moderate dependence on the overall SST ratio. Meanwhile, it was found that $E^f[\mathrm{As}_{\mathrm{Te}}^{+1}]$ has little dependence on the overall SST ratio, but a strong dependence on the local alloy arrangement. This suggests that Se must be carefully controlled in CdSeTe to reduce the possibility of AX structure formation. Note that we do not include the formation of compensating defect complexes, which may have a large impact on dopant activation. These will be addressed in a forthcoming work.

Our previous work identified 14 unique Te-site locations relative to the oriented AX dimer that are the main contributors to the variance in $E^f[\mathrm{As}_{\mathrm{Te}}^{+1}]$. For each site, the presence of Se on that site results in an energy change relative to the presence of Te, and the energy changes associated with each site are tabulated in Table 7.1. The locations of these sites are defined using a vector coordinate system such that $\mathrm{As_{Te}}$ is located at (0, 0, 0), the associated Te that distorts toward the $\mathrm{As_{Te}}$ in the AX structure is located at (1, 0, 0), and the Cd that neighbors both the $\mathrm{As_{Te}}$ and the

Table 7.1: Vectors given in new coordinate system (see Fig. 7.2) for locations of significant sites relative to an oriented As or P AX dimer, along with the energy change ΔE associated with the presence of Se on the site, in units of eV.

Vector:	(0.5, 0.5, -1)	(0.5, -0.5, -1)	(0.5, 0.5, 1)	(0.5, -0.5, 1)	(-0.5, 0.5, -1)
ΔE (As):	-0.100	-0.100	-0.030	-0.030	0.045
ΔE (P):	-0.110	-0.110	-0.024	-0.024	0.054
Vector:	(-0.5, -0.5, -1)	(0, 1, 2)	(0, -1, 2)	(0, 1, -2)	(0, -1, -2)
ΔE (As):	0.045	-0.015	-0.015	-0.015	-0.015
ΔE (P):	0.054	-0.017	-0.017	-0.017	-0.017
Vector:	(1.5, 0.5, 1)	(1.5, -0.5, 1)	(-1, 0, 2)	(-1, 0, -2)	
ΔE (As):	-0.020	-0.020	0.023	0.023	
ΔE (P):	-0.023	-0.023	0.009	0.009	

distorted Te is at (0.5, 0, 0.5), as shown in Fig. 7.2. Thus for an AX dimer in a given orientation, the 14 significant sites can be located using this coordinate system. In our KLMC simulations, at each step, for each of the (up to) 12 possible AX dimers, we wanted the simulation to check each of the 14 significant sites for the presence of an Se. Because the AX structure does not form between As_{Te} and Se_{Te}, the presence of Se on sites neighboring As_{Te} reduces the number of possible AX structures that can form. Given the locations of the As_{Te}, the distorted Te, and the Cd neighboring both (in the coordinates of the KLMC unit cell), the significant sites can be found by rotating the vectors in Table 7.1 by the rotation matrix given by:

$$R = \begin{bmatrix} \mathbf{a_1} & \mathbf{a_2} & \mathbf{a_3} \end{bmatrix} \begin{bmatrix} 1 & 0.5 & 0 \\ 0 & 0 & -1 \\ 0 & 0.5 & 0 \end{bmatrix}^{-1} \tag{7.1}$$

where $\mathbf{a_1}$ and $\mathbf{a_2}$ are the column vectors of the Te that is distorted toward the As and the Cd neighboring both As and the distorted Te, respectively, in the coordinates of the KLMC unit cell. The second matrix is identical for any AX dimer orientation, and the columns correspond to the

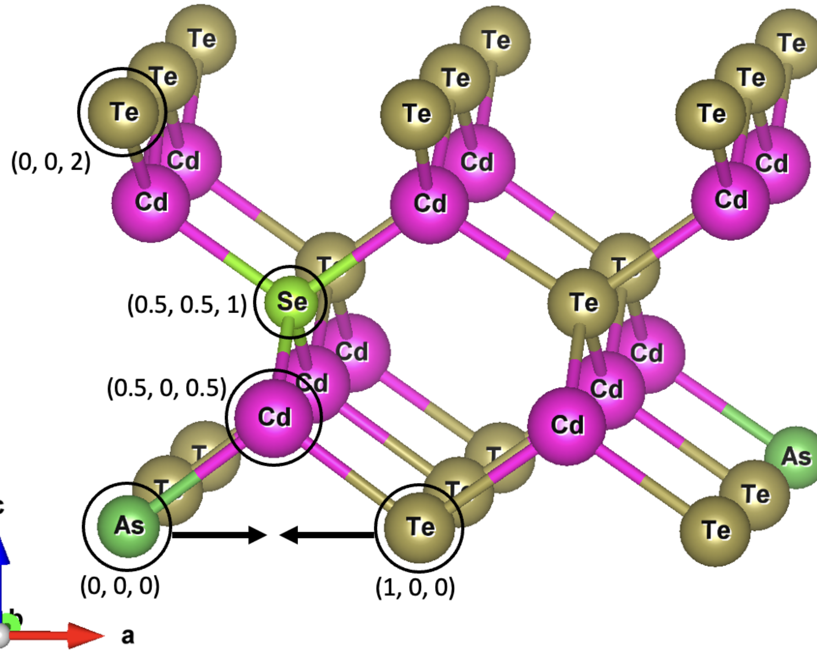

Figure 7.2: New coordinate system for defining atom locations relative to an oriented AX dimer. The coordinates are defined by As (0, 0, 0), the distorted Te (1, 0, 0), and the Cd bonded to both (0.5, 0, 0.5). Additional sites for a Se at (0.5, 0.5, 1) and a Te at (0, 0, 2) are also depicted. Black arrows show the As and Te deformation when the AX center forms.

same Te and Cd defined by $\mathbf{a_1}$ and $\mathbf{a_2}$, but in the coordinate system given in Fig. 7.2. To have an invertible matrix, a third column vector was created for each matrix from the cross product of the first two column vectors: $\mathbf{a_3} = (\mathbf{a_1} \times \mathbf{a_2}) \cdot \frac{\|\mathbf{a_1}\|}{\|\mathbf{a_1} \times \mathbf{a_2}\|}$ (the third column of the second matrix was derived in a like manner). For each significant site occupied by a Se, the associated energy from Table 7.1 is added to the baseline $E^f[\mathrm{As}_{\mathrm{Te}}^{+1}]$ in pure CdTe.

We calculated the barrier for transformation between the AX center and the symmetric tetrahedral structure and found that in both the -1 and +0 charge states, $\mathrm{As_{Te}}$ spontaneously relaxes from the AX structure to the symmetric structure. Meanwhile, in the +1 state the AX structure has a lower energy, and the transition barrier between AX and symmetric structures was found to generally be between 0.2 and 0.7 eV for different SST ratios. Therefore, even at room temperature

it is reasonable to assume that As_{Te}^{+1} will equilibrate to the AX structure.

For a fixed As location, the AX dimer can exist between the As and any neighboring Te, with up to 12 dimers possible. In our simulations, for each step we calculate the formation energy of each possible dimer orientation, and find an effective formation energy that treats the overall structure as a superposition of the individual orientations, with energy given by:

$$E^f[\mathrm{As}_{\mathrm{Te}}^{+1}] = -k_B T \ln \sum_i e^{-E_i^f[\mathrm{As}_{\mathrm{Te}}^{+1}]/k_B T} \tag{7.2}$$

$$E_i^f[\mathrm{As}_{\mathrm{Te}}^{+1}] = 1.91 + E_F + \sum_j \Delta E_j \tag{7.3}$$

$$E_i^f[\mathrm{P}_{\mathrm{Te}}^{+1}] = 2.06 + E_F + \sum_j \Delta E_j \tag{7.4}$$

where $E^f[\mathrm{As}_{\mathrm{Te}}^{+1}]$ is the effective overall formation energy for the AX structure in the simulation, $E_i^f[\mathrm{As}_{\mathrm{Te}}^{+1}]$ is the individual formation energy of each possible AX center orientation (likewise $E_i^f[\mathrm{P}_{\mathrm{Te}}^{+1}]$ applies for P doping), ΔE_j is the change in formation energy resulting from the presence of Se on a significant site (as given in Table 7.1), and E_F is the Fermi level. In effect, this is finding an effective energy that produces the same concentration of defects as the sum of the concentrations of the individual orientations possible. Because the formation energies of the symmetric structures are not dependent on the local alloy configuration, they can be found simply from:

$$E^f[\mathrm{As}_{\mathrm{Te}}^{-1}] = 2.06 + (0.24 * \mathrm{SST}) - E_F \tag{7.5}$$

$$E^f[\mathrm{P}_{\mathrm{Te}}^{-1}] = 2.04 + (0.17 * \mathrm{SST}) - E_F \tag{7.6}$$

$$E^f[\mathrm{As}_{\mathrm{Te}}^{+0}] = 1.94 - (0.40 * \mathrm{SST}^2) + (0.06 * \mathrm{SST}) \tag{7.7}$$

$$E^f[\mathrm{P}_{\mathrm{Te}}^{+0}] = 1.93 - (0.80 * \mathrm{SST}^2) + (0.68 * \mathrm{SST}) \tag{7.8}$$

The overall formation energy of an $\mathrm{As_{Te}}$ defect can be found by solving for an effective formation energy that produces the same concentration as the sum of the individual concentrations of $[\mathrm{As}_{\mathrm{Te}}^{-1}]$, $[\mathrm{As}_{\mathrm{Te}}^{+0}]$, and $[\mathrm{As}_{\mathrm{Te}}^{+1}]$:

$$E^f[\mathrm{As_{Te}}] = -k_B T \ln\left(e^{-E^f[\mathrm{As}_{\mathrm{Te}}^{-1}])/k_B T} + e^{-E^f[\mathrm{As}_{\mathrm{Te}}^{+0}])/k_B T} + \sum_i \left(e^{-E_i^f[\mathrm{As}_{\mathrm{Te}}^{+1}]/k_B T}\right)\right). \tag{7.9}$$

We defined the net doping effectiveness of a given state of the simulation as:

$$\text{Net doping effectiveness} = \frac{[\mathrm{As}_{\mathrm{Te}}^{-1}] - [\mathrm{As}_{\mathrm{Te}}^{+1}]}{[\mathrm{As}_{\mathrm{Te}}^{-1}] + [\mathrm{As}_{\mathrm{Te}}^{+0}] + [\mathrm{As}_{\mathrm{Te}}^{+1}]}. \tag{7.10}$$

Each step in the simulation can be viewed as a potential local arrangement that might exist around an As dopant in a real system. If this local arrangement occurs many times simultaneously in a real system, the net doping effectiveness of the arrangement is the average doping the As atoms with this local Se neighborhood will contribute, based on the relative concentrations of the acceptor, donor, and neutral charge states. Our convention defines a net doping effectiveness of 1 as maximal *p*-type acceptor (desired) doping, and -1 as maximal *n*-type donor (undesirable) doping. A value of 0 indicates that the different charge states cancel each other out, so there is no overall contribution to net doping. The average value of the net doping effectiveness over all the structures that occur in the simulation can be then seen as the overall effectiveness of As as a *p*-type dopant in the system.

At each step in the simulation, we record the net doping effectiveness and the overall formation energy $E^f[\mathrm{As_{Te}}]$. Additionally, we include Se-Se interactions, having determined a repulsive 0.0123 eV 1NN Se-Se interaction exists. The difference between $E^f[\mathrm{As_{Te}}]$ before and after a Se-

Te swap and the difference between the sum of Se-Se interactions before and after the swap are combined and used to modify the rate constant. As mentioned previously, while the absolute rate constant is not physically meaningful, the relative change in energetics reflected here is important for moving the simulation towards an equilibrium alloy configuration.

7.3 Results and Discussion

7.3.1 Maximum dopability and net doping effectiveness

Simulations were run for 25,000 steps, for varying temperatures, Fermi levels, and Se content, for both As and P dopants. After an initial equilibration period, the net doping effectiveness was averaged over all steps for every run. Initially, for each temperature and SST ratio of interest, several different Fermi levels were run, and the results used to narrow in on the "break-even" Fermi level, meaning the Fermi level (for a given temperature and SST ratio) that sets the net doping effectiveness to 0. At the break-even Fermi level, any additional As added to the material will have no further impact on the equilibrium doping level, as all As_{Te}^{-1} defects will be equally compensated by As_{Te}^{+1} defects. The break-even Fermi levels are plotted in Fig. 7.3. The simulations were then run again using Fermi levels ranging from -1, -0.5, 0, +0.5, and +1 k_bT above and below the respective break-even Fermi levels, to study the behavior of the system as it approaches the break-even Fermi level. A positive value of net doping effectiveness indicates that additional As added to the material will contribute to overall *p*-type doping, while a negative value indicates additional As will contribute to overall *n*-type doping. When the net doping effectiveness tends to 1, this indicates that all additional As dopants will behave as acceptors. Fig. 7.4 plots the net doping effectiveness for different conditions for As dopants, and Fig. 7.5 for P dopants.

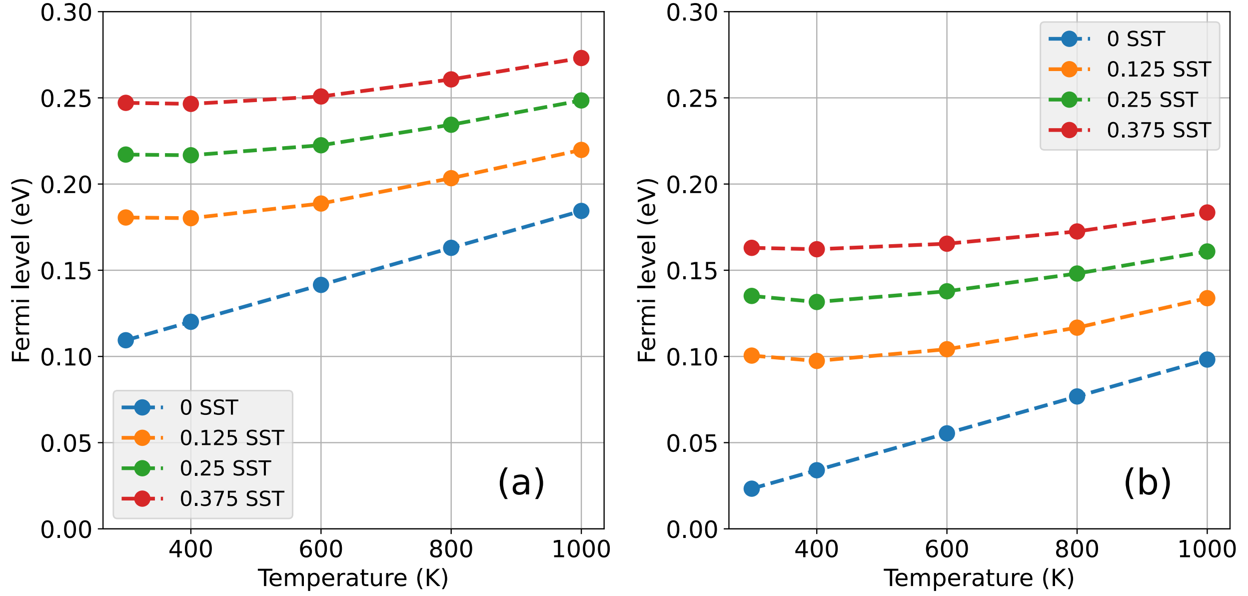

Figure 7.3: Temperature dependence of the break-even Fermi level (where $[\text{As}_{\text{Te}}^{-1}]$=$[\text{As}_{\text{Te}}^{+1}]$), for several SST ratios. (a) presents results for As dopants and (b) for P dopants.

In Figs. 7.4 and 7.5 for a given curve, the break-even Fermi level is the Fermi level where the net doping effectiveness is equal to 0. Starting with material possessing a Fermi level above the break-even Fermi level, additional As dopants added to the system will push the Fermi level down until reaching the break-even Fermi level. At the break-even Fermi level, additional As will self-compensate and leave the Fermi level unchanged. Likewise, starting with material possessing a Fermi level below the break-even Fermi level, additional As will raise the Fermi level to the break-even Fermi level, but not beyond. Thus, addition of As to CdSeTe will always tend to push the material to the break-even Fermi level, which represents the maximum *p*-type doping achievable with As in the absence of other doping species.

Figs. 7.3, 7.4, and 7.5 show that the break-even Fermi level consistently increases as the Se content increases, suggesting that As is an effective acceptor dopant in CdTe, but is significantly less effective as Se alloying increases. Eqs. 7.5 and 7.6 show that $E^f[\text{As}_{\text{Te}}^{-1}]$ increases with increasing Se content, while $E^f[\text{As}_{\text{Te}}^{+1}]$ is not directly dependent on overall Se content. However, increasing

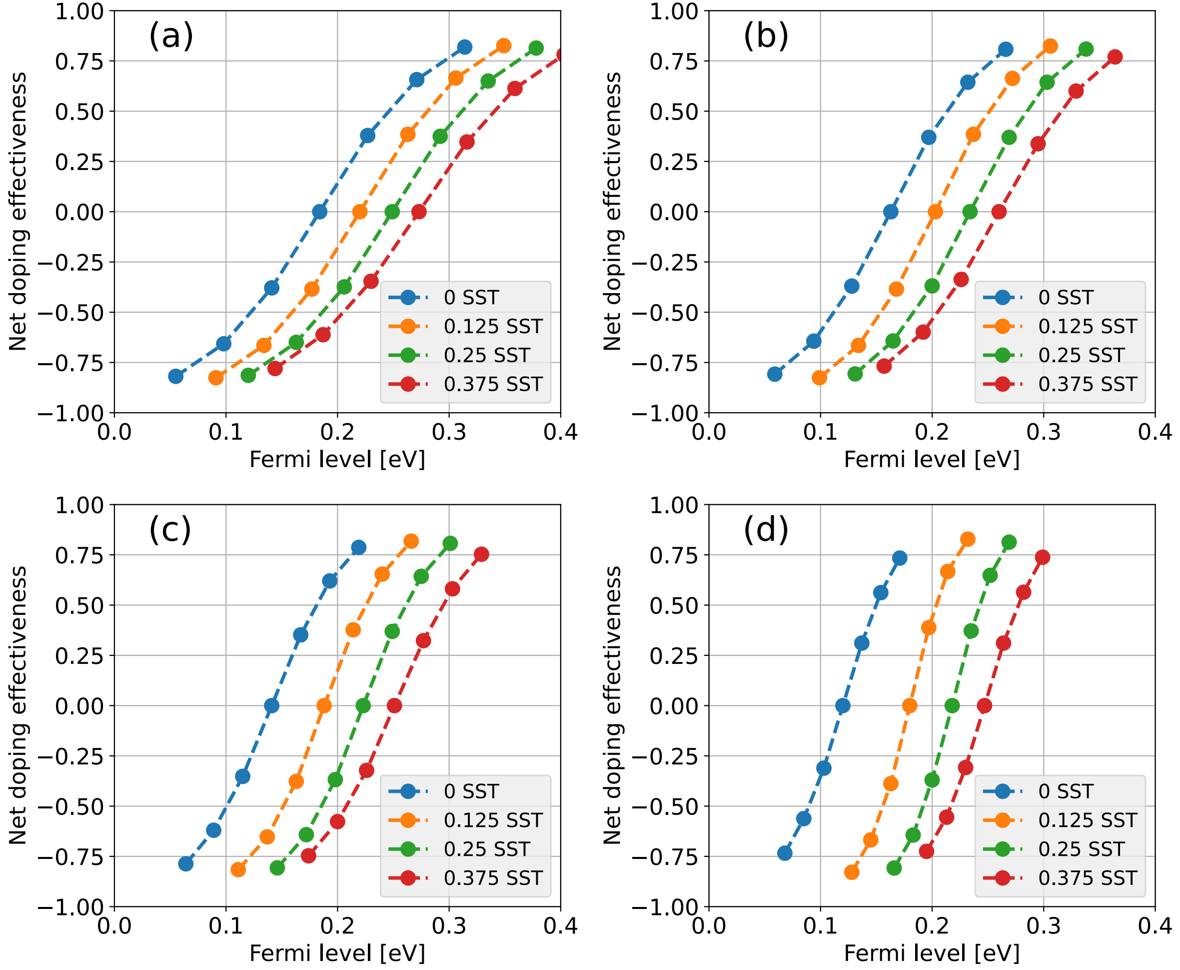

Figure 7.4: Net doping effectiveness of As substitutional defects in CdSeTe at varying Fermi levels, SST ratios, and temperatures. (a) is at 1000K, (b) is at 800K, (c) is at 600K, (d) is at 400K.

Se content increases the probability of occupation of a significant site by Se, which more often (see Table 7.1) tends to reduce $E^f[\mathrm{As}_{\mathrm{Te}}^{+1}]$. Because higher Se content decreases $E^f[\mathrm{As}_{\mathrm{Te}}^{+1}]$ and increases $E^f[\mathrm{As}_{\mathrm{Te}}^{-1}]$, $\mathrm{As}_{\mathrm{Te}}^{+1}$ will be increasingly favored over $\mathrm{As}_{\mathrm{Te}}^{-1}$, leading the break-even Fermi level to increase, as observed in our models. Note that in pure CdTe, the $\mathrm{As}_{\mathrm{Te}}$ can always form 12 AX dimers with neighboring Te atoms, but as Se content is increased, the number of available Te neighbors decreases, which causes $\mathrm{As}_{\mathrm{Te}}^{+1}$ formation to become less favorable, opposing the overall trend. While this effect was observed to shift higher-Se-content curves in Figs. 7.4 and 7.5 to lower Fermi levels, it is not enough to overcome the opposing factors previously described.

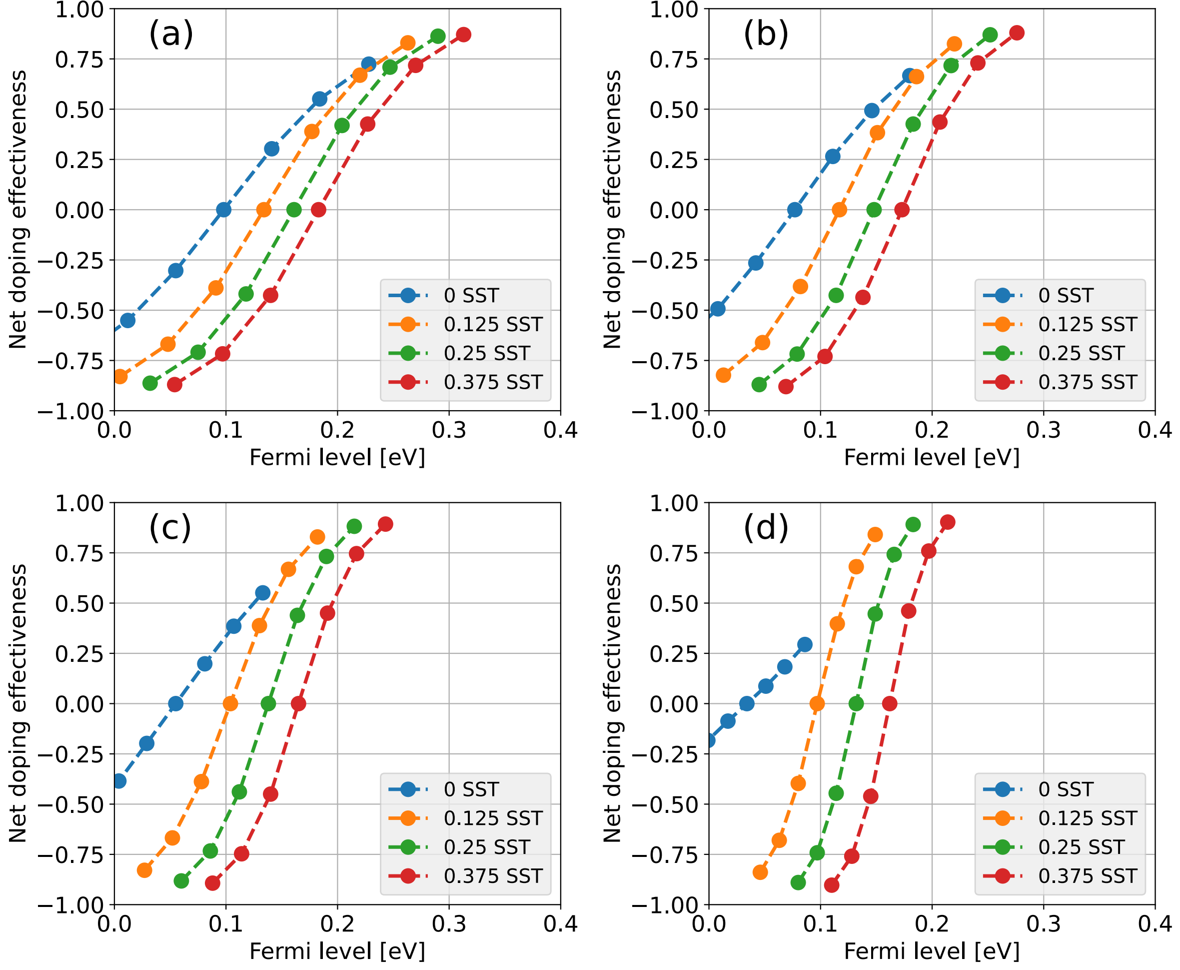

Figure 7.5: Net doping effectiveness of P substitutional defects in CdSeTe at varying Fermi levels, SST ratios, and temperatures. (a) is at 1000K, (b) is at 800K, (c) is at 600K, (d) is at 400K.

There also is observed a trend of increasing break-even Fermi level with increasing temperature. This trend is the most pronounced in pure CdTe (see Fig. 7.3), which is the simplest to consider as the local arrangement of Se is irrelevant. In CdTe, because all 12 potential AX center orientations are available and have identical formation energies, Eq. 7.2 reduces to $E^f[\mathrm{As}_{\mathrm{Te}}^{+1}] = 1.91 + E_F - k_B T \ln(12)$. The third term here represents the configurational entropy due to the multiplicity of orientations possible for the AX center. As temperature increases, the break-even Fermi level must increase to balance $E^f[\mathrm{As}_{\mathrm{Te}}^{+1}]$ with $E^f[\mathrm{As}_{\mathrm{Te}}^{-1}]$, which is independent of temperature. This trend also applies to the alloy, although developing a simple expression for

the configurational entropy becomes complicated by the presence of Se, which often reduces the number of AX structures that can form and changes their individual formation energies.

In contrast to the general trend of increasing break-even Fermi level with increasing temperature, at lower temperatures there is a relative boost to the break-even Fermi level seen in Fig. 7.3 when Se content is increased, beyond a simple translation of the linear 0 SST curve upwards. We have identified at least two independent causes for the low-temperature boost in the alloy. First, at high temperatures for the alloy systems, the Se configuration will approach a random arrangement, while at low temperatures the Se configuration will increasingly be driven to the lowest-energy arrangement. This is done in part by arranging the Se atoms to minimize $E^f[\mathrm{As}_{\mathrm{Te}}]$. As $E^f[\mathrm{As}_{\mathrm{Te}}^{-1}]$ is independent of Se arrangement and temperature in our simulations, this minimization has the effect of just minimizing $E^f[\mathrm{As}_{\mathrm{Te}}^{+1}]$, and consequently increasing the ratio of $\mathrm{As}_{\mathrm{Te}}^{+1}$ relative to $\mathrm{As}_{\mathrm{Te}}^{-1}$ as the temperature is lowered, increasing the break-even Fermi level. It is not trivial to predict if occupying a site with Se is favorable, as a site which is favorable to one AX configuration may be unfavorable to other AX configurations. Thus the simulation will find a balance between all these competing factors, and this illustrates the necessity of using Monte Carlo models to capture the complex behavior occurring.

The second cause for the low-temperature boost in the alloy arises from the presence of the $\mathrm{As}_{\mathrm{Te}}^{+0}$ charge state. Consider that the break-even Fermi level is defined as the Fermi level that sets the average net doping effectiveness of a simulation to zero. The average net doping effectiveness is calculated from the individual net doping effectiveness (Eq. 7.10) at each step. For the average to equal zero, some steps will have positive values of the net doping effectiveness, and some will have negative values. First consider Eq. 7.10 when $\mathrm{As}_{\mathrm{Te}}^{+0}$ is excluded from the simulation. $[\mathrm{As}_{\mathrm{Te}}^{-1}]$ will remain constant for every step as its value depends only on global parameters. Thus, whether the

individual net doping effectiveness of a given step is positive or negative will depend on whether $E^f[\mathrm{As}_{\mathrm{Te}}^{+1}]$ is less than or greater than the constant value of $E^f[\mathrm{As}_{\mathrm{Te}}^{-1}]$. Adding in $\mathrm{As}_{\mathrm{Te}}^{+0}$ will have the effect of scaling down the individual net doping effectiveness of a step without changing the sign. Because the values of $[\mathrm{As}_{\mathrm{Te}}^{-1}]$ and $[\mathrm{As}_{\mathrm{Te}}^{+0}]$ are constant throughout a single simulation, the magnitude of the scaling caused by the addition of $\mathrm{As}_{\mathrm{Te}}^{+0}$ to Eq. 7.10 will only depend on the magnitude of $[\mathrm{As}_{\mathrm{Te}}^{+1}]$ for a given step. First let us consider the situation where $[\mathrm{As}_{\mathrm{Te}}^{+0}] << [\mathrm{As}_{\mathrm{Te}}^{-1}]$. Since this holds true throughout the duration of the simulation, whether $\mathrm{As}_{\mathrm{Te}}^{+0}$ is included or not will have minimal impact on the individual net doping effectiveness values and consequently will not impact the average net doping effectiveness value. But when $[\mathrm{As}_{\mathrm{Te}}^{+0}] >> [\mathrm{As}_{\mathrm{Te}}^{-1}]$, if the net doping effectiveness of a certain step is positive, it indicates that $[\mathrm{As}_{\mathrm{Te}}^{+1}] < [\mathrm{As}_{\mathrm{Te}}^{-1}]$ and by extension $[\mathrm{As}_{\mathrm{Te}}^{+1}] << [\mathrm{As}_{\mathrm{Te}}^{+0}]$, in which case including 0 will significantly scale down the net doping effectiveness. But if the net doping effectiveness of a certain step is negative, it indicates that $[\mathrm{As}_{\mathrm{Te}}^{+1}] > [\mathrm{As}_{\mathrm{Te}}^{-1}]$, in which case it may even be true that $[\mathrm{As}_{\mathrm{Te}}^{+1}] >> [\mathrm{As}_{\mathrm{Te}}^{+0}]$, and addition of $\mathrm{As}_{\mathrm{Te}}^{+0}$ will not impact the net doping effectiveness. Taken together, this shows that positive values will be scaled down more than negative value upon inclusion of the $+0$ charge state, which will have the aggregate effect of reducing the average net doping effectiveness. To compensate, the break-even Fermi level will increase. At lower temperatures, small differences between the formation energies of the different charge states will lead to the differences between the relative concentrations to become more pronounced, enhancing the scaling effect and explaining why we observe a larger boost to the break-even Fermi level at lower temperatures. This result may seem counterintuitive, as Eq. 7.10 appears to imply that the break-even Fermi level should only depend on when $[\mathrm{As}_{\mathrm{Te}}^{+1}] = [\mathrm{As}_{\mathrm{Te}}^{-1}]$, regardless of the value of $[\mathrm{As}_{\mathrm{Te}}^{+0}]$. But the effect occurs because each individual value of the net doping effectiveness is generally not equal to 0 even when the average is equal to 0, so the presence

of As_{Te}^{+0} does in fact alter the average net doping effectiveness. Additionally, this effect will only occur when $[As_{Te}^{+1}]$ can vary from step to step, which is only possible when Se is present, explaining why the boost is not observed for pure CdTe.

We find that both the first cause (related to Se ordering) and the second cause (related to the presence of the As_{Te}^{+0} charge state) are responsible for the boost effect seen in the break-even Fermi levels. In particular, the two causes appear to be inversely related: when $E^f[As_{Te}^{+0}]$ is higher, the effect is primarily due to the first cause, while when $E^f[As_{Te}^{+0}]$ is lower, the effect is primarily due to the second cause. This occurs because for the simulation to favor Se moving from one location to another, the formation energy given by Eq. 7.9 must be lowered by swapping the locations of a Te and a Se. Because only $E^f[As_{Te}^{+1}]$ depends on the local alloy arrangement, the summation term in Eq. 7.9 pertaining to $E^f[As_{Te}^{+1}]$ must change significantly enough to alter the overall $E^f[As_{Te}]$ noticeably. However, if $E^f[As_{Te}^{+0}]$ is low enough (which it sometimes is in our simulations), its exponential term in Eq. 7.9 will overwhelm any changes to $E^f[As_{Te}^{+1}]$. This effectively removes the driving force for arranging Se into a lower-energy configuration. (Note that while $E^f[As_{Te}^{-1}]$ also does not depend on the local alloy arrangement, at the break-even Fermi level $[As_{Te}^{-1}] = [As_{Te}^{+1}]$. Therefore, a lower value of $E^f[As_{Te}^{-1}]$ will alter the break-even Fermi level, but it will not remove the driving force mentioned above as $[As_{Te}^{+1}]$ is always significant relative to $[As_{Te}^{-1}]$ near the break-even Fermi level). Thus, a lower value of $E^f[As_{Te}^{+0}]$ both suppresses the first cause while contributing to the second cause, and vice versa when $E^f[As_{Te}^{+0}]$ is higher. In most cases, we find a mixture of both causes at play in our simulations. The combined effect tends to be the same magnitude regardless of which cause is dominant, and so the break-even Fermi levels are constant even when $E^f[As_{Te}^{+0}]$ varies.

Another interesting trend can be seen in Figs. 7.4 and 7.5, where the curves become flattened at

lower temperatures and lower SST ratios, especially for P doping in pure CdTe. By this we mean that although all curves range from $\pm k_b T$ around their respective break-even Fermi levels, the net doping effectiveness may range from up to ± 0.9 to less than ± 0.25 net doping effectiveness. This is caused by the presence of $\mathrm{As}_{\mathrm{Te}}^{+0}$. When $\mathrm{As}_{\mathrm{Te}}^{+0}$ is not included, all curves range from about ± 0.9 net doping effectiveness. When $[\mathrm{As}_{\mathrm{Te}}^{+0}]$ is much greater than $[\mathrm{As}_{\mathrm{Te}}^{-1}]$ and $[\mathrm{As}_{\mathrm{Te}}^{+1}]$, as previously explained its presence scales down the net doping effectiveness. This is particularly pronounced at lower temperatures, where small differences between $E^f[\mathrm{As}_{\mathrm{Te}}^{+0}]$ compared to $E^f[\mathrm{As}_{\mathrm{Te}}^{-1}]$ or $E^f[\mathrm{As}_{\mathrm{Te}}^{+1}]$ lead to much larger differences in concentrations. Additionally, as the break-even Fermi level increases (either when moving from low to high temperature or from low to high SST ratios) the break-even value of $E^f[\mathrm{As}_{\mathrm{Te}}^{-1}] = E^f[\mathrm{As}_{\mathrm{Te}}^{+1}]$ tends to decrease. Since $E^f[\mathrm{As}_{\mathrm{Te}}^{+0}]$ is independent of the Fermi level, this trend reduces the scaling effect caused by $\mathrm{As}_{\mathrm{Te}}^{+0}$ by reducing the difference between $[\mathrm{As}_{\mathrm{Te}}^{-1}]$ and $[\mathrm{As}_{\mathrm{Te}}^{+1}]$ compared to $[\mathrm{As}_{\mathrm{Te}}^{+0}]$. Note that in our simulations this only occurs when $E^f[\mathrm{As}_{\mathrm{Te}}^{+0}]$ is less than $E^f[\mathrm{As}_{\mathrm{Te}}^{-1}] = E^f[\mathrm{As}_{\mathrm{Te}}^{+1}]$ (at the break-even Fermi level); when it is much higher $[\mathrm{As}_{\mathrm{Te}}^{+0}]$ is too low to affect the results.

In general, the behavior of P as a dopant is qualitatively very similar to that of As, and so our discussion of As doping applies to P doping as well. The primary difference between As and P doping is that the break-even Fermi levels are shifted noticeably downward with P compared to As (see Figure 7.3). Likewise, the net doping effectiveness curves for P are shifted to lower Fermi levels compared to As. This is significant, as it implies that P is likely to have higher activation than As in CdSeTe systems, in situations where activation is limited by AX formation. The main driver of this difference is the higher baseline formation energy of $\mathrm{P}_{\mathrm{Te}}^{+1}$ compared to $\mathrm{As}_{\mathrm{Te}}^{+1}$ (2.06 in Eq. 7.4 compared to 1.91 in Eq. 7.3). This makes AX formation less favorable for P dopants relative to As dopants, allowing the Fermi level to be pushed lower before AX self-compensation

becomes significant.

The next largest difference between As and P dopants is the formation energy of P_{Te}^{+0} compared to As_{Te}^{+0}, which ranges from a difference of 0.01 to 0.17 eV for Se alloy ratios ranging from 0 to 0.375, with the formation energy of P_{Te}^{+0} being consistently larger than that of As_{Te}^{+0}. This leads to a lower concentration of P_{Te}^{+0} relative to its As_{Te}^{+0} counterpart. This could result in less flattening (as described previously) of the net doping effectiveness curves for P_{Te}. However, it is also true that the values of $E^f[P_{Te}^{-1}] = E^f[P_{Te}^{+1}]$ at the break-even Fermi level are also consistently larger than the values of $E^f[As_{Te}^{-1}] = E^f[As_{Te}^{+1}]$ at the break-even Fermi level for the same temperature and SST ratio. In pure CdTe, where $E^f[As_{Te}^{+0}]$ and $E^f[P_{Te}^{+0}]$ are nearly equal to each other, the much larger values of $E^f[P_{Te}^{-1}] = E^f[P_{Te}^{+1}]$ at the break-even Fermi level compared to those of As mean that in pure CdTe, P_{Te}^{+0} is more significant relative to P_{Te}^{+1} and P_{Te}^{-1} compared to the significance of As_{Te}^{+0} relative to As_{Te}^{+1} and As_{Te}^{-1}. This explains the much greater flattening of P in pure CdTe compared to that of As. But for CdSeTe, the increase in $E^f[P_{Te}^{+0}]$ compared to $E^f[As_{Te}^{+0}]$ is greater than the increase of $E^f[P_{Te}^{-1}] = E^f[P_{Te}^{+1}]$ at the break-even Fermi level compared to $E^f[As_{Te}^{-1}] = E^f[As_{Te}^{+1}]$ at the break-even Fermi level. As a result, in CdSeTe, the net doping effectiveness curves for P are less flat than those for As.

7.3.2 Relation between dopant concentration and Fermi level

Using these results, we then calculated the As_{Te} concentration necessary to achieve a desired Fermi level. Overall charge neutrality requires that

$$N_D^+ + p = N_A^- + n \tag{7.11}$$

where N_D^+ and N_A^- are the concentration of ionized donors and acceptors respectively. Rearranging Eq. 7.11 gives

$$p - n = N_A^- - N_D^+ \tag{7.12}$$

which with As as the only dopant, this can be rewritten as

$$p - n = [\mathrm{As}_{\mathrm{Te}}^{-1}] - [\mathrm{As}_{\mathrm{Te}}^{+1}]. \tag{7.13}$$

Dividing by the net doping effectiveness (Eq. 7.10) gives

$$[\mathrm{As}_{\mathrm{Te}}] = \frac{p - n}{\text{Net doping effectiveness}} \tag{7.14}$$

For a known Fermi level E_F (relative to the valence band), n and p are given by

$$n = N_C \exp\left(-\frac{E_G - E_F}{kT}\right),\ N_C = 2\left(\frac{2\pi m_e^* kT}{h^2}\right)^{\frac{3}{2}} \tag{7.15}$$

$$p = N_V \exp\left(-\frac{E_F}{kT}\right),\ N_V = 2\left(\frac{2\pi m_h^* kT}{h^2}\right)^{\frac{3}{2}} \tag{7.16}$$

where E_G is the band gap, N_C and N_V are the effective densities of states in the conduction and valence bands respectively, and m_e^* and m_h^* are the effective masses of the electron and hole respectively. As a function of temperature T and SST ratio, E_G can be approximated by

$$1.79(\mathrm{SST}) + 1.49(1 - \mathrm{SST}) - 0.9(\mathrm{SST})(1 - \mathrm{SST}) - \frac{0.00059T^2}{T + 160} + 0.116. \tag{7.17}$$

Note that the first three terms that depend on SST ratio were calculated by our group previously for CdSeTe at 300K, while the remaining two terms that incorporate temperature dependence were calculated by Ref. [90] for pure CdTe only. Because we could not identify any work that incorporates both temperature dependence and SST ratio dependence, we find this approximation to be reasonable.

For a given Fermi level, the net doping effectiveness is known from the simulations (see Figs. 7.4 and 7.5). With E_F, T, and SST specified, we can calculate n and p, and find $[\mathrm{As_{Te}}]$. The

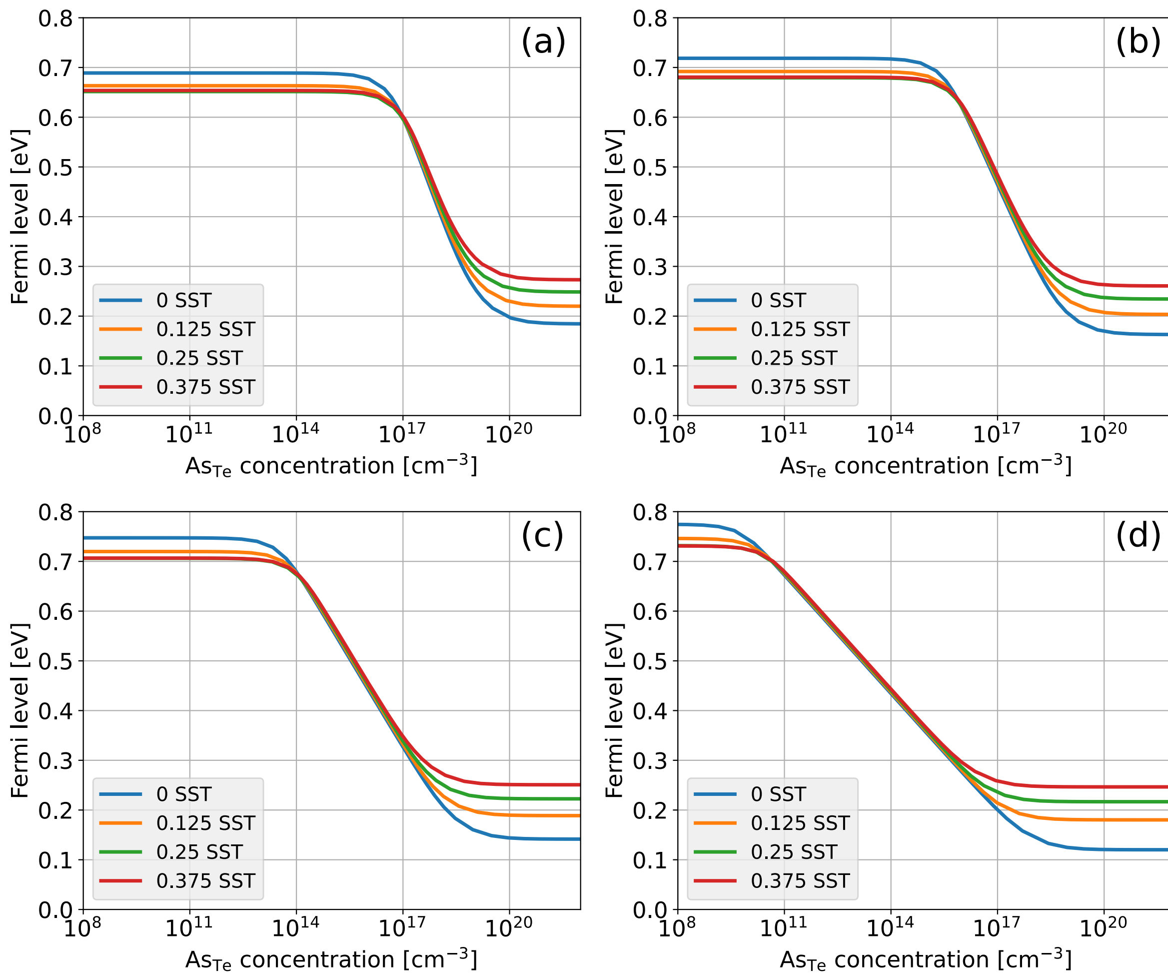

Figure 7.6: Fermi level as a function of $\mathrm{As_{Te}}$ concentration in CdSeTe, for varying SST ratios and temperatures. (a) is at 1000K, (b) is at 800K, (c) is at 600K, (d) is at 400K.

results are plotted in Figures 7.6 and 7.7. The same trends as before are apparent, with both

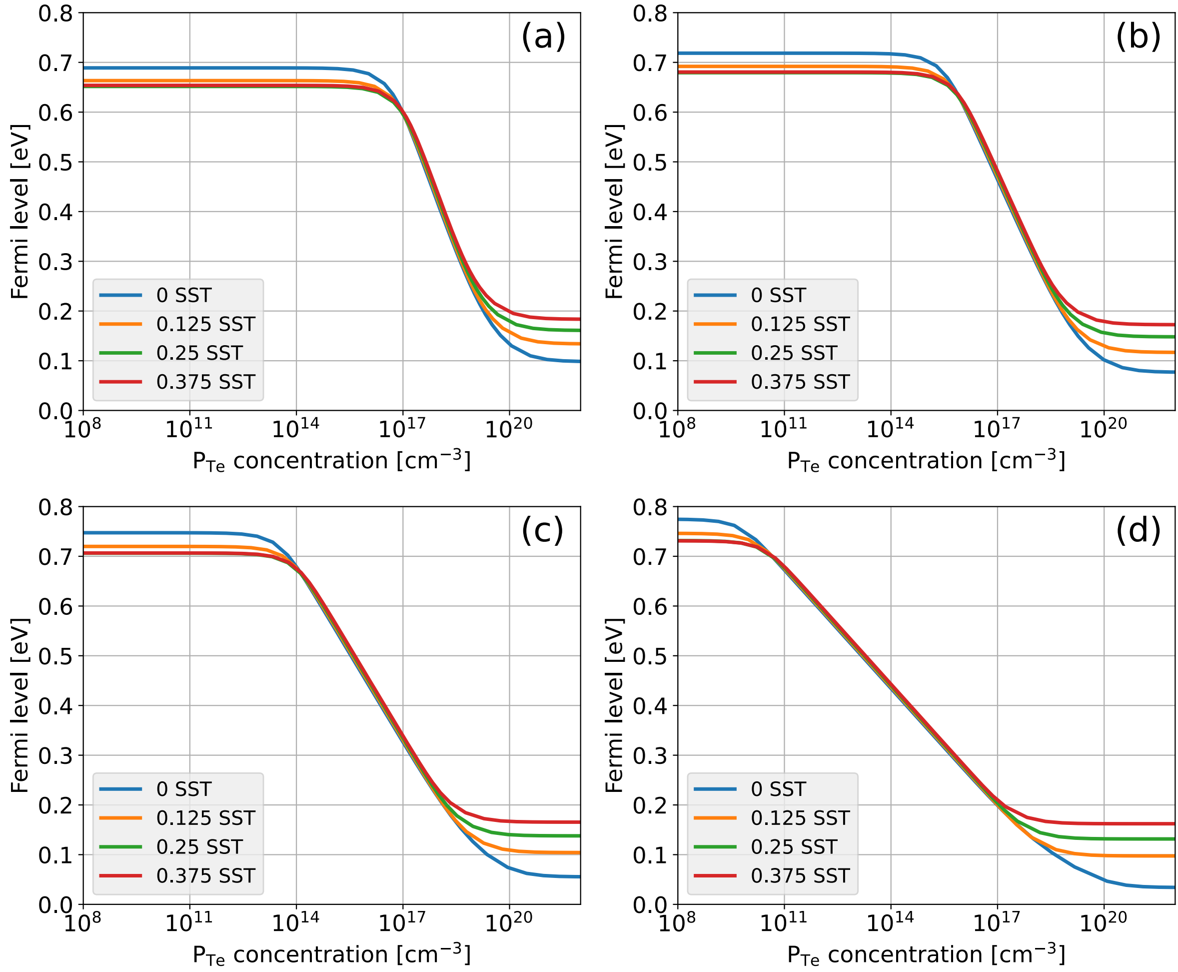

Figure 7.7: Fermi level as a function of P_{Te} concentration in CdSeTe, for varying SST ratios and temperatures. (a) is at 1000K, (b) is at 800K, (c) is at 600K, (d) is at 400K.

increasing Se content and increasing temperature reducing the maximum achievable *p*-type doping. Additionally, it is clear that in the absence of complex formation, at high dopant concentrations a lower Fermi level can be achieved using P dopants than As dopants. At the limits of experimentally achievable doping in the low 10^{17} cm^{-3} range[19], the temperature dependence becomes much more pronounced.

7.3.3 Effects of quenching on doping

Because of the possibility that the Se arrangement is less favorable to the detrimental As_{Te}^{+1} structures at high temperatures than at low temperatures, we decided to test the effects of a rapid quench from high temperature to low temperature. Such a quench should freeze in the desired high-temperature arrangement of Se and reduce the formation of As_{Te}^{+1}, lowering the Fermi level at operating temperatures. In order to simulate such a quench, we assume that it can be modeled using a sampling of the Se configurations from a high temperature run, but calculating the net doping effectiveness at a low temperature. Throughout the quench, the concentration of As_{Te} must remain constant in the system. However, this variable is not directly controlled in our simulations, but rather the Fermi level is. Because the Fermi level varies as the temperature is lowered, we must calculate the self-consistent Fermi level at the low temperature that produces the same As_{Te} concentration as at the high temperature.

To do this, we first ran an ordinary simulation at 1000K for 25,000 steps, and each step output the change in formation energy due to the local Se configuration (ΔE_j in Eqs. 7.3 and 7.4) for each of the 12 possible AX orientations. With this data saved outside the simulation, we applied Eqs. 7.2 through 7.17 to calculate the concentration of As_{Te} for the temperature, SST ratio, and Fermi level used in the simulation. We then changed the temperature to 300K and recalculated the As_{Te} concentration, using the data for the Se arrangement from the high temperature run. Finally, we varied the Fermi level in our calculations to find the value that fixes the As_{Te} concentration to the concentration calculated at 1000K. This value is then the Fermi level at 300K after quenching the system from 1000K, keeping the As_{Te} concentration fixed.

The results of these calculations are depicted in Figure 7.8. Only the high As_{Te} concentration range is depicted, as we found that for lower concentrations the equilibrated and quenched simula-

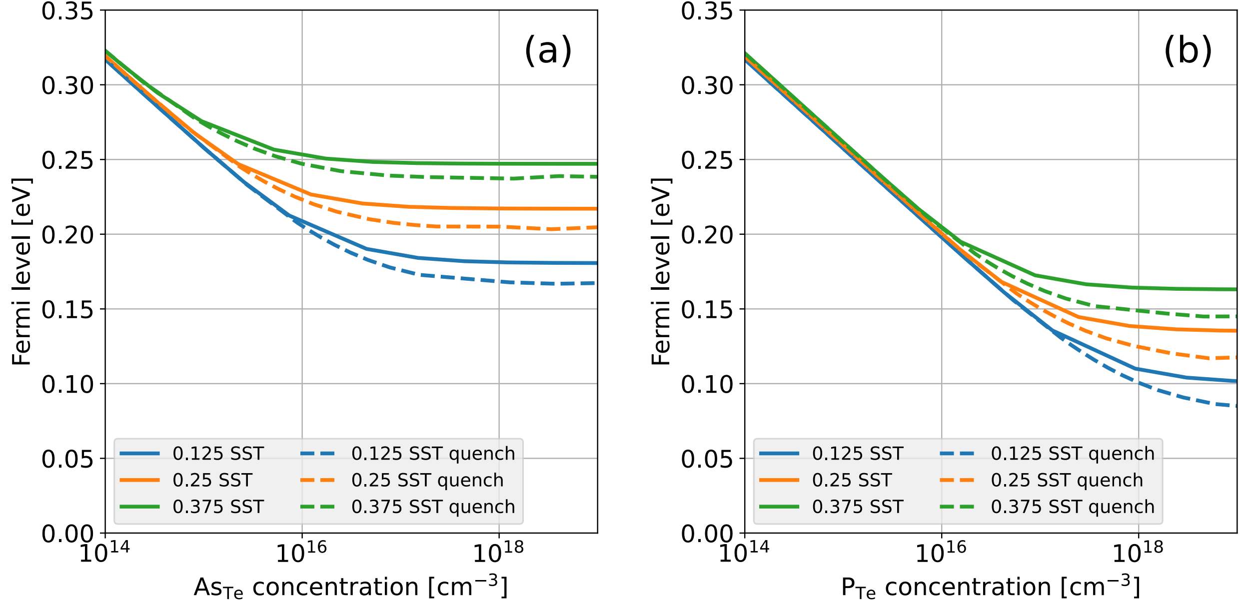

Figure 7.8: Fermi level as a function of As_{Te} concentration in CdSeTe, for varying SST ratios. Solid lines depict simulations that were allowed to equilibrate at 300K, while dashed lines depict simulations that were quenched from 1000K to 300K. (a) presents results for As dopants and (b) for P dopants.

tions produce identical results. This occurs because at lower As_{Te} concentrations, the Fermi level is high enough that As_{Te}^{-1} overwhelmingly dominates. Because As_{Te}^{-1} only depends on the global SST ratio and not the local Se arrangement, the quench has no effect as it only serves to alter the local Se arrangement. In the high As_{Te} concentration regime, quenching reduces the break-even Fermi level as expected, although the reduction is fairly modest. Because quenching freezes in a structure less favorable to detrimental As_{Te}^{+1} formation, *p*-type doping becomes easier and the break-even Fermi level is lowered. Despite this improvement, quenching is still not sufficient to overcome the increase in break-even Fermi level caused by addition of Se. Thus, our results suggest *p*-type doping will be harder to achieve in higher Se-content material, even with quenching.

Table 7.2 records the average fraction of Te sites neighboring the As_{Te} defect that are occupied by an Se throughout the simulation, for both the 1000K the 300K equilibrated structures. As expected, the fractions for structures at 1000K are very similar to the overall SST ratios, indicating

Table 7.2: Fraction of Te sites neighboring the As_{Te} occupied by Se, at different SST ratios, for both the structure quenched from 1000K and the structure allowed to equilibrate at 300K.

SST	Quenched from 1000K	Equilibrated at 300K
0.125	0.133	0.176
0.25	0.271	0.311
0.375	0.405	0.412

a nearly random Se distribution. Once the structure equilibrates at the lower 300K temperature however, the fraction occupied by Se increases noticeably, demonstrating that the system is driving the Se arrangement to a low energy minimum. The increases are still relatively small overall, which fits with the results in Figure 7.8 that also show a noticeable, but still relatively small, change in Fermi level upon quenching. The results for P doping are qualitatively very similar to those for As doping as shown in Table 7.2.

We found that if $E^f[As_{Te}^{+0}]$ decreases even slightly from our current calculated values, it can significantly reduce and even eliminate the effects of quenching. As previously described, high values of $[As_{Te}^{+0}]$ can suppress the formation of Se arrangements favorable to AX structure formation, and consequently a quench will have no additional effect on the system. For example, while we treat As_{Te}^{+0} as a delocalized charge (such that there is a net local charge on the nuclei not compensated for by the delocalized electrons/holes), we found that if we instead treat it as a localized charge, $E^f[As_{Te}^{+0}]$ decreases by about 0.1 eV. This change is enough to completely eliminate the effects of quenching, and we confirmed that when using the lower values for $E^f[As_{Te}^{+0}]$, the fraction of Te sites neighboring the As_{Te} occupied by Se at 300K becomes identical to the values at 1000K. This demonstrates that the increased concentration of As_{Te}^{+0} moves the system towards a nearly random Se configuration. Likewise, if As_{Te}^{+0} is removed completely from the simulation (such as when setting $E^f[As_{Te}^{+0}]$ to an arbitrarily large value), the fraction of Te sites neighboring the As_{Te} occupied by Se (at 300K) increases from the current values shown in Table 7.2. This suggests

that the presence of As_{Te}^{+0} does currently somewhat reduce the effect of the quench by suppressing the number of Se neighboring the As_{Te}. These results illustrate how sensitive the behavior of the system is to the input parameters, and the importance of obtaining robust DFT values.

7.3.4 Comparison with previous literature

Previous computational studies have attempted to calculate the break-even Fermi level, although only in CdTe. The values obtained for As doping range from finding no energy level within the gap where As_{Te}^{+1} is stable[91],[92], 0.12 eV[93], 0.21 eV[94], 0.36 eV[95], and 0.40 eV[96]. Likewise for P doping, the values range from finding no energy level within the gap[91],[92], 0.16 eV[94], 0.31 eV[97], and 0.32 eV[95]. In general, these results reflect a somewhat lower break-even Fermi level for P compared to As, consistent with our findings. However, none of these studies considered the configurational entropy due to the existence of 12 possible As_{Te}^{+1} distortions for any one As_{Te}, but instead only reported the $+/-$ charge transition level as the break-even Fermi level. If we exclude configurational entropy, our calculations produce a $+/-$ charge transition level of 0.08 eV for As in CdTe (and no value is stable within the gap for P), which is on the lower end of the previously reported results. The inclusion of configurational entropy can significantly increase the actual break-even Fermi level, up to an increase of 0.11 eV at 1000K (including configurational entropy always increases the break-even Fermi level for CdTe systems by $\ln(12)/2 = 1.24k_BT$, so it will always be significant).

Although we had difficulty identifying detailed experimental literature for the alloy system, there are several papers that look at As and P activation in pure CdTe, to which we can compare our results. With As doping, the reported maximum attainable hole concentrations range from 1×10^{17} cm^{-3}[98], 4×10^{16} cm^{-3}[99], 4×10^{16} cm^{-3}[100], 2×10^{16} cm^{-3}[101], and 2×10^{16} cm^{-3}[102].

For P doping, it ranges from 2×10^{17} cm^{-3}[98], 1.5×10^{17} cm^{-3}[103], and 6×10^{15} cm^{-3}[99]. In comparison, our simulations predict maximum hole concentrations at 300K in CdTe of 2.8×10^{17} cm^{-3} for As doping and 7.8×10^{18} cm^{-3} for P doping. Our value for As is on the high end but still reasonable compared to the experimental values. However, our value for P is significantly higher than any of the reported experimental values. Although our models predict that P dopants should sustain higher hole concentrations than As dopants, the publications that reported on both As and P doping in CdTe[98],[99] did not seem to identify noticeable differences between the maximum achievable doping with As compared to P. The presence of defect complexes (which we did not include in our models) may be reducing the activation of As and especially of P in these experimental systems, explaining why we generally find higher dopant activation than reported experimentally.

Computational studies have also calculated the migration barrier for conversion between the AX and symmetric tetrahedral structures, which we found to range from between 0.2 and 0.7 eV, depending on the SST ratio. Ref. [93] reports a value of 0.49 eV for conversion of symmetric As_{Te} into AX in CdTe, in line with our values. In contrast, Ref. [95] report that there is a "large energy barrier" between the symmetric and AX configurations in CdTe, which they report for the phosphorus P_{Te}^{+1} defect as being "less than 1 eV" (they find phosphorus and arsenic behave very similarly to each other in CdTe). Using these findings, they argue that a rapid quench from high temperature can freeze in a higher concentration of As_{Te}^{-1} than equilibrium allows, which is contrary to our assumption that even at room temperature As_{Te} will quickly reach an equilibrium distribution between As_{Te}^{-1} and As_{Te}^{+1}. However, we find that assuming an attempt frequency of 10^{13} Hz, even at room temperature and with a barrier as high as 1 eV, equilibration will occur in about 2 hours. This suggests that non-equilibrium *p*-type doping with As is likely unstable, and

our assumptions of fast equilibration are generally valid. Ref. [95] acknowledge this as a problem for the long-term stability of As as a *p*-type dopant. Both Refs. [95] and [94] find in computational studies that rapid quenching should significantly increase the hole density in As- and P-doped CdTe systems. However, because they both assumed that AX donor structures would not convert to symmetric acceptor structures and vice versa at room temperature (which as discussed above may not be the case), it is difficult to know whether these findings are valid. In contrast, Ref. [93] does not find a dependence of doping efficiency on cooling rate in their simulations, in line with our findings for CdTe.

There is some evidence from experiment that quenching does impact the hole concentration in CdTe, however. Ref. [104] finds that the doping efficiency of As in CdTe varies from 2% to 50% depending on the cooling rate. Ref. [96] reports that faster cooling gave an acceptor concentration two orders of magnitude greater than that produced by slower cooling. Ref. [105] observe a 5% activation of As dopants without quenching, compared to a 35%-80% activation of As dopants with quenching. However, they find this high activation efficiency decays to nearly the unquenched 5% value after only two weeks. If the AX centers are indeed the primary source of As self-compensation, this decay suggests a fairly low barrier to AX-symmetric conversion, generally in line with our findings.

While previous computational studies have investigated AX compensation in CdTe, this study has primarily focused on compensation in CdSeTe alloys. A key finding from our results is that increasing Se content should reduce the maximum obtainable hole concentration possible with As or P doping. The computational work by Ref. [106] suggests that the hole concentration is lower in CdSeTe compared to CdTe, which agrees with our findings. The results of experimental literature are mixed: some[107] suggest this is indeed the case, while others[108] find the opposite to be true.

Because of the paucity of studies on the behavior of the As and P AX structures in alloyed CdSeTe, this work represents an important contribution to the understanding of *p*-type doping limitations in the alloy system.

Chapter 8

ZnO: Surface Modeling

8.1 Introduction

Beyond our work on thin-film photovoltaics, we have also conducted some initial investigations into ZnO in conjunction with the UW MEM-C MRSEC program. ZnO possesses a wide band gap of 3.4 eV and a large exciton binding energy of 60 meV, making it a promising candidate material for UV light-emitters in lasers, LEDs, and other light-emitting devices[109]. It is also an emerging platform for qubits[110]. In collaboration with our experimental partners, we are particularly interested in the annealing of ZnO nanorods in an oxygen atmosphere, and the subsequent effects on defect states in the band gap. The ZnO nanorods of interest to us grow in a hexagonal wurtzite structure, elongated along the [0001] direction, with the large majority of the surface area occurring on the non-polar $[10\bar{1}0]$ sidewall faces. These faces, shown in Figure 8.1, will be the most likely adsorption sites for oxygen during annealing, so they will be the focus of our studies.

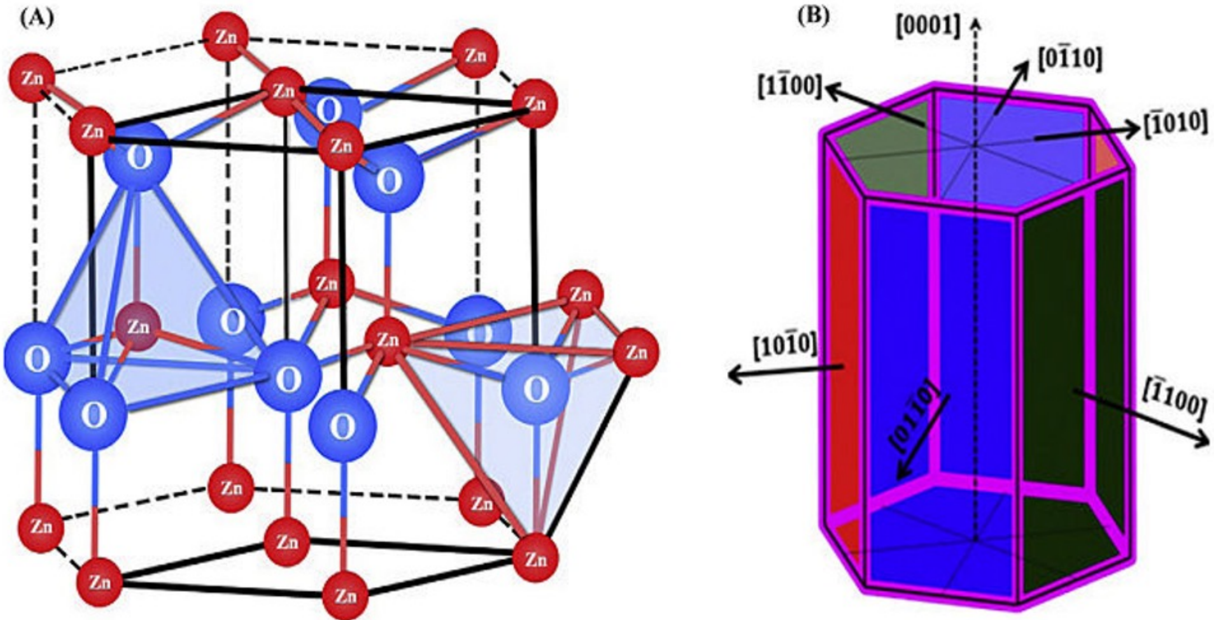

Figure 8.1: (a) ZnO wurtzite structure. (b) ZnO sidewall facets. Image reproduced from Ref. [111].

8.2 Bulk ZnO

Before we can model ZnO surfaces, we must establish a strong baseline in bulk ZnO using DFT. However, even for bulk ZnO there are several current challenges to the accurate modeling of the material. Both LDA and GGA functionals produce significantly underestimated band gaps (0.7-1.0 eV) compared with the experimental value (3.4 eV[112]). Semi-empirical DFT+U approaches have been employed that can correct the band gap, but at the cost of reductions in the lattice constant of up to 6%. Hybrid functionals can reproduce both the experimental band gap and lattice constants, but at a high computational cost[112].

Table 8.1 summarizes the properties of bulk ZnO reported in experimental and computational literature, along with the results of our work. As can be seen, our calculated band gap for GGA-PBE alone is far too small when compared with experimental values. We attempted to reproduce Ref. [114] using DFT+U, with $U_{Zn,d}$ = 10 eV and $U_{O,p}$ = 7 eV, but could not obtain the correct

Table 8.1: Summary of experimental and computational ZnO lattice constants and band gap from literature, compared with our work.

Experiment			**a** (Å)	**c** (Å)	**Band gap (eV)**
Ref. [112]			3.25	5.21	3.3
Ref. [113]			3.24	5.19	3.4
GGA-PBE			**a** (Å)	**c** (Å)	**Band gap (eV)**
This work			3.29	5.31	0.7
GGA-PBE+U	$\mathbf{U_{Zn,d}}$	$\mathbf{U_{O,p}}$	**a** (Å)	**c** (Å)	**Band gap (eV)**
Ref. [114]	10	7	3.05	4.91	3.4
This work	10	7	3.09	4.98	2.9
This work	10.75	10.5	3.05	4.91	3.4
This work	12.5	0	3.01	4.86	3.4
HSE	ω ($Å^{-1}$)	***a*** **(mix)**	**a** (Å)	**c** (Å)	**Band gap (eV)**
Ref. [115]	0.2	0.375	3.24	5.20	3.4
This work	0.2	0.375	3.25	5.21	3.4

band gap reported by them for these parameters. We found, however, that different combinations of the U parameters were able to reproduce the band gap. A sample of some of these combinations is shown in Table 8.1. The fact that very different combinations produced nearly identical results raises concerns about the justification for using one set of parameters over another.

Because of these concerns with the DFT+U method (along with the error in the lattice constants brought about by DFT+U), we turned to HSE hybrid functionals. Following Ref. [115], we successfully reproduced the experimental lattice constants and band gap with HSE, using a mixing parameter of $a = 0.375$. The density of states (DOS) from our HSE calculations is shown in Figure 8.2. The peak of the Zn 3d states is around -6.2 eV, compared to the experimental value of -7.5 eV[113]. Therefore, we conclude that the use of HSE is suitable for accurately modeling ZnO. To reduce the computational burden, we conducted compute-intensive explorations with faster GGA-PBE functionals, and final optimizations with HSE.

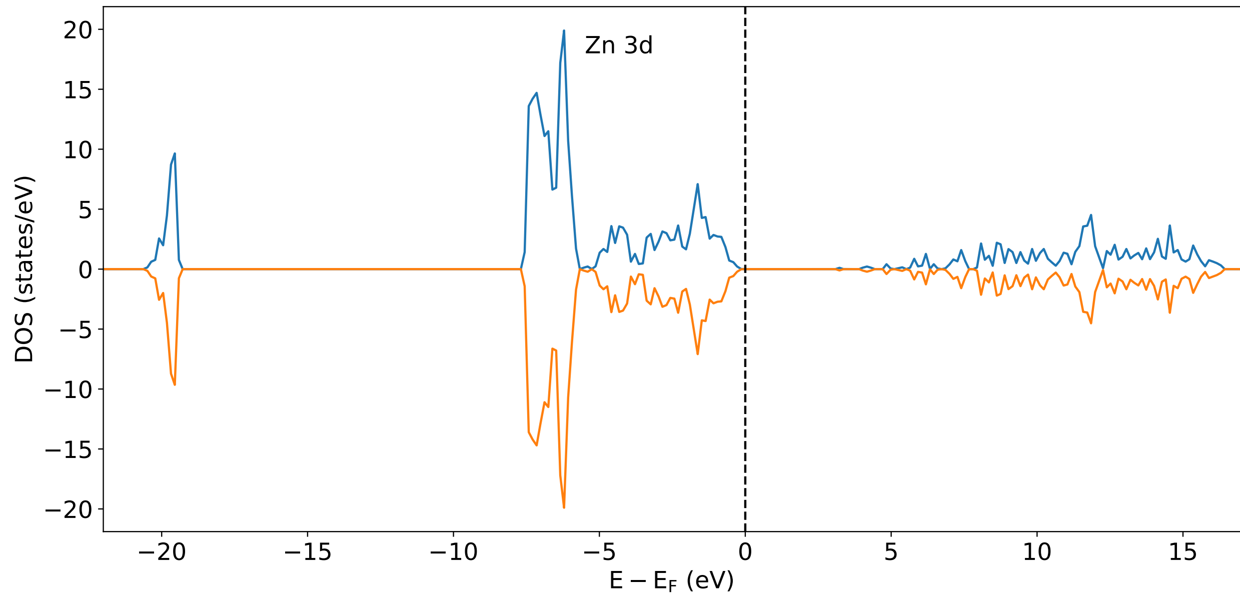

Figure 8.2: Density of states (showing both up and down spin states) of ZnO, calculated using HSE hybrid functionals. The vertical line indicates the Fermi level. The Zn 3d states are labeled.

8.3 $[10\bar{1}0]$ ZnO Surfaces

With a bulk ZnO baseline established, we turned to modeling the $[10\bar{1}0]$ non-polar surface. To simulate such a surface in DFT, we first created a large supercell of bulk ZnO. Then we removed all but 4 layers, as shown in Figure 8.3, so that there exists a large vacuum space extending 17 Å above the surface. To minimize interaction of the top surface with the periodic image of the bottom surface, pseudo-hydrogen atoms were added to the bottom surface to passivate the dangling bonds. Pseudo-H atoms with fractional charge of $\frac{3}{2}$ were added to Zn and pseudo-H atoms with fractional charge of $\frac{1}{2}$ were added to O. The top 2 surface layers were allowed to relax, while the remaining layers were frozen in their bulk positions. To find surface reconstructions, we initially used molecular dynamics (MD) to run simulated annealing, as described in Chapter 6.2. MD was run in the canonical (NVT) ensemble, using the Nose-Hoover thermostat to control the system temperature. The system was advanced with a 6 femtosecond time step for 1000 steps, starting at

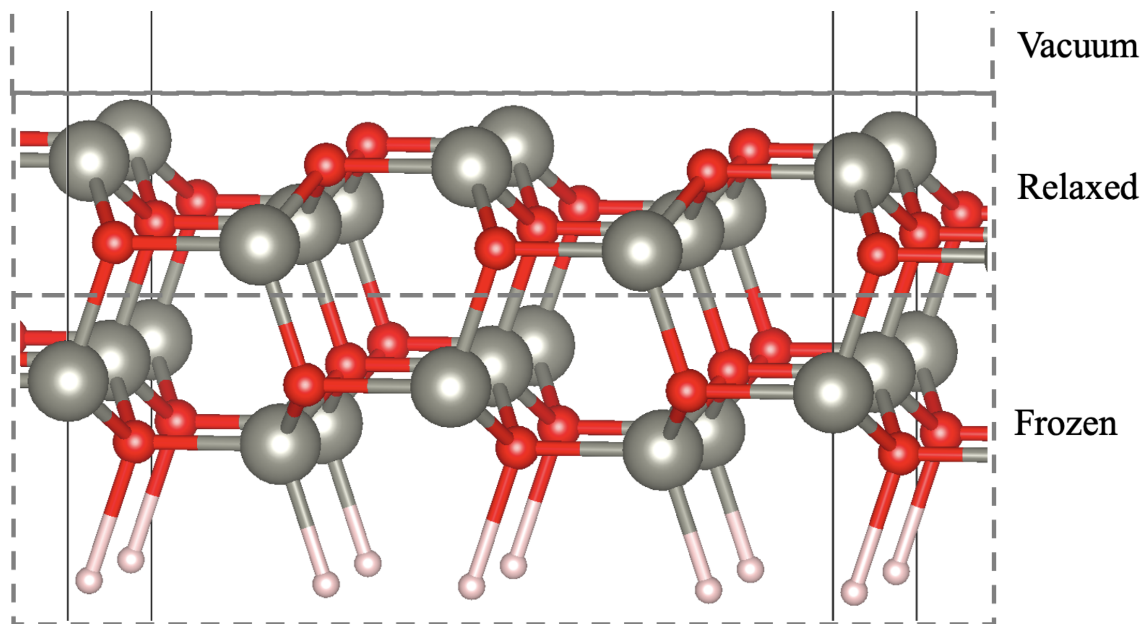

Figure 8.3: Side view of the bare unrelaxed ZnO $[10\bar{1}0]$ surface. The layers that are frozen, the layers that are allowed to relax, and the vacuum space are labeled. Zn is gray, O is red.

Table 8.2: Bond lengths (Å) corresponding to the labeled bonds in Figure 8.4. The columns (a), (b), and (c) correspond to the bare unreconstructed surface, the bare reconstructed surface, and the reconstructed surface with an adsorbed O atom, as in Figure 8.4.

Bond Label	(a)	(b)	(c)
1	1.98	1.85	2.05
2	1.97	1.91	2.01
3	1.97	1.98	1.91
4		1.91	1.89

600K and ending at 1K. MD was run using PBE-GGA functionals for speed, but with the frozen layers fixed at their optimal bulk positions as determined by HSE calculations. At the end, the final structures were relaxed using the full HSE functionals. In addition to studying the bare surface, we also ran simulations with 1-2 additional O atoms added to the surface, and 1-2 O atoms removed from the surface.

The results of a representative sample of these MD runs followed by HSE relaxations are shown in Figure 8.4, with the corresponding bond lengths of the labeled atoms in Figure 8.4 given in Table 8.2. When the bare surface relaxes, the top Zn atoms contract downwards, being pulled 0.26

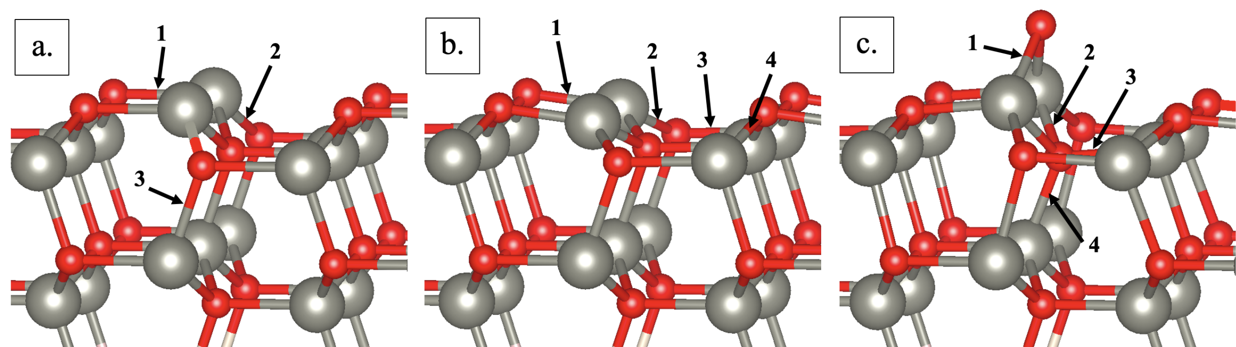

Figure 8.4: Surface reconstructions of the ZnO $[10\bar{1}0]$ surface. (a) the bare unreconstructed surface. (b) the bare reconstructed surface. (c) the reconstructed surface with an adsorbed O atom. The labels correspond to the bond lengths given in Table 8.2

Å closer to the bulk, as shown in Figure 8.4b. The surface Zn-O bonds (labeled 1b) contract from 1.98 Å to 1.85 Å, a contraction of 0.14 Å. Ref. [116], in their computational study of the same ZnO surface, report that the surface Zn atoms move downwards 0.22 Å, with the surface Zn-O bonds contracting 0.15 Å, in agreement with our results. Likewise, Ref. [117] find that the surface Zn atoms move downwards by 0.27 Å, also closely matching our values. The other bonds in the bare reconstructed surface contract slightly, but much less than the surface Zn-O bonds, which has also been reported by Ref. [116]. When an O is added to the surface (Figure 8.4c), it relaxes to a position halfway between two surface Zn atoms, with a bond distance (labeled 1c) of 2.05 Å, slightly larger than the bulk Zn-O bond distance. The adsorbed O displaces the O immediately beneath it, shifting that bulk O downwards 0.14 Å from its position in Figure 8.4b.

Figure 8.5 plots the DOS for the bare surface, surfaces with 1-2 O atoms added, and surfaces with 1-2 O atoms removed, referenced to the valence band maximum (VBM). For (a) and (b) the Fermi level is at about 1.4 eV relative to the VBM, while for (c), (d), and (e) the Fermi level is at

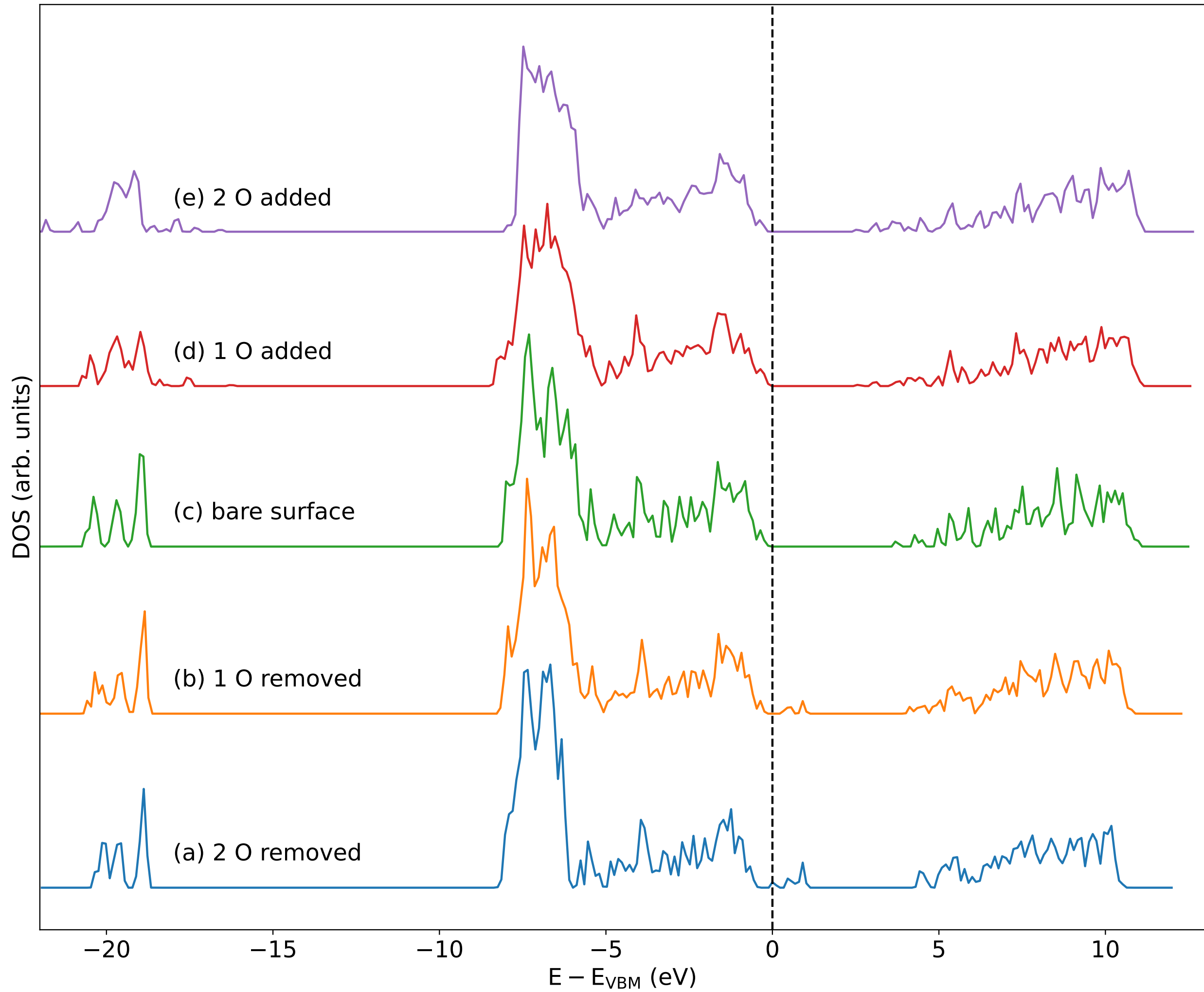

Figure 8.5: Density of states of ZnO, for surfaces with (a) 2 O atoms removed, (b) 1 O atom removed, (c) the bare $[10\bar{1}0]$ surface, (d) 1 O atom added, and (e) 2 O atoms added. The vertical line indicates the valence band maximum (VBM).

about 0.3 eV relative to the VBM. Consequently, as with the bulk ZnO in Figure 8.2, all valence band states are filled, while all conduction band states are empty. For the surfaces with additional O atoms, we observed that there are unfilled states introduced below the conduction band within the band gap. Meanwhile, for the surfaces with O atoms removed, we observed that there are filled states introduced above the valence band within the band gap. These states move the Fermi level up about 1.1 eV. Ref. [117] also reports additional filled states above the valence band when

removing an O atom from the same ZnO surface. Such states may function as a reservoir for less energetic photons, helping to excite them to the conduction band[117]. Our results suggest that the addition or subtraction of O from the $[10\bar{1}0]$ surface of ZnO (corresponding to annealing in an O atmosphere) will not introduce or remove any substantial surface charges, as for varying degrees of O coverage the valence band states are always filled and the conduction band states are always empty. However, heavily *p*- or *n*-doped material may have substantial surface charges, if the states near the top of the band gap become filled, or the states near the bottom of the band gap become emptied.

Chapter 9

Conclusions, Reflections, and Future Work

In this work I have presented several KLMC models of different systems relevant to thin-film PV technology. I have demonstrated a model for the diffusivity of In and Ga in CIGS, an important contribution that will be useful in understanding and controlling In/Ga interdiffusion and Ga grading in CIGS. This model can be integrated into continuum simulations of CIGS, and it has been shown to reproduce experimental diffusivity very closely. Additionally, I have built a model that captures the interactions of In and Ga on the III-sublattice with vacancies and antisites on the Cu-sublattice, which was used to predict both group-III and Cu-vacancy ordering, which in turn was used to model the band gap fluctuations that arise in the Cu-deficient CIGS used in high performance solar cells. I have built a model to simulate the passivation of Cu_{In} deep level traps by In_{Cu} in CIS, a process that is critical to understanding and improving device performance. This model predicts passivation timescales that are far longer than those obtained in experiment, potentially suggesting other mechanisms are at play and should be investigated. I have developed simple models for the diffusivity of intrinsic defects in CdSeTe, which can also be applied to continuum simulations. I have shown how self-compensating AX structure formation for As and P dopants

in CdSeTe limits *p*-type doping. I have found that in the absence of complex formation, P should allow for better *p*-type doping than As, and that rapid quenching from high temperature during processing may improve *p*-type doping. Additionally, by including Se interactions (which has not previously, to my knowledge, been attempted by other groups) I have demonstrated that increasing Se content will make *p*-type doping more difficult. I have reproduced the bulk properties of ZnO with HSE hybrid functionals, and used them to model $[10\bar{1}0]$ surfaces with varying levels of oxygen coverage, finding that oxygen annealing is unlikely to introduce or remove surface charges in undoped ZnO.

In addition to specific findings related to these materials, I believe that my work has contributed to advancing KLMC methodology. In general, I have found there to be a limited number of publications that engage with the type of KLMC methods I utilize here for the types of compound semiconductor alloys that I have looked at. In general, most publications involving Monte Carlo methods in this area that I have identified use the Metropolis-Hastings class of algorithms, which do not include kinetics and focus only on arriving at the equilibrium state of a material. Often when these thin-film materials are processed in real life, rapid quenching occurs such that non-equilibrium, kinetically limited structures become frozen in at room temperature. As a result, incorporation of kinetics is necessary to properly reproduce and understand the formation of these structures, and KLMC is needed. By demonstrating a KLMC approach to diffusion in CIGS that is validated against experiment, this work may help future investigators in applying these techniques to other systems of interest. In addition to models of diffusion, I have demonstrated creative ways to utilize KLMC (or in some cases simply Metropolis-Hastings MC) to understand the behavior of performance-limiting defects in the materials studied, such as the kinetics of the passivation of detrimental trap states or the self-compensation of dopants. These approaches hopefully will

demonstrate the versatility of the MC method to solve a wide variety of problems, and serve as inspiration for others. I have also found there to be a limited amount of modeling work done in the alloy regime of these thin-film systems, so by working in this regime (as opposed to simply studying the extrema, e.g. CIS and CGS) I have advanced methods for dealing with these types of alloys that can be translated over to any number of similar alloy systems.

It is hard to overstate how much I have learned over the course of this PhD. One key area that I have grown in is understanding both the power and the limitations of computational modeling methods. I have discovered that it can often be relatively straightforward to run a large number of calculations and set up some initial model, but that it is much harder to actually ensure that the model represents reality correctly. When I began my studies here, I initially treated tools such as VASP as simply producing the “correct answer” right off the bat, and only over time did I learn how calculations such as in VASP need to be tweaked and carefully validated to confirm proper results. Examples include the proper treatment of the errors that originate from the presence of charged defects in periodic cells, or handling the often incorrect estimations of the band gap produced by standard DFT methods. For both of these there exists a variety of proposed solutions with no “one-size-fits-all” approach, and a good physical intuition of the system is needed. Often many groups will publish results that disagree significantly on a single parameter, such as the formation energies of the AX structures of As and P in CdTe, where a half dozen papers differed substantially on this one point. Differences in the treatment of spin-orbit coupling or the localization of charge were found to have large impacts, illustrating the difficulty of even a relatively “straightforward” calculation.

I found hierarchical modeling to be especially difficult in this regards, as even slight errors in the foundational levels of the model will propagate upwards and compound, increasing the risk that

the higher-level model becomes decoupled from reality. Consider that for my model of In and Ga diffusion in CIGS to be accurate, I needed to identify the correct diffusion-limiting defects, obtain reliable estimates of defect concentrations, accurate defect binding energies, accurate defect migration barriers, accurate hopping attempt frequencies, and properly combine all these into a complex KLMC model. Furthermore, experimental results may be significantly impacted by more complex factors such as the presence of grain boundaries and extrinsic impurities such as Na, making experimental validation even more challenging. Failing to identify a critical rate-limiting process can mean that even an accurate model may be irrelevant to explaining experimental observations.

Going forward, one way to address this problem could be by identifying ways to break up larger projects into smaller parts, where each part independently provides valuable contributions. An example might be the work I have done on In/Ga ordering in CIGS. Here, KLMC can produce the structures to be fed into a model that predicts the impact that local variations in In/Ga concentration have on the band gap and ultimately on device performance. However, a smaller standalone project could involve initially testing a range of realistic structures (generated apart from KLMC) on the model to understand how the magnitude of In/Ga clustering impacts device performance, which is valuable in itself even if the KLMC models ultimately prove to be inaccurate. Additionally, I think collaborations between computational and experimental groups (such as we see with the UW MEM-C MRSEC) are extremely important to the success of computational modeling work. They allow for a back-and-forth, where computational results can guide experiment, which in turn can guide computation, and this process will hopefully ensure that the computational models remain in touch with experimental reality. Lastly, I am excited for how future developments in computing power and artificial intelligence (AI) may increase the usefulness of computational models. AI has the potential to accelerate workflows, automate the setup of runs, help with processing data, and

more. Increases in computing power will simply allow for more brute force, such as larger and longer simulations. In doing so, it may be possible to cut out various simplifying assumptions that introduce error. All in all, it is an exciting time for the field of computational materials modeling.

Acknowledgments

This work was supported in part by the U.S. Department of Energy's Office of Energy Efficiency and Renewable Energy (EERE) under the Solar Energy Technology Office Award Number DE-EE0008556. This work was facilitated through the use of the Hyak supercomputer system at the University of Washington, funded by the UW Student Technology Fee. This work was partially supported by the U.S. National Science Foundation through the University of Washington Molecular Engineering Materials Center, a Materials Research Science and Engineering Center (DMR-2308979).

Bibliography

[1] Fraunhofer Institute for Solar Energy Systems. "Photovoltaics Report." (2024), [Online]. Available: `https://www.ise.fraunhofer.de/content/dam/ise/de/documents/publications/studies/Photovoltaics-Report.pdf` (visited on 07/17/2024).

[2] D. Colombara, F. Werner, T. Schwarz, *et al.*, "Sodium enhances indium-gallium interdiffusion in copper indium gallium diselenide photovoltaic absorbers," *Nature Communications*, vol. 9, no. 826, 2018.

[3] D. J. Schroeder, G. D. Berry, and A. A. Rockett, "Gallium diffusion and diffusivity in $CuInSe_2$ epitaxial layers," *Applied Physics Letters*, vol. 69, no. 26, pp. 4068–4070, 1996.

[4] T. Beckers, L. Nagarajan, and M. Martin, "Radiotracer diffusion of 114m In in $Cu(In,Ga)Se_2$ thin films," *Thin Solid Films*, vol. 592, pp. 118–123, 2015.

[5] D. E. Sommer and S. T. Dunham, "Understanding copper diffusion in $CuInSe_2$ with first-principles based atomistic and continuum models," *Journal of Applied Physics*, vol. 130, no. 23, p. 235 701, 2021.

[6] O. Lundberg, J. Lu, A. Rockett, M. Edoff, and L. Stolt, "Diffusion of indium and gallium in $Cu(In,Ga)Se_2$ thin film solar cells," *J Phys Chem Solids*, vol. 64, pp. 1499–1504, 2003.

[7] W. Witte, D. Abou-Ras, K. Albe, *et al.*, "Gallium gradients in Cu(In,Ga)Se_2 thin-film solar cells," *Progress in Photovoltaics: Research and Applications*, vol. 23, no. 6, pp. 717–733, 2015.

[8] X. Xiang, D. E. Sommer, A. Gehrke, and S. T. Dunham, "Coupled process/device modeling and point defect engineering of Cu(In,Ga)Se_2 solar cells," *IEEE Journal of Photovoltaics*, vol. 14, no. 3, pp. 422–432, 2024.

[9] M.-H. Du, H. Takenaka, and D. J. Singh, "Native defects and oxygen and hydrogen-related defect complexes in CdTe: Density functional calculations," *Journal of Applied Physics*, vol. 104, no. 9, p. 093 521, 2008.

[10] E. D. Jones and N. M. Stewart, "Self-diffusion of cadmium telluride," *Journal of Crystal Growth*, vol. 84, no. 2, pp. 289–294, 1987.

[11] J.-H. Yang, J.-S. Park, J. Kang, and S.-H. Wei, "First-principles multiple-barrier diffusion theory: The case study of interstitial diffusion in CdTe," *Phys. Rev. B*, vol. 91, no. 7, p. 075 202, 2015.

[12] P. M. Borsenberger and D. A. Stevenson, "Self-diffusion of cadmium and tellurium in cadmium telluride," *Journal of Physics and Chemistry of Solids*, vol. 29, no. 8, pp. 1277–1286, 1968.

[13] J. Ma, J. Yang, S.-H. Wei, and J. L. F. Da Silva, "Correlation between the electronic structures and diffusion paths of interstitial defects in semiconductors: The case of CdTe," *Phys. Rev. B*, vol. 90, no. 15, p. 155 208, 2014.

[14] Solar Energy Technologies Office. "Cadmium telluride." (2022), [Online]. Available: `https://www.energy.gov/eere/solar/cadmium-telluride` (visited on 11/21/2022).

[15] E. Menéndez-Proupin, M. Casanova-Páez, A. L. Montero-Alejo, M. A. Flores, and W. Orellana, “Symmetry and thermodynamics of tellurium vacancies in cadmium telluride,” *Physica B: Condensed Matter*, vol. 568, pp. 81–87, 2019.

[16] M. A. Berding, “Native defects in CdTe,” *Phys. Rev. B*, vol. 60, no. 12, pp. 8943–8950, 1999.

[17] I. Sankin and D. Krasikov, “Kinetic simulations of Cu doping in chlorinated CdSeTe PV absorbers,” *Phys. Status Solidi A*, vol. 216, no. 15, p. 1 800 887, 2019.

[18] H. Wolf, F. Wagner, and T. Wichert, “Anomalous diffusion profiles of Ag in CdTe due to chemical self-diffusion,” *Phys. Rev. Lett.*, vol. 94, no. 12, p. 125 901, 2005.

[19] M. A. Scarpulla, B. McCandless, A. B. Phillips, *et al.*, “CdTe-based thin film photovoltaics: Recent advances, current challenges and future prospects,” *Solar Energy Materials and Solar Cells*, vol. 255, p. 112 289, 2023.

[20] M. Mantina, Y. Wang, R. Arroyave, L. Q. Chen, Z. K. Liu, and C. Wolverton, “First-principles calculation of self-diffusion coefficients,” *Phys. Rev. Lett.*, vol. 100, no. 21, p. 215 901, 2008.

[21] P. Hatton. “Gas bubbles and atomic diffusion mechanisms in CdTe solar cells.” (2021), [Online]. Available: `https://repository.lboro.ac.uk/articles/thesis/Gas_bubbles_and_atomic_diffusion_mechanisms_in_CdTe_solar_cells/13677880` (visited on 11/21/2022).

[22] N. M. Harrison. “An introduction to density functional theory.” (2001), [Online]. Available: `https://www.imperial.ac.uk/media/imperial-college/research-`

centres-and-groups/computational-materials-science/teaching/DFT_NATO.pdf (visited on 11/21/2022).

[23] P. Hohenberg and W. Kohn, "Inhomogeneous electron gas," *Phys. Rev.*, vol. 136, no. 0, B864–B871, 1964.

[24] W. Kohn and L. J. Sham, "Self-consistent equations including exchange and correlation effects," *Phys. Rev.*, vol. 140, no. 4A, A1133–A1138, 1965.

[25] K. F. Garrity, J. W. Bennett, K. M. Rabe, and D. Vanderbilt, "Pseudopotentials for high-throughput DFT calculations," *Computational Materials Science*, vol. 81, pp. 446–452, 2014.

[26] D. Sheppard, R. Terrell, P. Xiao, and J. Duncan. "Saddle point finding methods." (), [Online]. Available: https://theory.cm.utexas.edu/henkelman/research/saddle/ (visited on 11/21/2022).

[27] G. Henkelman and H. Jónsson, "Improved tangent estimate in the nudged elastic band method for finding minimum energy paths and saddle points," *The Journal of Chemical Physics*, vol. 113, no. 22, pp. 9978–9985, 2000.

[28] H. Jónsson, G. Mills, and K. W. Jacobsen, "Nudged elastic band method for finding minimum energy paths of transitions," in *Classical and Quantum Dynamics in Condensed Phase Simulations*. World Scientific, 1998, pp. 385–404.

[29] G. Henkelman, B. P. Uberuaga, and H. Jónsson, "A climbing image nudged elastic band method for finding saddle points and minimum energy paths," *The Journal of Chemical Physics*, vol. 113, no. 22, pp. 9901–9904, 2000.

[30] G. Henkelman and H. Jónsson, "A dimer method for finding saddle points on high dimensional potential surfaces using only first derivatives," *The Journal of Chemical Physics*, vol. 111, no. 15, pp. 7010–7022, 1999.

[31] M. Gajdos, K. Hummer, G. Kresse, J. Furthmüller, and F. Bechstedt, "Linear optical properties in the projector-augmented wave methodology," *Phys. Rev. B*, vol. 73, no. 4, p. 045 112, 2006.

[32] D. Mutter and S. T. Dunham, "Calculation of defect concentrations and phase stability in Cu_2ZnSnS_4 and $Cu_2ZnSnSe_4$ from stoichiometry," *IEEE Journal of Photovoltaics*, vol. 5, no. 4, pp. 1188–1196, 2015.

[33] D. Sommer. "PYCCT (python compositionally constrained thermodynamics)." (2022), [Online]. Available: `https://github.com/dsom55/pycct` (visited on 11/21/2022).

[34] M. Leetmaa and N. V. Skorodumova, "KMCLib: A general framework for lattice kinetic monte carlo (KMC) simulations," *Computer Physics Communications*, vol. 185, no. 9, pp. 2340–2349, 2014.

[35] A. S. Gehrke, D. E. Sommer, and S. T. Dunham, "Atomistic models of In and Ga diffusion in Cu(In,Ga)Se_2," *Journal of Applied Physics*, vol. 134, no. 11, p. 115 002, 2023.

[36] M. Marudachalam, R. Birkmire, H. Hichri, J. Schultz, A. Swartzlander, and M. Al-Jassim, "Phases, morphology, and diffusion in $CuIn_xGa_{1-x}Se_2$ thin films," *Journal of Applied Physics*, vol. 82, no. 6, pp. 2896–2905, 1997.

[37] L. E. Oikkonen, M. G. Ganchenkova, A. P. Seitsonen, and R. M. Nieminen, "Formation, migration, and clustering of point defects in $CuInSe_2$ from first principles," *Journal of Physics: Condensed Matter*, vol. 26, no. 34, p. 345 501, 2014.

[38] M. Malitckaya, H.-P. Komsa, V. Havu, and M. J. Puska, "First-principles modeling of point defects and complexes in thin-film solar-cell absorber $CuInSe_2$," *Advanced Electronic Materials*, vol. 3, no. 6, p. 1 600 353, 2017.

[39] C. Persson, Y.-J. Zhao, S. Lany, and A. Zunger, "*n*-type doping of $CuInSe_2$ and $CuGaSe_2$," *Phys. Rev. B*, vol. 72, no. 3, p. 035 211, 2005.

[40] J. Pohl and K. Albe, "Intrinsic point defects in $CuInSe_2$ and $CuGaSe_2$ as seen via screened-exchange hybrid density functional theory," *Physical Review B*, vol. 87, no. 24, p. 245 203, 2013.

[41] G. Kresse and J. Furthmüller, "Efficient iterative schemes for ab initio total-energy calculations using a plane-wave basis set," *Physical Review B*, vol. 54, no. 16, p. 11 169, 1996.

[42] J. P. Perdew, K. Burke, and M. Ernzerhof, "Generalized gradient approximation made simple," *Phys. Rev. Lett.*, vol. 77, no. 18, pp. 3865–3868, 1996.

[43] J. Heyd, G. E. Scuseria, and M. Ernzerhof, "Hybrid functionals based on a screened coulomb potential," *The Journal of Chemical Physics*, vol. 118, no. 18, pp. 8207–8215, 2003.

[44] W. Paszkowicz, R. Lewandowska, and R. Bacewicz, "Rietveld refinement for $CuInSe_2$ and $CuIn_3Se_5$," *Journal of Alloys and Compounds*, vol. 362, no. 1, pp. 241–247, 2004.

[45] L. Shay and J. Wernick, *Ternary Chalcopyrite Semiconductors*. Pergamon Press, 1975.

[46] D. Colombara, K. Conley, M. Malitckaya, H.-P. Komsa, and M. J. Puska, "The fox and the hound: In-depth and in-grain Na doping and Ga grading in $Cu(In,Ga)Se_2$ solar cells," *J. Mater. Chem. A*, vol. 8, no. 14, pp. 6471–6479, 2020.

[47] S. P. Ong, W. D. Richards, A. Jain, *et al.*, "Python Materials Genomics (pymatgen): A robust, open-source python library for materials analysis," *Computational Materials Science*, vol. 68, pp. 314–319, 2013.

[48] P. Ágoston, C. Körber, A. Klein, M. J. Puska, R. M. Nieminen, and K. Albe, "Limits for n-type doping in In_2O_3 and SnO_2: A theoretical approach by first-principles calculations using hybrid-functional methodology," *Journal of Applied Physics*, vol. 108, no. 5, p. 053 511, 2010.

[49] M. V. Yakushev, F. Luckert, C. Faugeras, A. V. Karotki, A. V. Mudryi, and R. W. Martin, "Excited states of the free excitons in $CuInSe_2$ single crystals," *Applied Physics Letters*, vol. 97, no. 15, p. 152 110, 2010.

[50] P. W. Li, R. A. Anderson, and R. H. Plovnick, "Dielectric constant of $CuInSe_2$ by capacitance measurements," *Journal of Physics and Chemistry of Solids*, vol. 40, no. 4, pp. 333–334, 1979.

[51] S. Ishizuka, N. Taguchi, J. Nishinaga, Y. Kamikawa, and H. Shibata, "A comparative study of the effects of light and heavy alkali-halide postdeposition treatment on $CuGaSe_2$ and $Cu(In,Ga)Se_2$ thin-film solar cells," *Solar Energy*, vol. 211, pp. 1092–1101, 2020.

[52] A. Bauknecht, S. Siebentritt, J. Albert, Y. Tomm, and M. C. Lux-Steiner, "Excitonic photoluminescence from $CuGaSe_2$ single crystals and epitaxial layers: Temperature dependence of the band gap energy," *Japanese Journal of Applied Physics*, vol. 39, no. S1, p. 322, 2000.

[53] D. L. Young, J. Keane, A. Duda, *et al.*, "Improved performance in $ZnO/CdS/CuGaSe_2$ thin-film solar cells," *Progress in Photovoltaics: Research and Applications*, vol. 11, no. 8, pp. 535–541, 2003.

[54] H. Metzner, A. Dietz, M. Gossla, *et al.*, "Admittance spectroscopy of polycrystalline and epitaxially grown $CuGaSe_2$," *Journal of Physics and Chemistry of Solids*, vol. 66, no. 11, pp. 1940–1943, 2005.

[55] M. Pippig and F. Mercuri, "Efficient evaluation of coulomb interactions in kinetic Monte Carlo simulations of charge transport," *The Journal of Chemical Physics*, vol. 152, no. 16, p. 164 102, 2020.

[56] C. W. M. Castleton, A. Höglund, and S. Mirbt, "Density functional theory calculations of defect energies using supercells," *Modelling and Simulation in Materials Science and Engineering*, vol. 17, no. 8, p. 084 003, 2009.

[57] H.-P. Komsa, T. T. Rantala, and A. Pasquarello, "Finite-size supercell correction schemes for charged defect calculations," *Phys. Rev. B*, vol. 86, no. 4, p. 045 112, 2012.

[58] S. Lany and A. Zunger, "Assessment of correction methods for the band-gap problem and for finite-size effects in supercell defect calculations: Case studies for ZnO and GaAs," *Phys. Rev. B*, vol. 78, no. 23, p. 235 104, 2008.

[59] C. Freysoldt, J. Neugebauer, and C. G. Van de Walle, "Fully ab initio finite-size corrections for charged-defect supercell calculations," *Phys. Rev. Lett.*, vol. 102, no. 1, p. 016 402, 2009.

[60] J. Pohl and K. Albe, "Thermodynamics and kinetics of the copper vacancy in $CuInSe_2$, $CuGaSe_2$, $CuInS_2$, and $CuGaS_2$ from screened-exchange hybrid density functional theory," *Journal of Applied Physics*, vol. 108, no. 2, p. 023 509, 2010.

[61] R. Forest, B. McCandless, X. He, *et al.*, "Diffusion of sodium in single crystal $CuInSe_2$," *Journal of Applied Physics*, vol. 121, no. 24, p. 245 102, 2017.

[62] R. Saniz, J. Bekaert, B. Partoens, and D. Lamoen, “Structural and electronic properties of defects at grain boundaries in $CuInSe_2$,” *Phys. Chem. Chem. Phys.*, vol. 19, no. 22, pp. 14 770–14 780, 2017.

[63] R. Saniz, J. Bekaert, B. Partoens, and D. Lamoen, “First-principles study of defects at Σ3 grain boundaries in $CuGaSe_2$,” *Solid State Communications*, vol. 330, p. 114 263, 2021.

[64] N. J. Herrmann, D. Sommer, Y. Jin, D. Mutter, and S. T. Dunham, “Monte Carlo modeling of phase separation in $CuIn_xGa_{1-x}Se_2$,” in *2016 IEEE 43rd Photovoltaic Specialists Conference (PVSC)*, 2016, pp. 2174–2177.

[65] C. D. R. Ludwig, T. Gruhn, C. Felser, T. Schilling, J. Windeln, and P. Kratzer, “Indium-gallium segregation in $CuIn_xGa_{1-x}Se_2$: An ab initio–based Monte Carlo study,” *Phys. Rev. Lett.*, vol. 105, no. 2, p. 025 702, 2010.

[66] H. Xue, F. Tang, F. Zhang, W. Lu, and Y. Feng, “Temperature effects on distribution and inhomogeneous degree of In–Ga atoms in $CuIn_{1-x}Ga_xSe_2$ alloys,” *Materials Letters*, vol. 164, pp. 169–171, 2016.

[67] S. T. Dunham and C. D. Wu, “Atomistic models of vacancy-mediated diffusion in silicon,” *Journal of Applied Physics*, vol. 78, no. 4, pp. 2362–2366, 1995.

[68] Wolfram Research, Inc., *Mathematica, Version 12.0*, Champaign, IL, 2019. [Online]. Available: `https://www.wolfram.com/mathematica`.

[69] G. Voorwinden, R. Kniese, P. Jackson, and M. Powalla, “In-line $Cu(In,Ga)Se_2$ co-evaporation process on 30 cm x 30 cm substrates with multiple deposition stages,” in *Proceedings of the 22nd European Photovoltaic Solar Energy Conference*, 2007, pp. 2115–2118.

[70] J. Bastek, N. A. Stolwijk, R. Wuerz, A. Eicke, J. Albert, and S. Sadewasser, "Zinc diffusion in polycrystalline Cu(In,Ga)Se_2 and single-crystal $CuInSe_2$ layers," *Applied Physics Letters*, vol. 101, no. 7, p. 074 105, 2012.

[71] K. Hiepko, J. Bastek, R. Schlesiger, G. Schmitz, R. Wuerz, and N. A. Stolwijk, "Diffusion and incorporation of Cd in solar-grade Cu(In,Ga)Se_2 layers," *Applied Physics Letters*, vol. 99, no. 23, p. 234 101, 2011.

[72] A. Koprek, P. Zabierowski, M. Pawlowski, *et al.*, "Effect of Cd diffusion on the electrical properties of the Cu(In,Ga)Se_2 thin-film solar cell," *Solar Energy Materials and Solar Cells*, vol. 224, p. 110 989, 2021.

[73] W. Witte, D. Abou-Ras, and D. Hariskos, "Chemical bath deposition of Zn(O,S) and CdS buffers: Influence of Cu(In,Ga)Se_2 grain orientation," *Applied Physics Letters*, vol. 102, no. 5, p. 051 607, 2013.

[74] K. Djessas, S. Yapi, G. Massé, M. Ibannain, and J. L. Gauffier, "Diffusion of Cu, In, and Ga in In_2Se_3/$CuGaSe_2$/SnO_2 thin film photovoltaic structures," *Journal of Applied Physics*, vol. 95, no. 8, pp. 4111–4116, 2004.

[75] J. Wang, Y. F. Zhang, and J. Zhu, "Diffusion coefficients of selenium and gallium during the $Cu(In_{1-x}Ga_x)Se_2$ thin films preparation process," *Advanced Materials Research*, vol. 815, pp. 448–453, 2013.

[76] B. Namnuan, K. Yoodee, and S. Chatraphorn, "Probing diffusion of In and Ga in $CuInSe_2$/$CuGaSe_2$ bilayer thin films by x-ray diffraction," *Journal of Crystal Growth*, vol. 432, pp. 24–32, 2015.

[77] A. Stokes, M. Al-Jassim, A. Norman, D. Diercks, and B. Gorman, “Nanoscale insight into the p-n junction of alkali-incorporated Cu(In,Ga)Se_2 solar cells,” *Progress in Photovoltaics: Research and Applications*, vol. 25, no. 9, pp. 764–772, 2017.

[78] T. Wada, “$CuInSe_2$ and related I–III–VI_2 chalcopyrite compounds for photovoltaic application,” *Japanese Journal of Applied Physics*, vol. 60, no. 8, p. 080 101, 2021.

[79] S. B. Zhang, S.-H. Wei, A. Zunger, and H. Katayama-Yoshida, “Defect physics of the $CuInSe_2$ chalcopyrite semiconductor,” *Phys. Rev. B*, vol. 57, no. 16, pp. 9642–9656, 1998.

[80] J. Mattheis, U. Rau, and J. H. Werner, “Light absorption and emission in semiconductors with band gap fluctuations—a study on Cu(In,Ga)Se_2 thin films,” *Journal of Applied Physics*, vol. 101, no. 11, p. 113 519, 2007.

[81] M. R. Roussel. “Foundations of chemical kinetics lecture 28: Diffusion-influenced reactions.” (2021), [Online]. Available: `https://people.uleth.ca/~roussel/C4000foundations/slides/18diffusion_influenced.pdf` (visited on 11/23/2021).

[82] H. H. Woodbury and R. B. Hall, “Diffusion of the chalcogens in the II-VI compounds,” *Phys. Rev.*, vol. 157, no. 3, pp. 641–655, 1967.

[83] S. S. Chern and F. A. Kroger, “The defect structure of CdTe: Self-diffusion data,” *Journal of Solid State Chemistry*, vol. 14, no. 1, pp. 44–51, 1975.

[84] M. G. Astles and G. Blackmore, “The use of secondary ion mass spectrometry in the study of matrix atom diffusion in epitaxial CdTe,” *Journal of Electronic Materials*, vol. 15, no. 5, pp. 287–290, 1986.

[85] E. D. Jones, N. M. Stewart, and J. B. Mullin, "Studies on the self-diffusion of cadmium in cadmium telluride in the temperature range 350–650°C using anodic oxidation," *Journal of Crystal Growth*, vol. 130, no. 1, pp. 6–12, 1993.

[86] M. U. Ahmed, E. D. Jones, and N. M. Stewart, "Cd self-diffusion in Cu doped CdTe," *Journal of Crystal Growth*, vol. 160, no. 1, pp. 36–40, 1996.

[87] R. Kanno, T. Wada, Y. Yamazaki, J. Wang, M. Isshiki, and Y. Iijima, "Self-diffusion of cadmium in cadmium telluride annealed in tellurium-saturated atmosphere," *Materials Science in Semiconductor Processing*, vol. 6, no. 5, pp. 319–322, 2003.

[88] F. A. Kröger, "The defect structure of CdTe," *Rev. Phys. Appl.*, vol. 12, no. 2, pp. 205–210, 1977.

[89] A. Carvalho, A. K. Tagantsev, S. Oberg, P. R. Briddon, and N. Setter, "Cation-site intrinsic defects in Zn-doped CdTe," *Phys. Rev. B*, vol. 81, no. 7, p. 075 215, 2010.

[90] C.-H. Su, "Energy band gap, intrinsic carrier concentration, and fermi level of CdTe bulk crystal between 304 and 1067K," *Journal of Applied Physics*, vol. 103, no. 8, p. 084 903, 2008.

[91] I. Chatratin, B. Dou, S.-H. Wei, and A. Janotti, "Doping limits of phosphorus, arsenic, and antimony in CdTe," *The Journal of Physical Chemistry Letters*, vol. 14, no. 1, pp. 273–278, 2023.

[92] S.-H. Wei and S. B. Zhang, "Chemical trends of defect formation and doping limit in II-VI semiconductors: The case of CdTe," *Phys. Rev. B*, vol. 66, no. 15, p. 155 211, 2002.

[93] D. Krasikov and I. Sankin, "Beyond thermodynamic defect models: A kinetic simulation of arsenic activation in CdTe," *Physical Review Materials*, vol. 2, no. 10, p. 103 803, 2018.

[94] B. Dou, Q. Sun, and S.-H. Wei, “Optimization of doping CdTe with group-V elements: A first-principles study,” *Phys. Rev. Appl.*, vol. 15, no. 5, p. 054 045, 2021.

[95] J.-H. Yang, W.-J. Yin, J.-S. Park, *et al.*, “Enhanced p-type dopability of P and As in CdTe using non-equilibrium thermal processing,” *Journal of Applied Physics*, vol. 118, no. 2, 2015.

[96] T. Ablekim, S. K. Swain, W.-J. Yin, *et al.*, “Self-compensation in arsenic doping of CdTe,” *Scientific reports*, vol. 7, no. 1, p. 4563, 2017.

[97] M. A. Flores, W. Orellana, and E. Menéndez-Proupin, “Self-compensation in phosphorus-doped CdTe,” *Phys. Rev. B*, vol. 96, no. 6, p. 134 115, 2017.

[98] A. Nagaoka, K. Nishioka, K. Yoshino, *et al.*, “Comparison of Sb, As, and P doping in Cd-rich CdTe single crystals: Doping properties, persistent photoconductivity, and long-term stability,” *Applied Physics Letters*, vol. 116, no. 13, 2020.

[99] B. E. McCandless, W. A. Buchanan, C. P. Thompson, *et al.*, “Overcoming carrier concentration limits in polycrystalline CdTe thin films with in situ doping,” *Scientific Reports*, vol. 8, p. 14 519, 2018.

[100] J. Moseley, S. Grover, D. Lu, *et al.*, “Impact of dopant-induced optoelectronic tails on open-circuit voltage in arsenic-doped Cd(Se)Te solar cells,” *Journal of Applied Physics*, vol. 128, no. 10, p. 103 105, 2020.

[101] G. Kartopu, O. Oklobia, D. Turkay, *et al.*, “Study of thin film poly-crystalline CdTe solar cells presenting high acceptor concentrations achieved by in-situ arsenic doping,” *Solar Energy Materials and Solar Cells*, vol. 194, pp. 259–267, 2019.

[102] J. Park, S. Farrell, R. Kodama, *et al.*, "Incorporation and activation of arsenic dopant in single-crystal CdTe grown on Si by molecular beam epitaxy," *Journal of Electronic Materials*, vol. 43, no. 8, pp. 2998–3003, 2014.

[103] J. M. Burst, J. N. Duenow, D. S. Albin, *et al.*, "CdTe solar cells with open-circuit voltage breaking the 1 V barrier," *Nature Energy*, vol. 1, p. 16 015, 2016.

[104] A. Nagaoka, D. Kuciauskas, J. McCoy, and M. A. Scarpulla, "High p-type doping, mobility, and photocarrier lifetime in arsenic-doped CdTe single crystals," *Applied Physics Letters*, vol. 112, no. 19, p. 192 101, 2018.

[105] A. Nagaoka, D. Kuciauskas, and M. A. Scarpulla, "Doping properties of cadmium-rich arsenic-doped CdTe single crystals: Evidence of metastable AX behavior," *Applied Physics Letters*, vol. 111, no. 23, p. 232 103, 2017.

[106] D. Krasikov, D. Guo, S. Demtsu, and I. Sankin, "Comparative study of As and Cu doping stability in CdSeTe absorbers," *Solar Energy Materials and Solar Cells*, vol. 224, p. 111 012, 2021.

[107] R. Mallick, X. Li, C. Reich, *et al.*, "Arsenic-doped CdSeTe solar cells achieve world record 22.3% efficiency," *IEEE Journal of Photovoltaics*, 2023.

[108] M. Z. Alom, S. T. Elahi, V. Palekis, W. Wang, and C. Ferekides, "The effect of arsenic doping on the performance of $CdSe_xTe_{1-x}/CdTe$ solar cells," in *2021 IEEE 48th Photovoltaic Specialists Conference (PVSC)*, 2021, pp. 1460–1463.

[109] N. S. Norberg and D. R. Gamelin, "Influence of surface modification on the luminescence of colloidal ZnO nanocrystals," *The Journal of Physical Chemistry B*, vol. 109, no. 44, pp. 20 810–20 816, 2005.

[110] X. Wang, C. Zimmermann, M. Titze, *et al.*, “Properties of donor qubits in ZnO formed by indium-ion implantation,” *Phys. Rev. Appl.*, vol. 19, no. 5, p. 054 090, 2023.

[111] K. Adegoke, M. Iqbal, H. Louis, S. Jan, A. Mateen, and O. Bello, “Photocatalytic conversion of CO_2 using ZnO semiconductor by hydrothermal method,” *Pakistan Journal of Analytical & Environmental Chemistry*, vol. 19, no. 1, pp. 1–27, 2018.

[112] K. Harun, N. A. Salleh, B. Deghfel, M. K. Yaakob, and A. A. Mohamad, “DFT+U calculations for electronic, structural, and optical properties of ZnO wurtzite structure: A review,” *Results in Physics*, vol. 16, p. 102 829, 2020.

[113] W. Göpel, J. Pollmann, I. Ivanov, and B. Reihl, “Angle-resolved photoemission from polar and nonpolar zinc oxide surfaces,” *Phys. Rev. B*, vol. 26, no. 6, pp. 3144–3150, 1982.

[114] X. Ma, Y. Wu, Y. Lv, and Y. Zhu, “Correlation effects on lattice relaxation and electronic structure of ZnO within the GGA+U formalism,” *The Journal of Physical Chemistry C*, vol. 117, no. 49, pp. 26 029–26 039, 2013.

[115] F. Oba, A. Togo, I. Tanaka, J. Paier, and G. Kresse, “Defect energetics in ZnO: A hybrid Hartree-Fock density functional study,” *Phys. Rev. B*, vol. 77, no. 24, p. 245 202, 2008.

[116] H. Viet Thang, “A DFT+U study of CO and H_2 adsorption properties on Ga, Li, and Cu doped ZnO surfaces,” *ChemNanoMat*, vol. 9, no. 6, e202300024, 2023.

[117] F. Maldonado, L. Villamagua, and R. Rivera, “DFT analysis of the adsorption of phenol on the nonpolar $(10\bar{1}0)$ ZnO surface,” *The Journal of Physical Chemistry C*, vol. 123, no. 19, pp. 12 296–12 304, 2019.